A software for the reinterpretation of model independent search results and constraining theories beyond the Standard Model

Von der Fakultät für Mathematik, Informatik und Naturwissenschaften
der RWTH Aachen University zur Erlangung des akademischen Grades eines
Doktors der Naturwissenschaften genehmigte Dissertation

vorgelegt von

Master of Science
Simon Knutzen

aus
Euskirchen

Berichter: Universitätsprofessor Dr. Thomas Hebbeker
Universitätsprofessor Dr. Christopher Wiebusch

Tag der mündlichen Prüfung: 04.07.2017

Abstract

The CMS detector located at the Large Hadron Collider enables physicists to investigate a variety of models describing many different kinds of phenomena not included in the Standard Model of particle physics. Despite the huge success of the Standard Model in describing various aspects of particle physics in great accuracy, several open questions remain that can not be explain within the existing theoretical framework. In order to tackle these questions, plenty new theories are continuously developed offering potential answers which have to be tested against experimental data. The data produced by the CMS detector are sensitive to predictions of many of these new theories but the large number of existing theories renders it impossible to perform dedicated analyses for all of them.

To solve this problem and increase the exploitation of the recorded data to a larger extent, a new approach has been developed which will be presented in this thesis: Based on the approach of the analysis “Model Unspecific Search in CMS” (MUSiC), to which this work is an extension, exclusion limits are calculated depending only on the particle multiplicity and kinematic properties of various final states. These limits can later be reinterpreted in terms of different possible new theories.

This thesis describes the development of a software framework to calculate these exclusion limits and provide a tool to automatically perform the reinterpretation in terms of the theory under investigation. The framework was optimized and validated for the status of the CMS detector during the 2012 data taking period and a complete collection of model independent limits was calculated based on the full set of proton-proton collision data recorded in the year 2012 at a center of mass energy of 8 TeV.

Zusammenfassung

Der CMS Detector am Large Hadron Collider ermöglicht es Physikern eine Vielzahl von Modellen zu untersuchen, die mögliche Erklärungen für physikalische Phänomene bereitstellen welche sich nicht durch das Standardmodell der Teilchenphysik erklären lassen. Trotz der großen Erfolge, welche das Standardmodell dabei hatte, viele verschiedene Aspekte der Teilchenphysik mit großer Genauigkeit zu beschreiben, bleiben einige Fragen offen, die nicht innerhalb des Standardmodells beantwortet werden können. Es werden kontinuierlich neue Theorien mit dem Ziel entwickelt, Antworten auf diese offenen Fragen zu liefern. Der CMS Detector liefert Daten die das Potential haben, zahlreiche dieser Theorien zu überprüfen, doch erlaubt die zu große Anzahl an neuen Theorien es nicht, für jede eine dedizierte Analyse durchzuführen.

Um dieses Problem anzugehen und das Potential der aufgezeichneten Daten möglichst umfangreichend auszuschöpfen, wurde ein neuer Ansatz entwickelt, der im Rahmen dieser Dissertation präsentiert wird: Basierend auf der Herangehensweise der Analyse “Model Unspecific Search in CMS” (MUSiC), zu welcher diese Arbeit eine Erweiterung darstellt, werden Ausschlussgrenzen berechnet, die nur von der Teilchenmultiplizität und den kinematischen Eigenschaften des Endzustandes abhängen. Diese Limits können daraufhin benutzt werden um beliebige Theorien zu überprüfen.

Der thematische Schwerpunkt der vorliegenden Arbeit ist die Entwicklung eines Programmpaketes, welches die Berechnung der Ausschlussgrenzen durchführt und ein Hilfsprogramm zur Verfügung stellt, dass die Überprüfung der verschiedenen Theorien anhand dieser Ausschlussgrenzen automatisiert durchführt. Das Programmpaket wurde für den Zustand des CMS Detektors während der Datennahme im Jahr 2012 optimiert und validiert. Zusätzlich wurde ein vollständiger Satz von modellunabhängigen Ausschlussgrenzen berechnet, die auf den Proton-Proton Kollisionsdaten basieren, die im Jahr 2012 bei einer Schwerpunktsenergie von 8 TeV aufgezeichnet wurden.

Contents

1. Introduction

One of the main tasks of the CMS experiment at the Large Hadron Collider is the general search for new phenomena not described by the Standard Model, and the experimental examination of specific postulated models and theories that extend the Standard Model (called "BSM theories"). The standard approach for those tasks is the development of many different dedicated analyses, each optimized for one specific signature or model. The "Model Unspecific Search in CMS" (MUSiC) project was developed as an alternative approach to search for new phenomena: An automated scan for deviations between the measured data and the Standard Model simulation is performed without optimizing with respect to properties of the new phenomena. This approach addresses the problem of missing a potential new signature hidden in the data because it is not being looked for. This could happen since the large amount of possible extensions to the Standard Model make it impossible to perform a dedicated search for all of them. Additionally, it could be possible that a new phenomenon exists in the data for which no theory has been developed, yet.

The project described in this thesis is an extension to the MUSiC analysis. The goal is to provide information which can be used to restrain the allowed parameter space of many of the previously mentioned theories for which no dedicated analyses have been performed. For this purpose, model independent exclusion limits are calculated on the number of signal events on top of the Standard Model expectation. The limits depend on kinematic properties of the final state in many different event classes which are defined by the particle content of the final state. The event and object reconstruction as well as the Standard Model description and the event classification used for this are shared with the main MUSiC analysis [1] [2]. Once the model independent exclusion limits have been calculated, they can be reinterpreted in terms of a new theory: For this purpose, the total signal selection efficiency, depending on the same kinematic properties and event classes used to calculate the limits, has to be calculated and applied to the model independent limits in order to translate them into model specific limits.

As part of the project described in this thesis, a software framework called "MUSiC Embedded Tool for Ascertaining Limits" (METAL) was developed which can be used to calculate the model independent exclusion limits. It also provides a tool that performs the reinterpretation in a fast and easy to use manner. The limit setting procedure as well as the reinterpretation have been validated and a full set of limits has been calculated for the proton-proton collision data recorded with the CMS detector in the year 2012 at a center of mass energy of 8 TeV.

The thesis is divided into three part: In the first one, a short overview over the current state of the Standard Model and the CMS detector as well as an introduction to the statistical methods used in this analysis are given.

The second part contains a general description of the MUSiC data preparation and event classification as well as the simulation of the Standard Model expectation which is also used by the METAL project. Additional details on that can be found in [1].

The third part contains the discussion of the exclusion limit calculation and the reinterpretation method. Validation results for both aspects are given and example limits are calculated for two BSM models which are then compared to the results of dedicated analyses for the same models.

A short user's guide to the METAL reinterpretation tool and instructions on how to download it can be found in the Appendix B.

Part I.

Fundamentals

2. Theoretical Foundation

The goal of the analysis presented in this thesis is to quantify the agreement between the data measured with the CMS detector and the predictions of the Standard Model of particle physics (SM). In order to do so, a precise understanding of these predictions and in particular their signatures in the detector are needed. In the following chapter an overview of the Standard Model will be given as well as a discussion of the properties of the proton, as protons constitute the initial state of all particle interactions discussed in this thesis. A detailed discussion of the mathematical description of the Standard Model will not be given since it is not necessary for the understanding of the following analysis and would also exceed the scope of this thesis [1]. Instead of this, a phenomenological discussion of its predictions and properties will be given which should be much more beneficial for the reader in this context. All information in this chapter is taken from [4, 5] unless stated otherwise.

2.1. Basic Quantities and Units

In particle physics, a specific framework of units (called "natural units") is used which is motivated by the typical scale of the quantities it has to deal with. It is based on the definition of the unit of energy as the energy a particle with one elementary charge "e" would gain by acceleration in an electric potential of one Volt called one electron Volt (eV). Since the typical energy of objects at the LHC has increased massively compared to experiments at the time of the definition of the natural units, most energies in this thesis will be stated in Giga electron volt (GeV) to avoid numbers with large powers of ten. To simplify calculations, some natural constants are set to one: $\hbar = \mathrm{c} = \epsilon_0 = 1$. This then defines the rest of the units: Energy, mass and momentum are expressed in GeV while distance and time are expressed in 1/GeV. Velocity is expressed as a fraction of the speed of light in vacuum (c).

Interaction cross-sections (σ) of particle physics processes are expressed in the unit "femto barn" ($\mathrm{fb} = 10^{-28}\ \mathrm{m}^2$) or "pico barn" ($\mathrm{pb} = 1000\ \mathrm{fb}$) depending on the size of the cross-section. Cross-section are defined by the rate at which an interaction occurs at a specific instantaneous luminosity ($\mathcal{L}$) of the particle collider. The unit of the instantaneous luminosity is chosen to $\mathrm{fb}^{-1}\mathrm{s}^{-1}$ so that the rate can be calculated by $\mathrm{dN/ds} = \mathcal{L} \cdot \sigma$. Derived from the instantaneous luminosity is the integrated luminosity ($\mathrm{L} = \int \mathcal{L}\ \mathrm{dt}$) which describes the size of a dataset. Its unit is therefore fb^{-1}. It can be used to directly calculate the expected number of events corresponding to a specific process with a cross-section σ within this dataset: $\mathrm{N} = \mathrm{L} \cdot \sigma$.

---

[1] For information on this refer to the relevant literature (e.g. [3, 4])

2.2. The Phenomenology of the Standard Model

The Standard Model of particle physics describes the properties of the elementary particles, their behavior and their mutual interactions. It is formulated within the mathematical framework of quantum field theory which is a conjunction of quantum mechanics and special relativity. In quantum field theory, particles are described as quantized fields and the interactions between those are derived from the principle of local gauge invariance of these fields. I will start my discussion of the Standard Model with a short overview of the particles and their fundamental interaction before elaborating more on the properties of those interactions.

2.2.1. Particles and their interactions

Three fundamental interactions are included in the Standard Model: the electromagnetic[6], the weak[7, 8, 9] and the strong[10] interactions. The description of these interactions is done in the form of a unified, renormalizable quantum field theory with the gauge group $\mathrm{U}(1)_\mathrm{Y} \otimes \mathrm{SU}(2)_\mathrm{L} \otimes \mathrm{SU}(3)_\mathrm{C}$. Gravitation, which is the fourth fundamental interaction in our universe, is not included in the Standard Model. It is many orders of magnitude weaker than the other three interactions for all known particles and most of the postulated objects for a typical interaction distance considered by particle physics processes and can therefore be neglected. The three other interactions and their properties will be discussed in more detail in their dedicated sections. The electromagnetic and the weak interaction have been found to be different aspects of a common interaction called the electroweak interaction. Due to symmetry breaking they appear as separate interactions at low energies. In contrast to the electromagnetic, the weak interaction cannot be described by a stand alone quantum field theory[2]. Therefore, there will be no dedicated section on the weak interaction but a chapter on the electroweak unification instead.

The different particles of the Standard Model are defined by a dedicated set of quantum numbers and their specific masses[3].

The particles can be assigned to different categories: The most general is the separation into fermions and bosons depending on the spin of the particle with fermions having a spin of 1/2 and bosons having an integer spin (1 or 0). Bosons are the gauge particles of the fundamental interaction while fermions are associated with matter (electrons, up- and down-quark are the building blocks of atoms). The photon is the gauge boson of the electromagnetic interaction, the W and the Z boson are the gauge bosons of the weak interaction and the gluons are the gauge bosons of the strong interaction. Fermions are further divided into quarks and leptons. Their main difference is that quarks take part in the strong interaction while leptons do not. They all take part in the weak interaction while all particles with an electrical charge take part in the electromagnetic interaction.

Quarks and leptons are furthermore divided into three generations where each generation contains two quarks and two leptons. These pairs of particles are forming doublets

---

[2] A first (incomplete) description of the weak interaction without the unification with the electromagnetic one was done by Enrico Fermi in his “Theory of the weak interaction”, but will not be discussed here.

[3] e.g. A particle is an electron if it has the same mass as an electron and the exact same set of quantum numbers.

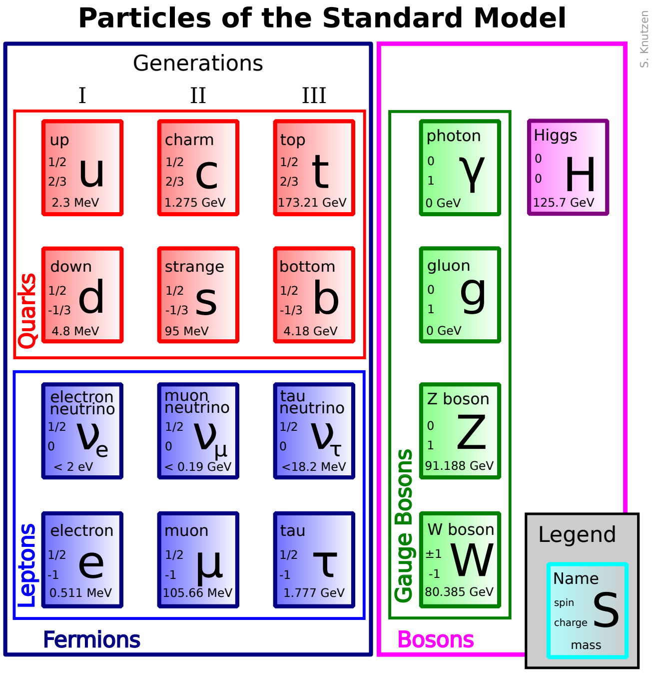

Figure 2.1.: Particles of the Standard Model and their properties[11].

of the SU(2) gauge group of the weak interaction where each particle of a pair can be identified as an up or down type orientation of a particle characteristic called weak isospin (I). This name is inspired by the normal spin characteristic of a particle since it shows the same mathematical behavior. These isospin doublets are assigned to the generations in increasing order of their mass. Each particle carries a quantum number assigning its affiliation to a specific isospin doublet. They are called “lepton/quark family-numbers”.

The up-type quarks have an electrical charge of $+2/3$ while the down-type quarks have an electrical charge of $-1/3$. The up-type leptons are called neutrinos and have an electrical charge of 0 and the down-type leptons have an electrical charge of -1.

The quarks carry an additional type of charge responsible for the coupling to the strong interaction which is called color-charge. Due to the properties of the strong interaction, there can only exist free particles which are neutral in terms of the color-charge. All configurations of quarks which lead to such color-neutral objects will always carry an integer number of electrical charge. Above all, there can be no free quarks. Leptons do not carry a color-charge and can therefore exist as free particles.

Particles will decay if there is a final state of particles which conserves all relevant quantum numbers[4] and is kinematically accessible. Due to particle decays, only the members of the lightest isospin doublets for leptons and quarks exist as stable particles in nature with the exception of the neutrinos. In the Standard Model, the masses of all neutrinos are equal to zero which means that they all exist as stable particles. In

---

[4] e.g. conserves the lepton-number, which means that a lepton will never decay into two quarks exclusively.

recent years experiments have shown that at least two neutrinos have a non-zero (but still small) mass, but this is not part of the Standard Model, yet.

To every fermion in the Standard Model exists an antiparticle with the exact same mass and with the sign of all charge-like quantum numbers inverted.

An overview of the particles of the Standard Model can be found in Figure 2.1.

2.2.2. Quantum electrodynamics

The quantum field theory "quantum electrodynamics" (QED) describes the electromagnetic interaction between charged particles and the photon field. The quantum number to which the photon field couples is the electric charge. It determines the coupling strength g which is defined as $\mathrm{g} = \frac{\mathrm{e}^2}{4\pi}$ with $\frac{\mathrm{e}^2}{4\pi} = \alpha = \frac{1}{137}$ in the limit of zero momentum transfer. The electromagnetic force has an infinite range due to the fact that the photon is massless.

Processes which are mediated by the electrodynamic interaction have to conserve all quantum numbers at all interaction vertices.

2.2.3. Electroweak unification and symmetry breaking

Weak interaction

The weak interaction couples to all fermions in the Standard Model and is the only one which can describe processes where particles are converted from one type to another. Due to this, it is the only interaction which can mediate particle decays such as the decay of the muon or the radioactive beta-decay[5]. In the Lagrangian of QED

$$\mathscr{L} = i\bar{\psi}(\gamma^\mu \partial_\mu)\psi - m\bar{\psi}\psi + g\,\bar{\psi}\gamma^\mu\psi A_\mu - \frac{1}{4}F_{\mu\nu}F^{\mu\nu} \tag{2.1}$$

it can easily be seen that conversions of particles are not possible with the electromagnetic interaction since the Lagrangian contains no terms where two different spinors are coupled in any way. The whole Lagrangian contains only one kind of spinor.

The easiest way to describe a particle conversion mathematically is to identify the two particles which should be converted into each other as two orientations of a doublet and the conversion as the rotation of the two orientations into each other.

$$\mathrm{u} = \begin{pmatrix} 1 \\ 0 \end{pmatrix} \rightarrow \begin{pmatrix} 0 & -1 \\ 1 & 0 \end{pmatrix} \cdot \begin{pmatrix} 1 \\ 0 \end{pmatrix} = \begin{pmatrix} 0 \\ 1 \end{pmatrix} = \mathrm{d}$$

The gauge group which does this is the SU(2) with the two orientations of the doublet being the base vectors of this rotation. These doublets are the quark and the lepton doublet of each generation of the Standard Model with the orientations corresponding to the up- or down-type quark and the neutrino or charged lepton, alternatively. This means that up-type quarks can be converted into down type quarks (and vice versa)

---

[5] The decay of composite objects like the π^0 meson which is mediated by the strong interaction does not contradict this statement since the decay is in fact a particle-antiparticle annihilation of its components.

and charged leptons into neutrinos (and vice versa) by the weak interaction which is described by this SU(2).

The SU(2) gauge group has three generators (W^1, W^2, W^3) and there have to be two gauge bosons with an electrical charge of ±1 mediating those particle conversions since this charge is transferred at each of those interactions. Two of the generators can be used to create those two charged bosons. They are called W-bosons which have been also found experimentally and identified as the mediators of the charged weak interaction.

Electroweak unification

Unfortunately this cannot be the full picture of the weak interaction since it cannot describe all of its properties and the last generator (W^3) cannot be identified with any real gauge boson. One property of the weak interaction is maximum parity violation for charged weak interactions. It was found in multiple experiments (Wu experiment [12], Goldhaber experiment[13]) which have shown that only left chiral fermions (and right chiral anti-fermions) take part in this interaction.

Chirality is the Lorentz invariant generalization of the helicity of a particle which describes the orientation of the spin of a particle relative to its direction of flight. Mathematically, it is the projection of the angular momentum vector onto the vector of the direction of the linear momentum. For the case of quantum mechanical spins (s) it becomes a discrete quantity and in the special case of $\mathrm{s} = \frac{1}{2}$ it has exactly two eigenvalues ($\pm\frac{1}{2}$). The one corresponding to the orientation in the direction of flight is called “right” and the opposite one is called “left”. The helicity is not Lorentz invariant since the direction of the momentum depends on the reference frame except for the case of massless particles for which it is impossible to choose a reference frame where the momentum points into the opposite direction.

To account for this behavior of the weak interaction, left and right chiral particles have to be treated differently. Since the SU(2) should not act on the right chiral fermions they do not form SU(2) doublets but only singlets. The quantum number corresponding to the doublet structure of the SU(2) is called the weak isospin which determines the coupling of the fermions to the W-bosons. It is $\frac{1}{2}$ for the left chiral doublets and 0 for the right chiral singlets. The position in the doublet defines the z-component of the Isospin (I_3) for a particle with $I_3 = \frac{1}{2}$ for the up-types and $I_3 = -\frac{1}{2}$ for the down-types.

In addition to the charged weak interaction, there is also a neutral weak interaction which is mediated by the Z-boson. Parity violation was also found for those neutral, weak processes, but it is not maximal except for processes involving neutrinos. The Z-boson couples to right chiral charged fermions though. It cannot be identified with the W^3 generator of the SU(2) since it would exhibit maximum parity violation in this case. However, it is possible to introduce a new gauge group U(1) with one generator called “B” and an additional quantum number for the coupling called “hypercharge” (Y). Mixing of this new gauge group with the known SU(2) gives rise to two new gauge bosons. When choosing the correct mixing angle and appointing the correct hypercharges to the fermions, one of these bosons has all the needed properties of the Z-boson. On top of that, the additional fourth boson has all properties of the photon which means that by this construction of the gauge groups a unified description of the weak and the electromagnetic interaction has been found. They can both be interpreted as two aspects of one single interaction which is called “electroweak”. The mixing of the four generators of the SU(2) and the U(1) into the four gauge bosons can be seen in Equation 2.2.

$$\begin{aligned} W^{+} &= (W^{1} + iW^{2})/\sqrt{2} \\ W^{-} &= (W^{1} - iW^{2})/\sqrt{2} \\ A &= \cos(\theta_W) \cdot B + \sin(\theta_W) \cdot W^{3} \\ Z &= -\sin(\theta_W) \cdot B + \cos(\theta_W) \cdot W^{3} \end{aligned} \tag{2.2}$$

The electroweak quantum numbers of all particles are shown in Table 2.1. These quantum numbers are not independent from each other and their relation is given by $\mathrm{Q} = \frac{\mathrm{Y}}{2} + \mathrm{I}_3$. The fermion generation is not specified in this table since the electroweak interaction is independent of the generation. There are no right chiral neutrinos since they interact neither weakly nor electromagneticly. The angle θ_W describes the mixing between the two gauge groups and is called “weak mixing angle”.It has been measured to $\sin^2(\theta_\mathrm{W}) \approx 0.23$. In order to obtain all needed properties of the electroweak interaction, the coupling constant g of the W-field to fermions has to be connected to the electrical charge with the relation $\mathrm{g} = \frac{\mathrm{e}}{\sin\theta_\mathrm{W}}$. The coupling constant to the W-boson and the Z-boson is of the same order of magnitude as the one for the photons and not smaller as the name “weak interaction” may imply.

	I	I_3	Y	Q
ν_L	1/2	1/2	-1	0
e_L	1/2	-1/2	-1	-1
e_R	0	0	-2	-1
u_L	1/2	1/2	1/3	2/3
d_L	1/2	-1/2	1/3	-1/3
u_R	0	0	4/3	-2/3
d_R	0	0	-2/3	-1/3

Table 2.1.: Electroweak quantum numbers of the fermions. The fermion generation is not specified since the electroweak interaction is independent of the generation.

The W-boson and the Z-boson are massive particles ($\mathrm{m_W} \approx 80.4$ GeV, $\mathrm{m_Z} \approx 91.19$ GeV)[11] which is why the weak interaction is weaker than the electromagnetic one (with the photon as a massless gauge boson) as long as the momentum transfer of a process is small to such an extent that these massive bosons are energetically suppressed. The masses of the W and Z bosons cause the electroweak symmetry to break for processes with those small momentum transfer while it is fully intact for the case that the momentum transfer is so large that the masses can be neglected.

It is not possible to simply introduce boson mass terms in the Lagrangian to account for the masses of the W and Z bosons since those terms would violate the local gauge invariance. Instead, the Higgs mechanism[14, 15, 16, 17, 18] is used to introduce these masses into the Standard Model. An additional field (the so called "Higgs field") is postulated by this theory and particles gain mass by interaction with this field.

The Higgs field gives rise to a new gauge boson, the so called Higgs boson, with a mass that cannot be predicted within the theory.

The Higgs mechanism is an elegant theory which solves not only the problem of particle masses in the Standard Model but also alters the cross-section of WW scattering which would violate the unitarity boundary otherwise. It was postulated in the year 1964 by Peter Higgs and many others but it was not possible to actually find the predicted Higgs boson until the year 2012 when analyses of the data produced by the LHC in the years 2011 and 2012 confirmed the observation of a new particle by both the CMS[19] and the ATLAS collaboration[20]. These data and later measurements have shown that this new particle is in good agreement with the properties of the Standard Model Higgs boson.

2.2.4. Strong interaction

The final interaction included in the Standard Model is the strong interaction which is described by the gauge theory called "quantum chromodynamics" (QCD). Its gauge group is the SU(3) and the corresponding quantum numbers are called color charges. There are three different types of color charges: red (r), green (g) and blue (b). In order to get an uncharged object, all three colors have to be combined. In analogy to the color picture those objects are called "white". Another way to generate a white object is by combining a color with its corresponding anti-color. Of all fermions only quarks carry a color charge and take part in the strong interaction. Every quark carries one color and the combination of three quarks with three different colors results in a white object called baryon. The combination of one quark with an anti-quark of the corresponding anti-color results in a white object called meson. The SU(3) has eight generators which give rise to eight colored gauge boson which are called gluons. They all carry a different combination of one color and one other anti-color each. This causes a gluon self interaction which leads to a potential of the strong interaction of

$$E_{pot}(r) = -\frac{c}{r} + \kappa\, r \tag{2.3}$$

with two positive constants c and κ. This means that the potential energy between two color charges increases with rising distance and an infinite amount of energy would be needed to separate those. Once the energy stored in the field between the two charges is large enough to create a new quark-antiquark pair, those will emerge with a color configuration such that the two initial color charges are shielded. The two new and the two initial quarks form two white objects and no more force acts between them. This feature is called confinement and is the reason why free quarks cannot exist. Free particles are always uncolored. The range of the strong interaction is given by this feature as the distance needed to create the quark-antiquark pair. This distance is approximately 1 fm and defines the typical size of hadrons. The strong interaction is short ranged despite the fact that the gluons have no mass. The self-interaction of the gluon field alters the effective coupling between two color charges depending on the momentum transfer of the corresponding process significantly. A larger momentum transfer which is equivalent to a smaller distance between the charges leads to a smaller coupling. This feature is called asymptotic freedom since quarks behave nearly like free particles at small distances in a nucleon. At a momentum transfer equivalent to the mass of the Z-boson the effective coupling constant is $\alpha_\mathrm{s}(\mathrm{m_Z}) \approx 0.12$ which is one order of magnitude larger than the one of QED.

2.3. The Composition of the Proton

The proton is a composite particle[21] consisting of three valence quarks, gluons and a variety of virtual quark-antiquark pairs called sea-quarks. The valence quarks determine the properties of the proton like its electrical charge or its spin. Between those valence quarks a field of gluons exists due to the strong interaction caused by the color charge of the valence quarks. These gluons give rise to the sea-quarks which are created and annihilated continuously. The components of the proton are called partons. The momentum of the proton is distributed statistically amongst these partons where the distribution per parton is described by the parton distribution function (pdf). It describes the probability that a parton carries a fraction x of the total proton momentum. Every parton type has its own pdf and the combination of all parton distribution functions for each parton is called a pdf set. Parton distribution functions are needed in order to calculate cross-sections of particle interactions during proton collisions. The calculation of these interactions are separated into two parts: The hard interaction described by quantum field theory and the processes happening inside the proton which are described by the pdf set. A factorization scale μ has to be chosen that separates these two parts. Processes happening at an energy scale above the factorization scale are assigned to the hard interaction.

It is not possible to calculate the parton distribution functions, yet, and they have to be determined from measurements. One of the most recent sets is shown in Figure 2.2 based on the work of the NNPDF collaboration [22]. There are many more collaborations which work on the determination of pdf sets. Due to different methods and extrapolation approaches they all obtain slightly different results. Since pdf sets are very important for the calculation of the cross sections of Standard Model processes, the uncertainty on the pdf sets is an important uncertainty for this analysis. There will be more information provided in Chapter 6 on which pdf set is used in this analysis and how the corresponding uncertainties are treated.

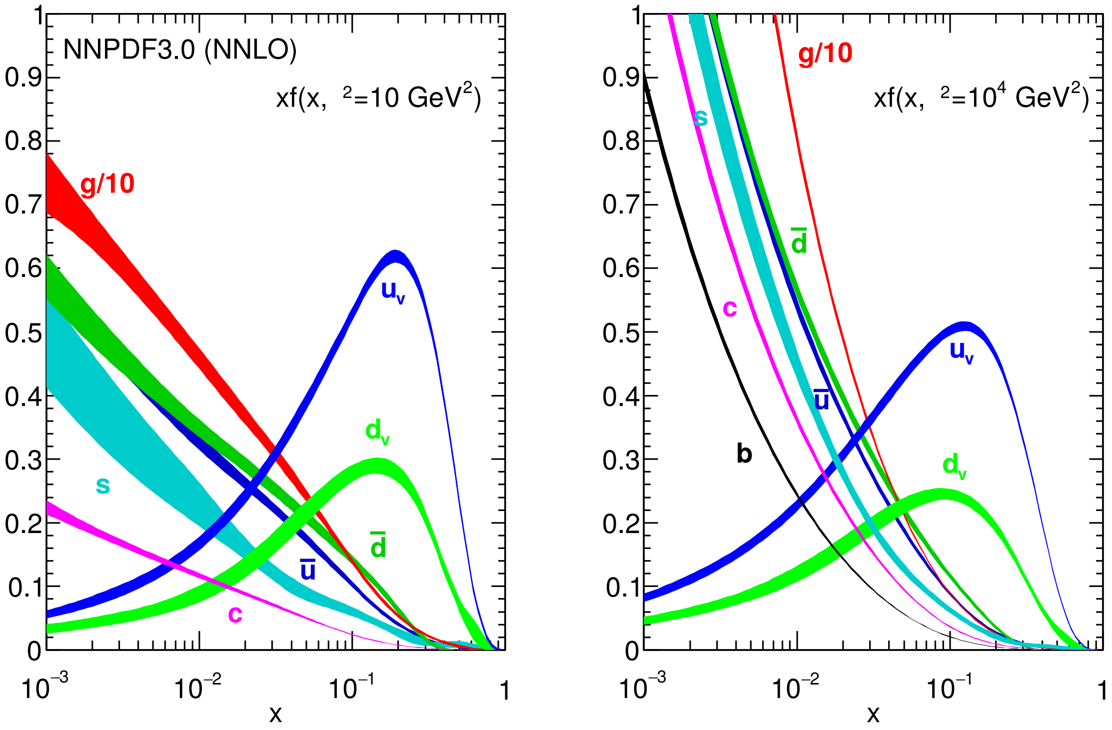

Figure 2.2.: Parton distribution function set of the proton obtained in the NNPDF3.0 global analysis.[23]. The two plots show the distributions for two different factorization scales μ ($\mu^2 = 10$ GeV^2 left, $\mu^2 = 10^4$ GeV^2 right).

3. Experimental Setup

The analysis described in this thesis uses data which was produced by the Large Hadron Collider (LHC) in the year 2012 and was measured with the Compact Muon Solenoid (CMS) detector. In the following I will review both machines as well as the computing infrastructure provided by the collaboration in outlines. The discussion of the detector will be focused on the detection performance rather than the detailed technical implementation. The status of the LHC and CMS in the year 2012 will be discussed (which does neither agree entirely with its current nor its design status).

3.1. Large Hadron Collider

The LHC [24] is a hadron accelerator ring with a perimeter of 26.7 kilometers located underground at the European Center for particle physics (CERN) close to the city of Geneva. It is the largest man made particle accelerator up to date and can be run in three different modes of operation with the first one colliding protons, the second one colliding lead ions and the last one colliding lead ions with protons. Since this analysis only deals with proton-proton collision data, only the first mode will be discussed. The proton collisions in the year 2012 took place between two proton beams with 4 TeV proton energy each resulting in a center of mass energy of 8 TeV. The protons within each beam are packed into bunches consisting of approximately 150 billion protons each. These bunches have a spacing of 50 ns between each other resulting in a bunch crossing rate of 20 MHz. The two proton beams are circulating in two separate vacuum tubes and are bent into their orbits by magnetic fields with a field strength of 8.3 Tesla created by superconducting dipole magnets. Magnets of higher multipole moments are used to focus the beams. At four interaction points the two beams are crossed causing the protons to collide. At each of these collision points particle detectors are deployed in order to measure the results of the collisions. There are two multi-purpose detectors called ATLAS[25] and CMS[26], one detector designed to measure ion collisions called ALICE[27] and one detector specialized to measure highly boosted events at small angles relative to the beam pipe which is called LHCb[28]. Additional to these four large experiments there are two smaller ones: TOTEM[29] which is located close to CMS, and LHCF[30] which is located close to ATLAS. Both use collisions occurring at the interaction point of their host experiment with final state particles whose trajectories are very close to the beampipe. TOTEM measures total interaction cross-sections while LHCF investigates particle shower properties to support cosmic ray experiments.

The LHC was designed with two key features in mind. First of all, the collisions should take place at a very high center of mass energy in order to reach energies needed to produce potential new particles with very high masses. The second important feature which had to be achieved is a high luminosity since most theories predict very small production cross sections for these new particles. One drawback of a high instantaneous luminosity is that it causes more than one collision to occur simultaneously. The measurement of one bunch crossing is called an “event” which is the smallest classification unit of the collision data and all collisions happening during one bunch crossing are pooled into one event. Since normally only one of these collisions is of interest, the other collisions cause disturbances in the detector which make it harder to reconstruct and identify the particles of interest. These unwanted additional collisions are called pileup.

The luminosity at one interaction point of a collider depends on various parameters of the machine and is given by

$$\mathcal{L} = \frac{N_b^2 \, n_b \, f_{rev} \, \gamma}{4\pi \, \epsilon_n \, \beta^*} \, F \tag{3.1}$$

where $\mathrm{N_b}$ is the number of protons in one bunch, $\mathrm{n_b}$ the number of bunches per beam, $\mathrm{f_{rev}}$ the number of revolutions per second, γ the relativistic gamma factor, ϵ_n the normalized transverse beam emittance, β^* the beta function at collision and F a geometrical factor which considers the non-zero crossing angle of the two beams. The emittance is the phase-space accessible to the protons transverse to the beam and the beta function describes the focus (squeeze) of the proton bunch.

The peak instantaneous luminosity reached in 2012 was $\mathcal{L} = 7.7 \cdot 10^{33}\ \mathrm{cm^{-2}\ s^{-1}}$ and the total luminosity delivered to CMS added up to approximately $\mathrm{L} = 23\ \mathrm{fb^{-1}}$.

The full accelerator complex with all its pre-accelerators and detectors can be seen in Figure 3.1.

3.2. Compact Muon Solenoid

The CMS detector is a multipurpose particle detector composed of different sub-detectors which are arranged symmetrically in different layers around the interaction point of the particle collision in its center. The detector was designed to identify different types of particles and measure their kinematic properties with high precision up to very high momenta. The very high collision rate present at the LHC gives rise to the demand of a very short readout time and the high particle multiplicity per collision demands a good spatial resolution and high granularity of the detector. The technical realization of these different requirements will be presented in the following section.

3.2.1. Reference frame

The reference frame of CMS is defined with the origin located at the nominal interaction point in the center of CMS, the x-axis pointing toward the center of the LHC, the y-axis pointing upwards from the LHC plane and the z-axis pointing in the counterclockwise beam direction. Cylindrical coordinates are normally used with the position of an object being expressed as the distance $\mathrm{r} = \sqrt{\mathrm{x}^2 + \mathrm{y}^2}$ from the beamline, the azimuth angle ϕ relative to the x-axis in the x-y-plane and the distance in z-direction parallel to the beamline. This x-y-plane is called transverse plane since it is transverse to the beams. The portion of a kinematic quantity restricted to the transverse plane is also denoted

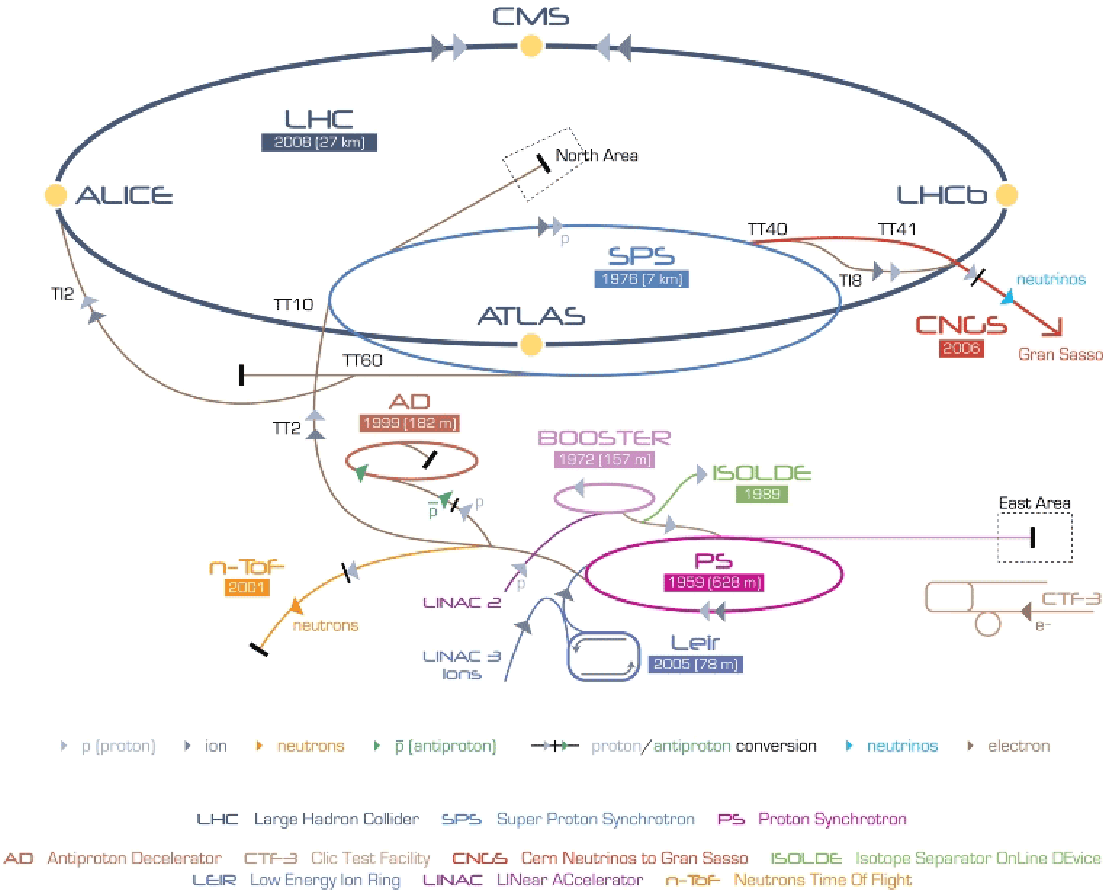

Figure 3.1.: LHC accelerator complex with pre-accelerators, main injector and experiments [31]

by the specification “transverse” (e.g. the projection of a particle’s momentum onto the transverse plane is called transverse momentum). The direction of flight of an object is often given by the azimuth angle ϕ and the pseudo-rapidity η which is a function of the polar angle θ with

$$\eta = -\ln\left(\tan\left(\frac{\theta}{2}\right)\right). \tag{3.2}$$

The advantage of the pseudo rapidity in contrast to θ is that distances in η are invariant under a Lorentz boost along the beam axis. Distances in the direction of flight of two objects are often expressed as $\Delta\mathrm{R} = \sqrt{(\Delta\phi)^2 + (\Delta\eta)^2}$.

3.2.2. General detector concepts

Every particle detector used at a collider experiment has two basic tasks: Identifying objects arising from the collision and measuring their kinematic properties. They have to be designed in a way to achieve the optimal results for a given task while dealing with the demands of the experimental setup (radiation hardness, lifespan, etc.). In order to achieve this, a compromise between different detector properties has to be found. Excellent performance in one often means some drawbacks for others. Depending on the intention of the performed experiment, different detector properties will be emphasized differently at the respective detectors with some being highly specialized while others are more general.

The basic properties of a detector are:

- geometrical acceptance (how much of the solid angle is instrumented)
- geometrical coverage (how many gaps or insensitive areas are in the detector)
- kinematic resolution (highly dependent on particle type and energy range)
- object identification potential (what kind of particles are potentially distinguishable)
- object identification purity (how large is the misidentification probability)
- dead time (how much time does it take after one detection to be ready for the next one)
- readout time (how long does it take to get the information. This is important for the trigger-system)

Various physical effects can be utilized in order to identify the type of a particle and to measure its momentum or energy with different advantages and disadvantages. The most common effects utilized to identify a particle are a) the energy loss per distance in matter, b) transition radiation, c) Cherenkov radiation and d) its ionization capability.

The most common way to measure the momentum of a particle is to measure the bending of its trajectory in a magnetic field. This devise corresponding detector is called “spectrometer”.

To measure the energy of a particle it is normally stopped in an absorber and the energy loss during the deceleration is measured. For high energetic particles, this is usually done by measuring the light which is produced within the particle shower that is induced by the initial particle in the absorber. For this case, the absorber can either be translucent or different layers of non-translucent absorber must be interwoven with light sensitive detectors. The light yield is proportional to the particle's energy as long as the particle can be stopped completely. The corresponding detector is called "calorimeter".

3.2.3. Experimental requirements and the resulting detector design of CMS

Kinematic resolution

The CMS detector was developed to measure a large number of different signatures with the energy of the objects in the final state ranging from a few GeV up to more than one TeV with high precision. The main challenge regarding the measurements of particle kinematics is given by muons at high energies since their energy cannot be measured in a calorimeter due to the fact that they are minimum ionizing particles and deposit only very little energy when traversing matter. The only way to measure their kinematics is to measure their momentum in a spectrometer, but a spectrometer's resolution gets worse for higher energies since the track bending decreases with increasing momentum. To address this challenge, CMS contains a strong solenoid coil which produces a magnetic field of 3.8 T and a precise muon tracking system.

The measurement of electrons benefits from the fact that it is possible to measure their momentum in a spectrometer as well as measuring their energy in a calorimeter. While the resolution of a spectrometer decreases for increasing momentum, the resolution of a calorimeter increases. Photons on the other hand can only be measured in a calorimeter which gives rise to the necessity of a good electromagnetic calorimeter for CMS. In order to measure the energy of hadronically interacting particles, an additional hadronic calorimeter is needed which must contain much more absorber material than the electromagnetic calorimeter since the hadronic interaction length of a material is much larger than the electromagnetic one. In order to reduce the amount of matter particles have to pass before being measured in the calorimeter the solenoid coil of CMS is placed outside of the calorimeters which makes it necessary to have a coil with a large diameter (see Fig. 3.2).

Object identification

CMS must be able to identify the types of the particles arising from the collision with high certainty in a busy hadronic environment. The particle identification capability is focused on leptons and photons while the detector does not need to be able to distinguish the type of secondary hadronic objects. Therefore, there are no dedicated identification detectors like transition radiation detectors or Cherenkov detectors deployed in CMS. The particles of interest for most of the analyses are the particles produced directly at the hard interaction. Due to the confinement of the strong interaction, quarks and gluons cannot be detected directly, but they produce a collimated bunch of secondary hadronic objects (called jets) which can be measured and used to determine the kinematics of the initial quark or gluon. For the reconstruction of jets the identification of the exact type of the contributing hadrons is not needed.

The discrimination between electrons, muons and photons against a jet is based on the total energy of all particles in a cone around the candidate which is called isolation.

The discrimination between electrons, muons and photons itself is based on the type of subdetectors they deposit a signal in. Photons do not cause a signal in the tracker[1] while neither electrons nor photons are able to reach the muon system.

In order to deal with the large particle multiplicity caused by the large cross-section of hadronic processes and the large number of pileup collisions, a precise vertex determination and track reconstruction in the inner region of the detector is needed. This is realized by a silicon based tracking detector which achieves an excellent spacial resolution while being fast enough to deal with the high bunch crossing rate. The drawback of a solid state tracking detector is the relatively large amount of matter compared with gaseous detectors which particles have to traverse before reaching the calorimeter. The excellent vertex reconstruction enables CMS to identify whether the origin of jet was a b-quark or not.

Geometrical coverage

Many signatures contain neutrinos or other postulated weakly interacting particles which are impossible to detect directly in a collider experiment. In order to gain indirect information on these objects, the detector has to be able to measure the complete vectorial sum of the transverse momenta since an undetected particle would lead to an imbalance of this sum. It is important that no detectable particle escapes the detector without being measured since it would distort the measurement. To achieve this, the geometrical coverage should be as close as possible to the full 4π solid angle and the detector needs to be hermetic with no gaps.

Final detector design

By combining all the above mentioned solutions to the various experimental requirements, the full design of CMS is obtained: It is constructed as a cylindrically shaped, symmetrical, multi-layer particle detector which is divided into a central region called “barrel” and two forward regions called “endcaps”. The innermost part of the detector is a silicon based pixel detector, followed by a silicon strip tracking detector, surrounded by a calorimeter which is divided into an electromagnetic and a hadronic one. These subdetectors are contained inside a superconducting solenoid coil. Outside of the coil are muon tracking chambers which are positioned between the different layers of an iron yoke used to contain the exterior magnetic field of the solenoid. An overview of the detector can be seen in Figure 3.2 and the different subdetectors will be discussed in more detail in the next sections.

---

[1] In fact, photons can induce pair production which give rise to an electron and a positron which can be measured in the tracker but it is not the photon itself causing the signals.

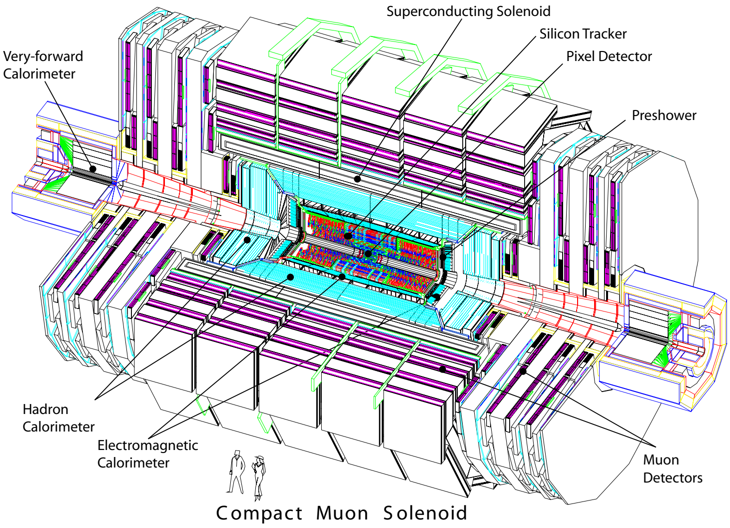

Figure 3.2.: Overview of the CMS detector and all its subdetectors[26].

3.2.4. Silicon tracking detector

The subdetector positioned closest to the beampipe in CMS is the silicon tracking detector. It is divided into three layers of pixel detectors for the innermost part and ten layers of strip detectors afterwards. Both consist of semi-conducting silicon as a active detector material in which an electrical signal is produced when a charged particle traverses it. The main task of the pixel detector is the reconstruction of the track vertices of the event and the assignment of all tracks to these vertices. The primary vertex with the largest sum of the transverse momenta of all tracks originating from this vertex is chosen as the vertex of the main interaction in this event. The other vertices are assigned to pileup interactions if they are displaced in z-direction or to secondary decay vertices if displaced in transverse direction. The correct assignment of all tracks to their vertices is crucial to suppress the influence of pileup tracks on the objects originating from the main interaction. The resolution of the measurement of the position of a vertex depends on the number of tracks associated to this vertex. A larger number of tracks increases the precision. For ten tracks the resolution in x and y direction is approximately 80 μm (95 μm for z-direction) which improves to approximately 30 μm for 50 tracks [32] equally for all directions.

The silicon strip detector which encloses the pixel detector consist of the same detector material, but is segmented into strips in contrast to pixels. It reaches up to a pseudorapidity of $\eta = 2.5$. The different layers are rotated against each other in a stereo angle in order to enable the measurement of a three dimensional position of a particle hit. This design reduces the number of readout channels significantly, but introduces the problem of hit ambiguities if one strip is hit by more than one particle. The probability for these double hits decreases with increasing distance to the beam-axis since the track density lessens due to geometrical reasons. The main purpose of the strip detector is the measurement of the track of a charged particle. The tracks are bent in direction of ϕ due to the magnetic field of the solenoid coil with the radius of the bent track being proportional to the transverse momentum of the particle. The momentum resolution worsens with increasing momentum with $\frac{\sigma_{\mathrm{p_T}}}{\mathrm{p_T}} \propto \mathrm{p_T}$ since the relative measurement of the bending becomes more inexact for smaller curvatures. For very small values of $\mathrm{p_T}$ the (relative) resolution worsens again since the negative effect of multiple scattering on the accuracy of the track measurement becomes more important than the advantage of a smaller curvature. The transverse momentum resolution of the tracker for a muon as a function of the transverse momentum can be seen in Figure 3.3 for different bins of η.

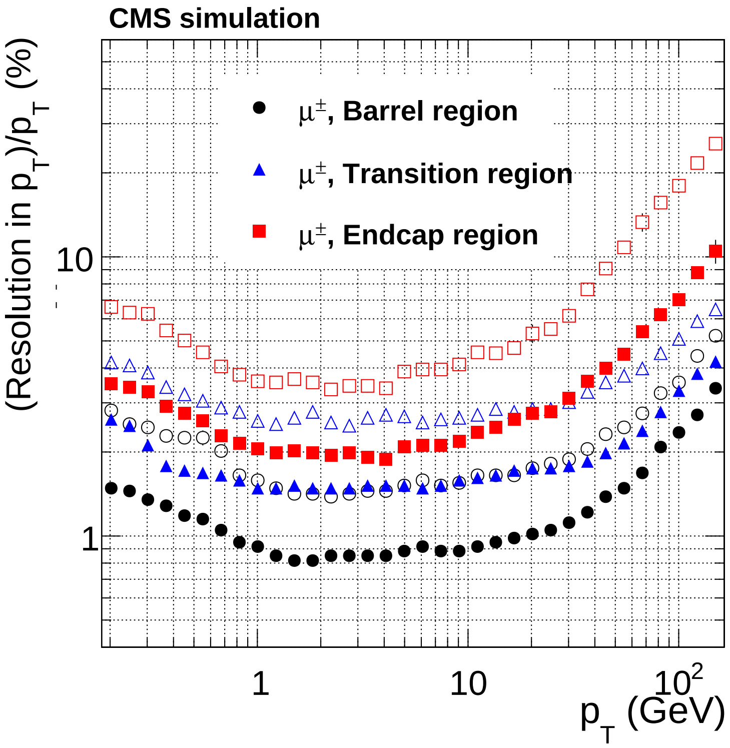

Figure 3.3.: Relative transverse momentum resolution of the CMS tracker for single, isolated muons[32]. The solid symbols represent the 68% intervals while the open symbols represent the 90% intervals. The barrel region is defined as the pseudo-rapidity range of $|\eta| < 0.9$, the transition region as $0.9 < |\eta| < 1.4$ and the endcap region as $1.4 < |\eta| < 2.5$.

3.2.5. Calorimeters

The calorimeter of the CMS detector is divided into two devices with one specialized to measure electromagnetically interacting particles and one for hadronically interacting particles.

Electromagnetic calorimeter

The electromagnetic calorimeter (ECAL) consists of lead tungstate ($PbWO_4$) crystals which are very dense ($8.28\,\mathrm{g/cm^3}$) and translucent and are therefore used as an absorber and as active detector material simultaneously. The light which is produced when a particle is stopped in the calorimeter is measured with avalanche photodiodes in the barrel and vacuum phototriodes in the endcaps. The depth of the calorimeter is approximately 26 radiation lengths for electromagnetic particles. It covers a region of pseudo-rapidity up to $\eta = 3.0$. The energy resolution of the calorimeter improves with increasing particle energies and is described by

$$\left(\frac{\sigma}{E}\right)^2 = \left(\frac{S}{\sqrt{E}}\right)^2 + \left(\frac{N}{E}\right)^2 + C^2 \tag{3.3}$$

where the three terms describe different nuisance influences. The first term describes the effect of stochastic variations in the particle shower evolution induced by the initial particle. The second one is the noise term which contains electronics, digitization and pileup noise and the constant third term describes intercalibration errors.

The resolution was determined in test measurements to be approximately[33]:

$$\left(\frac{\sigma}{E}\right)^2 = \left(\frac{2.8\,\%}{\sqrt{E\ (GeV)}}\right)^2 + \left(\frac{12\,\%}{E\ (GeV)}\right)^2 + (0.3\,\%)^2 \tag{3.4}$$

Hadronic calorimeter

The hadronic calorimeter (HCAL) is divided into three parts: The main calorimeter, the outer barrel calorimeter and the forward calorimeter. The main calorimeter is designed as a sandwich calorimeter with layers of brass as absorber and layers of plastic scintillators as active material. The energy resolution of this design is worse than the energy resolution of the electromagnetic calorimeter, but since neutral hadrons are the only particles which are measured in the hadronic calorimeter exclusively and they are not used by any analysis as stand-alone objects, this is no major drawback. Neutral hadrons are only used as input for the reconstruction of composited objects like jets. The jet energy resolution will be discussed in Chapter 7.

The depth of the hadronic calorimeter is 5.8 hadronic interaction lengths with the electromagnetic calorimeter adding additional 1.1 interaction lengths. To increase the depth, additional scintillation detectors are implemented outside of the solenoid coil which will measure remaining energy contributions of particles which could not be stopped in the calorimeter. These detectors are called the outer barrel calorimeter and the coil functions as an additional absorber for these. This increases the overall depth of the hadronic calorimeter to 11.8 hadronic interaction lengths.

The geometrical coverage of the main hadronic calorimeter reaches up to $\eta = 3.0$. In order to improve the measurement of the full transverse energy sum of an event which is needed to calculate a quantity used in many analyses called “missing transverse energy” (MET), the geometrical coverage is increased up to $\eta = 5.2$ by the forward calorimeter.

The forward calorimeter must withstand a very harsh environment since the energy flux increases with increasing values of η, which leads to strong radiation exposure. Because of that, it is built in a very robust and simple design: It consists out of a steel absorber with quartz fibers as active material.

3.2.6. Muon system

The muon system is used to measure tracks of muons outside of the magnet. This additional track measurement improves the momentum measurement for muons with high energy compared to a detector setup which only contains the inner tracking detector since the tracks of those muons are only slightly curved and measuring a longer part of this trajectory makes it easier to resolve this curvature. This improved measurement of the momentum is needed for muons with high energy since their energy cannot be measured in the calorimeters. The improvement of the momentum resolution due to the addition of the muons system can be seen in Figure 3.4.

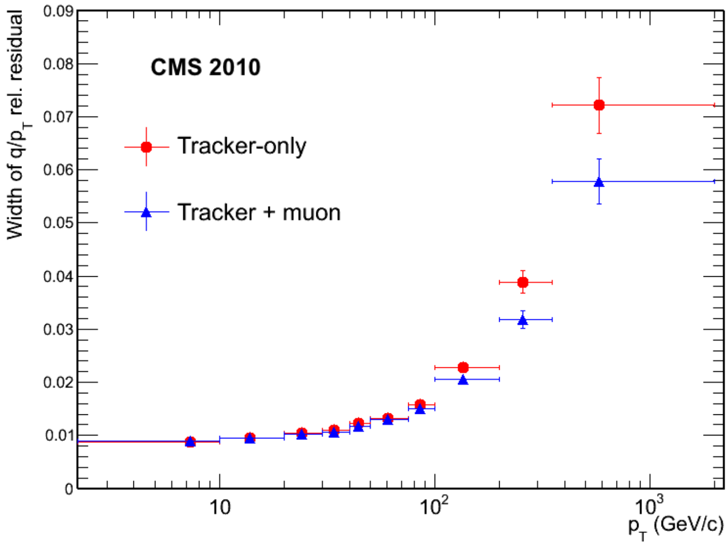

Figure 3.4.: Improvement of the muon momentum reconstruction due to the muon system in the barrel which is tested using cosmic muons traversing the detector from top to bottom: The width of the distribution of the relative differences of $\frac{1}{p_T}$ measured in the top half compared to the measurement of the same muon in the bottom half of the detector is shown. The red dots show the results obtained with only the tracker and the blue dots show the results obtained with a combination of the tracker with the muon system[34].

The muon system utilizes three different kinds of gaseous detectors: Drift tubes (DT), cathode strip chambers (CSC) and resistive plate chambers (RPC). The first two are constructed with the focus on spacial resolution and the third on time resolution. Drift tubes consist out of a single anode wire within an enclosed gas volume forming a drift cell while cathode strip chambers are multi-wire proportional chambers with a cathode segmented into strips perpendicular to the orientation of the wires. Drift tubes are used in the barrel region while cathode strip chambers are used in the endcaps since they are robust against the remnant magnetic field of the magnet in the endcap muon system and they can deal with the higher occupancies caused by the larger particle flux in the endcaps. Resistive plate chambers are used in both regions as an additional device to obtain trigger information. The muon system covers a region in pseudo-rapidity up to $\eta = 2.4$.

3.3. Trigger System

A two-level trigger system is implemented in CMS in order to perform a real time selection of collision events which are potentially valuable for further analysis since it is not possible to store and process the full amount of data of all events. In the data taking period of the year 2012, the trigger system had to reduce the event rate of 20 MHz down to around 400 Hz before data storage.

The first level (L1) of the trigger system reduces the event rate down to 100 kHz. Since this first trigger decision has to be made within 3.2 μs, the L1 trigger is implemented directly in hardware using field programmable gate arrays (FPGA) which are very fast. The L1 trigger uses only a part of the detector information for the trigger decision since it would take too long to process the whole information. Only the calorimeter and the muon system is used, but not the silicon tracker.

In a second step, the final rate reduction down to around 400 Hz is achieved by the high-level trigger (HLT) which is implemented in software and runs on a computer farm with approximately 13000 CPUs. The HLT is able to access the full detector information and can utilize event reconstruction algorithms and object identification similar to those used in the offline analyses since it can use up to 175 ms CPU time per event. This improved analysis capability compared to the L1 trigger allows for a much higher purity of the triggered events which is why a much lower event rate can be achieved without loosing much efficiency for interesting events compared to the L1 stage.

Various event topologies are considered as interesting events with each one having a specific set of requirements it has to fulfill in order to evoke a positive trigger decision. The set of all requirements for one topology is called a trigger path (or sometimes only “trigger”) and the set of all trigger paths is called a trigger menu. There are different trigger menus with slightly different requirements within the different paths which are used depending on the instantaneous luminosity of the collider. If the instantaneous luminosity of the collider improves due to machine development, the requirements of a trigger menu have to be tightened in order to keep the event rate within the bandwidth restriction. Triggered events are sorted into so called primary datasets depending on the topology of the event. For example, all events which are triggered due to the fact that they contain at least one muon (independent of the p_T threshold or isolation criterion for this muon) are sorted into the so called “single muon” datasets. Datasets are not mutual exclusive since an event can match the topology requirements of more than one dataset and can be triggered by fulfilling the requirements of more than one trigger path.

More information on the CMS trigger system and its performance during Run 1 of LHC can be found in [35].

3.4. Computing Infrastructure

In order to store and process the huge amount of data recorded with the CMS detector, a powerful computing infrastructure is needed. The record of a single event consist of approximately one MB of data which results in a data rate of a few hundred MB per second during operation of the detector. This data has to be stored as well as processed in order to be accessible for analysis. In addition, a large amount of simulated data has to be produced and stored which is needed for various tasks such as background determination, efficiency calculations, sensitivity studies and more. This adds up to an amount of data produced each year by the CMS collaboration in the order of ten peta byte.

To deal with these challenges, the worldwide LHC computing grid (WLCG) was developed. It is an association of large scale datacenters which are organized in a tier structure with three different layers. Most of the datacenters host more than one of the LHC experiments, but each one has its separate organization. In the following I will discuss the organization of the CMS computing grid within the WLCG which is illustrated in Figure 3.5.

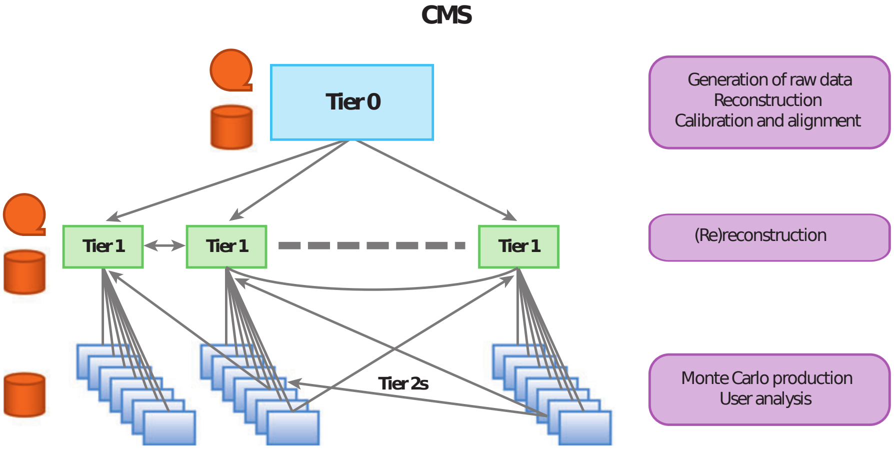

Figure 3.5.: The WLCG organization model for CMS. Adapted from [36].

The tier 0 layer consist of only one data center located at CERN. Its main task is to store and redistribute the raw data collected by the detector and perform calculations which are closely connected to the operation of the experiment like calibration. A backup copy of the data is stored on tape and a working copy is distributed amongst the tier 1 data centers.

The tier 1 data centers perform computation tasks which are of importance for the whole collaboration and are organized centrally. This includes processing of the raw data and event simulation.

Event simulation is also performed on tier 2 data centers, but their main task is to provide computing resources to the individual physicists. All tier 2 computing centers are accessible to all CMS physicists organized by a priority system. Tasks which need access to data stored on tier 2 data storage systems are distributed to the correlated tier 2 computing center. Beside of that, parts of the resources of a tier 2 center are directly accessible by the people affiliated to the organization which hosts the computing center.

The computing tasks in this analysis are mainly executed on the local recourses of the Aachen tier 2 computing center with additional usage of the distributed computing on the full tier 2 layer for the data preprocessing steps.

4. Statistical Methods

The aim of the project described in this thesis is to provide a tool which calculates restrictions on any desired model for new phenomena at the LHC by using results of the MUSiC analysis. For this purpose, exclusion limits on the number of additional events on top of the expected number of events described by the Standard Model have to be calculated. This additional event yield is called "signal" and is treated as the parameter of interest of a hypothesis test in order to calculate exclusion limits. An exclusion limit states the smallest number of expected signal events which can still be excluded given the measured data and assuming a signal plus background hypothesis. The exclusion limit is the upper boundary of the confidence interval on the signal yield which contains the true value of the signal yield with a chosen confidence level (CL). In particle physics it is common to choose a 95% CL which is also done in this thesis.

The hypothesis tests used in this analysis as well as the underlying statistical concepts are explained in the following chapter.

4.1. Frequentist statistics

All statistical methods used in this thesis are based on the frequentist's interpretation of probability. In the framework of frequentism, the probability for an event to occur is defined as the frequency of its occurrence ($\mathrm{n_x}$) normalized by the overall number of trials ($\mathrm{n_t}$) in the limits of infinite trials

$$P(x) = \lim_{n_t \to \infty} \frac{n_x}{n_t} \,. \tag{4.1}$$

For real applications, the probability for an event to occure can be estimated by observing the result of a large number of independent repetitions of a test under constant conditions. In contrast to the Bayesian interpretation of probability, the set of results from the statistical test cannot be used to deduce a probability for a theory describing this outcome of the test to be true or false given the measured data. Likewise it is not possible to assign a prior probability to a theory in order to express an a priori degree of belief in this theory. Although this seems to be a drawback of the frequentist's approach to statistics, it ensures a stringent objective definition of probability and prevents subjective assessment to have an effect on the results of statistical tests. It is important to keep these definitions in mind to avoid confusion while interpreting probabilities stated by a statistical test: A frequentist's hypothesis test performed on a dataset will only state the probability that the hypothesis that is tested will result in a dataset that deviates more from the hypothesis prediction than the observed dataset and not the probability that the hypothesis is true given the observed data.

4.2. Confidence intervals from hypothesis tests

Confidence intervals state the value range for a parameter of interest in which the true value of the parameter will be included at a certain confidence level. Confidence level has to be understood in the following way: If one would perform many independent repetitions of the experiment used to determine the confidence interval (with each repetition leading to a slightly different confidence interval), the true value for the parameter of interest would be included in the corresponding confidence intervals in a percentage of cases stated by the confidence level. This must not be confused with the probability for the true parameter to be contained in the stated confidence interval, which is not only a wrong interpretation of the result but also a probability statement about a hypothesis that is meaningless within the frequentist's interpretation of statistics. Bayesian credible intervals correspond to this probability interpretation for the true parameter. It can be in good agreement with the frequentist's confidence interval under certain circumstances, but in general it will be different.

One way to create confidence intervals with a predefined confidence level is to perform many hypothesis tests while varying the parameter of interest within the theory for each of the tests. The upper boundary of the confidence interval is then estimated by searching for the value of the parameter which results in a confidence level equal to the claimed value (95% in this thesis). This upper boundary of the interval is the exclusion limit for the parameter of interest.

The first step of performing a hypothesis test is to identify an observable of the experiment sensitive to the hypothesis. The simplest choice for a collider experiment is the number of signal candidate events which are defined by a set of requirements. Since no search can be completely free of background, it is impossible to test a pure signal hypothesis with the data. A signal plus background hypothesis has to be constructed instead. In the next step, a test statistic (Q) has to be defined which sorts all possible results of the experiment depending on how signal- or background-like they are. It is desired that the chosen test statistic provides a optimal separation between the signal plus background and the background only hypothesis. After choosing one, the probability density function for this test statistic ($\frac{\mathrm{dP_{s+b}}}{\mathrm{dQ}}$) has to be determined under the assumption of the signal plus background hypothesis in order to calculate the probability that the test statistic of an experiment originating from this hypothesis is less (or equal) signal-like than the value of the test statistic obtained from the observed data:

$$P_{s+b}(Q \leq Q_{obs}) = \int_{-\infty}^{Q_{obs}} \frac{dP_{s+b}}{dQ} dQ \tag{4.2}$$

for $\mathrm{Q} \leq \mathrm{Q_{obs}}$ being less signal-like than $\mathrm{Q_{obs}}$. This probability is the confidence level in the hypothesis ($\mathrm{CL_{s+b} = P_{s+b}(Q \leq Q_{obs})}$)(see Figure 4.1).

The test statistic used in this analysis to perform the hypothesis test is the profile likelihood ratio

$$Q = \lambda(s, b, \boldsymbol{\theta}) = \frac{L(s + b(\hat{\hat{\boldsymbol{\theta}}}), \hat{\hat{\boldsymbol{\theta}}})}{L(\hat{s} + b(\hat{\boldsymbol{\theta}}), \hat{\boldsymbol{\theta}})} \tag{4.3}$$

which is a function of the number of expected signal events s (called "signal strength"), the expected number of background b and the nuisance parameters $\boldsymbol{\theta}$. In the context of this analysis, the only nuisance parameter is the uncertainty on the expected number of background events. The nuisance parameter in the numerator is optimized to get the maximum likelihood to the measured data for each specified signal strength resulting in $\hat{\hat{\boldsymbol{\theta}}}$ as a function of the signal strength. The denominator is the unconditional maximum likelihood function with $\hat{\mathrm{s}}$ and $\hat{\boldsymbol{\theta}}$ being their maximum likelihood estimators. An additional requirement of $0 \leq \hat{\mathrm{s}} \leq \mathrm{s}$ is included to make sure that an upper limit is achieved and no two sided intervals. The inclusion of the nuisance parameters broadens the distributions which expresses the loss of information on the signal strength due to the systematic uncertainty on the background expectation.

There are various other possibilities for a valid test statistics with the number of events itself being the easiest one but according to the Neyman-Pearson lemma [37], the likelihood-ratio leads to the most powerful test. However, there is a major flaw with the classical frequentist method (called $\mathrm{CL_{s+b}}$) described above which occurs when trying to calculate exclusion intervals on parameters of a signal model with an experiment which is not sensitive to the signal. Intuitively, it should be clear that the results of an insensitive experiment should always lead to very poor exclusion limits but this is not always the case when using $\mathrm{CL_{s+b}}$ to perform the statistical test. If the number of events observed in data is lower than the number expected from background, the upper limit

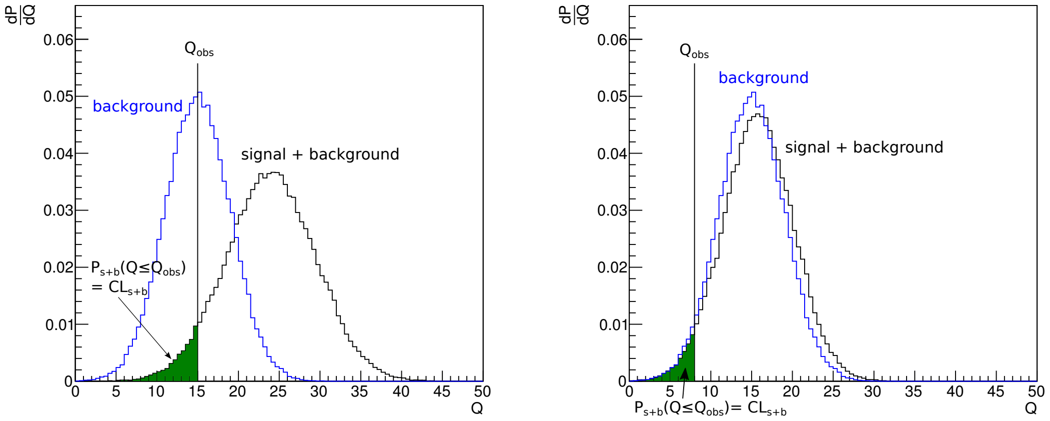

Figure 4.1.: Schematic example for the determination of the confidence level with the usage of the $\mathrm{CL_{s+b}}$ method. The two distributions in both plots show the probability density of the test statistic Q for the signal + background and background only hypothesis. In the left plot, the signal plus background and the background only hypothesis are well separated and the observed result is in good agreement with the background only hypothesis. In the right plot, the experiment is insensitive to the signal and the observation is even less signal-like than the expected background. It is an example for which the $\mathrm{CL_{s+b}}$ method fails to deliver a meaningful interpretation of the experimental results.

of the exclusion interval can become very small in the case of low sensitivity and even go down to zero (which would mean that every conceivable signal would be excluded). This conclusion from the experimental result is obviously wrong. However, this does not mean that the statistical procedure is wrong, but the interpretation of the hypothesis test becomes misleading: If the sensitivity is low, the pdf for the test statistic under the assumption of the signal plus background hypothesis becomes very similar to the pdf under the assumption of the background only hypothesis which means that a test of the signal plus background hypothesis becomes in fact a test of the background hypothesis with only slight alterations by the signal. This implies that the signal plus background hypothesis will be excluded independent of the signal for a percentage of all experimental outcomes equal to the claimed confidence level since this is by construction equal to the frequency that the background only hypothesis is falsely rejected (see Figure 4.1). It cannot be desired that a statistical test leads to a strong exclusion limit on a parameter of a signal hypothesis when it can not be separeted from an equally unlikely background only hypthesis.

4.3. The CLs technique for exclusion intervals

To elude this problem, a modified version of the classical frequentist approach is used in this analysis which is called “$\mathrm{CL_s}$ technique”[38, 39]. For this, the confidence level for signal plus background hypothesis is replaced by the ratio

$$CL_s = \frac{CL_{s+b}}{1 - CL_b} \tag{4.4}$$

with

$$CL_b = P_b(Q \geq Q_{obs}) = \int_{Q_{obs}}^{\infty} \frac{dP_b}{dQ} dQ \tag{4.5}$$

being the confidence level for the background only hypothesis. The factor (1-$\mathrm{CL_b}$) is the probability to observe a dataset more background-like than the one observed. This is used as a penalty factor in the construction of $\mathrm{CL_s}$ which reduces the confidence in the signal plus background hypothesis in cases of low sensitivity. A graphical representation of the confidence levels can be seen in Figure 4.2. If the overlap of the two probability density functions is large, the denominator of $\mathrm{CL_s}$ becomes small too and therefore the penalty is large (see left plot of Figure 4.2). This counteracts exclusion of signals in case of low sensitivity and underfluctuation of the data.

The problem that it is meaningless to state that it is very unlikely to observe a dataset more background-like given the signal plus background hypothesis if the same is true for the background only hypothesis. It is chosen by convention to reject the signal hypothesis if the hypothesis test results in $\mathrm{CL_s} = 0.05$. In analogy to the $\mathrm{CL_{s+b}}$ method it is often stated that this corresponds to an exclusion interval at 95% CL which is in fact not exactly true: The confidence interval was constructed using the confidence level in the signal plus background hypothesis but by using $\mathrm{CL_s}$ the confidence level is replaced by a ratio of confidence levels. The penalty factor will enlarge this ratio in comparison to the

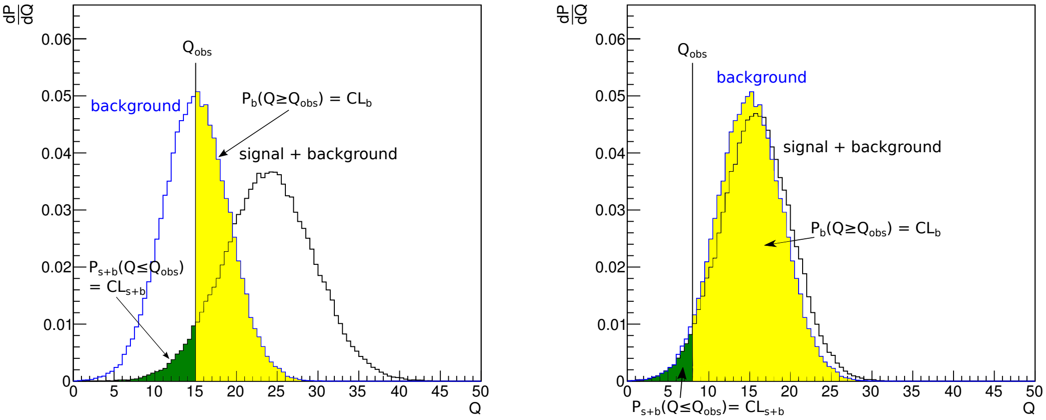

Figure 4.2.: Schematic example for the determination of the confidence level with the usage of the CL_s method. The two distributions in both plots show the probability density of the test statistic Q for the signal + background and background only hypothesis. The same two examples are shown as in Figure 4.1. The yellow area indicates the confidence level for the background only hypothesis which acts as a penalty factor to the hypothesis test. The larger the yellow area is, the larger the penalty factor. This counteracts the misleading interpretation of the example shown in the right plot and leads to a weak exclusion limit in this case.

confidence level even when the observed data is in perfect agreement with the background expectation which leads to an exclusion limit more conservative than the stated 95% CL.

The actual confidence level of the interval depends on the value of the penalty factor and can be investigated with Monte Carlo methods. By using pseudo datasets which are constructed under a fixed signal hypothesis to construct confidence intervals, the actual confidence level of an interval can be determined since it is possible in this case to count the number of datasets that result in an interval that contains the true value. The property of a hypothesis test that the constructed intervals represent the correct confidence level is called “coverage”. The case that the number of datasets resulting in an interval that contains the true value is smaller than stated by the confidence level is called “under-coverage” (more aggressive limits) while the opposite case is called over-coverage (more conservative limits).

The most challenging part of the hypothesis test is the determination of the distribution of the test statistic (the pdf of Q). There are two different approaches: Usage of Monte Carlo techniques or the description of the distributions with analytical formulas.

The first approach is performed by dicing the results of pseudo experiments under the assumption of the signal plus background hypothesis and again under the assumption of the background only hypothesis and calculating the corresponding value of the test statistic for each result. This approach is very CPU intensive since a very large amount of pseudo datasets is needed to gain a precise description of the tails of the distributions which are of main interest for the hypothesis test.

The second approach does not require any pseudo experiments which makes it much faster. Unfortunately, it is not possible to calculate the exact analytical description most of the times. In the general case it is only possible to calculate approximation formulas for the true distributions. However, it is possible to show that the formulas calculated following the recipe described in [40] approach the true distribution asymptotically depending on the expected number of background events: For this approach, the signal strength s is modeled as a nominal signal strength $\mathrm{s}_{\mathrm{nom}}$ multiplied with a signal strength modifier μ: $\mathrm{s} = \mathrm{s}_{\mathrm{nom}} \cdot \mu$. The test statistic 4.3 as a function of this modifier can then be described approximately by a normal distribution:

$$-\,2\;ln(\lambda(\mu)) \approx \frac{(\mu-\hat{\mu})^2}{\sigma^2} \tag{4.6}$$

with $\hat{\mu}$ being the signal strength modifier corresponding to the maximum likelihood of the likelihood function used in 4.3. This approximation follows from the Wald theorem [41]. The probability density function of this test statistic $\mathrm{t}_\mu = -2\ \mathrm{ln}(\lambda(\mu))$ can be described by a non central chi-square distribution for one degree of freedom:

$$f(t_\mu, \Lambda) = \frac{1}{2\sqrt{t_\mu}}\,\frac{1}{\sqrt{2\pi}}[\;exp\;(-\frac{1}{2}(\sqrt{t_\mu}+\sqrt{\Lambda})^2) + exp\;(\sqrt{t_\mu}-\sqrt{\Lambda})^2)] \tag{4.7}$$

with the noncentrality parameter Λ described by:

$$\Lambda = \frac{(\mu-\mu')}{\sigma^2} \tag{4.8}$$

where μ' is the mean value of the Gaussian distributed $\hat{\mu}$. The noncentrality parameter can be determined by using the properties of an artificial data set called “Asimov data set”. This data set is constructed in a way that it yields the true values for all parameters when it is used to evaluate their estimators. From this follows $\mu' = \hat{\mu}$ for the Asimov dataset. By using this relation, the equations 4.6 and 4.8 can be combine to:

$$\Lambda = \frac{(\mu-\hat{\mu})}{\sigma^2} = -2\;ln(\lambda_A(\mu)) \tag{4.9}$$

with λ_A being the test statistic of the Asimov dataset. This means that by exploiting the properties of the Asimov dataset, it is possible to get an estimate of the noncentrality parameter of the chi-square distribution which in turn approximates the probability density function of the test statistic for the hypothesis test.

The agreement between the description of the probability density function determined with Monte Carlo techniques and the one obtained with the approximation method increases for increasing number of expected events. Usage of the asymptotic formulas can reduce the needed computing time drastically which is why the usage of this approach is favored over the Monte Carlo techniques wherever it is valid. The determination of the validity range of the asymptotic formulas approach has been done within the framework of this thesis and can be found in Chapter 10.

Part II.

Experimental Techniques and Data Preparation

5. The MUSiC Project

The Model Unspecific Search in CMS (MUSiC) is an analysis project which dates back to the year 2008 when the first public document regarding this topic had been published [42]. However, model independent searches for new physics are around for much longer and many similar analyses have been performed at various pre-existing experiments in the past. The idea for this kind of model independent search was formulated for the first time in the L3 collaboration at the Large Electron Positron (LEP) collider[43] and was revisited at the DØ collaboration[44, 45, 46] and the CDF collaboration[47, 48] at TeVatron as well as at the H1 collaboration[49] at HERA. A model independent search is currently also performed at the ATLAS experiment[50].

Since the start of the MUSiC project at LHC, many people have worked on this topic and the analysis has been improved continuously. The basic concepts of the analysis which forms the foundation of the methods described in this chapter have been developed and implemented by my predecessors in the MUSiC working group. The main publications documenting the work of those people contain five doctoral theses [51, 52, 53, 54] and three CMS publication[55, 42, 2]. None of those analyses have seen new physics.

I have worked on the final analysis of the 8 TeV dataset in close collaboration with Deborah Duchardt whose doctoral thesis is documented in [1]. The results of this analysis are also documented in the CMS publication [2]. Both of us have developed different aspects of the analysis described in the following chapter. The final classification results which are produced with this joint analysis are used by both of us as input for each of our unique statistical interpretations.

5.1. Basic Concept of MUSiC

5.1.1. Search for deviations from Standard Model prediction

The motivation to perform a model unspecific search is to minimize the risk that signs for new phenomena in the CMS data will be missed. There are two main problems which could cause that such signs would be missed for the case that only dedicated analyses are performed. For one, there are many different theories for new phenomena and it is simply not possible to perform a dedicated search for all of them due to limited resources but the worse problem is that it is not possible to perform a dedicated search for any phenomena nobody has thought of, yet. In order to deal with these problems, MUSiC was developed as a complementary approach to dedicated analyses. A dedicated analysis aims to understand and simulate a new phenomenon as precisely as possible and then searches for its specific signature in the data. Events matching its signature are selected and compared to the expectation predicted by the Standard Model for this signature.

MUSiC in contrast aims to achieve a complete and precise description of the Standard Model expectation for the full phase space of the CMS dataset and then compares the measured data to this expectation in order to find deviations which cannot be explained by statistical effects. No data driven method is used in order to describe the Standard Model expectation since without a specific model under investigation there cannot be any signal free control region which is needed for those methods. Instead, in the MUSiC framework the description of the Standard Model is completely based on simulation. In the following the signature of a new phenomenon as well as the phenomenon itself will simply be called “signal” since the exact meaning should become clear by the context.

Due to the typically small cross section of predicted signals, it is obviously necessary to split the full data into subsets defined by some properties of the data events which have the capability to separate potential signals from the bulk of the data (without aiming at any specific signal) in order to be sensitive to it. The events caused by a signal process should be contained in only one or few of the subsets while the events caused by known Standard Model processes should be distributed over a large number of subsets. The event property used to define the subsets in MUSiC is the particle content. The particle content describes how many particles of each distinguishable type are in the final state of the collision event. This is the natural choice since the final state particles are the most common defining property of most postulated signals without being too specific to a certain kind of signals. These subsets of data defined by the particle content are called “event classes”. An example for the sorting of an event into event classes can be seen in Figure 5.2 and details on this procedure called “classification” are given in section 5.3.

To further enhance the sensitivity of the model independent search, distributions of kinematic properties of the events in each event class are produced. Instead of only comparing the total number of events in an event class expected from Standard Model simulation to the total number of real data events in that same class, the expected distributions of the kinematic properties are compared to the measured ones. Large deviations could show up in parts of a distribution while the overall number of events can be in agreement within uncertainties.

The details of the event classification as well as the kinematic distributions are described in detail later in this chapter.

Every kinematic distribution of every class has to be searched for the region of largest deviation and its statistical significance has to be calculated in order to determine if it constitutes a evidence for a new signal or if it is within the expected statistical fluctuation of the Standard Model expectation. Every possible contiguous set of bins within each distribution is considered as a search region. This search strategy which is called scanning and the results of the scans on the 2012 dataset are described in detail in [1] and will not be discussed in this thesis.

5.1.2. Upper limit on possible number of signal events

In addition to searching for significant deviations between data and Standard Model expectation, the information on the level of agreement between the two is used to calculate confidence intervals on the size of a potential additional contribution on top of the Standard Model expectation caused by any unknown signal. The size of the additional contribution is expressed in number of additional events on top of the Standard Model expectation. One sided intervals are constructed resulting in an upper limit on the number of additional events still consistent with the data at a specific level of confidence (CL). Since these limits are used to exclude theory parameters, they will be called “exclusion limits” in the following.

These exclusion limits can be used to set restrictions on parameters of any signal theory by comparing the number of additional events predicted by this theory to the upper limit on the number of additional events calculated beforehand. Since the exclusion limits can be calculated separately for every region of each kinematic distribution in every event class, the region which gains the most sensitivity can be chosen for each theory.

The task of calculating these exclusion limits as well as the development of a tool to use the limits to test new theories are the main focus of this thesis and will be discussed in detail in part III.

5.2. The MUSiC workflow

In this section an overview of the MUSiC workflow is presented (a graphical representation is shown in Figure 5.1. It can be divided into three consecutive steps: Object and event reconstruction, event classification and the statistical analysis.

The first step is dependent on the data taking period. The details of event reconstruction as well as the object reconstruction and identification change for every new dataset to react to changes in detector performance and run condition. Its purpose is to translate the raw detector information into high level physics objects (particles, jets, MET) and combine these objects into a coherent picture of the collision event. The events are checked for good reconstruction quality: Events are discarded from the analysis if problems with the detector during measurement of these event are noticed. The procedures of this step are not specific to the MUSiC analysis and established algorithms are used. This step is performed for collision data and simulated events alike. It is discussed in more detail in Chapter 7.

The second step uses the output of the first step and performs a classification depending on the particle content in the final state of the reconstructed event. Again, data and simulation are treated in the same way by the classification algorithm. The classification algorithm is completely independent of the used collision data in order to minimize the observation bias. This means for example that a pre-selection on which event classes are considered for the classification is only applied depending on the quality of the simulation[1] but not on the type of events observed in the collision data. For each event class up to three different kinematic distributions are formed: The scalar sum of all transverse momenta ($\sum p_T$), the combined mass (M_{inv}) and the missing transverse energy (MET). $\sum p_T$ is formed for every event class while the creation of the other two depends on the

---

[1] e.g. high jet multiplicities in the final state are complicated to simulate and the reliability of the predictions are questionable in this case. Therefore, event classes which require events with a large number of jets are omitted.

particle content of the specific event class. Details on those kinematic distributions as well as on the classification are given in Section 5.3.

The final step is the statistical analysis which can be divided into two independent parts: The search for deviations between the data and the Standard Model expectation and the calculation of upper limits on additional events in addition to the Standard Model expectation. Both use the kinematic distribution of the different event classes as their input. The discovery of a signal is the main goal and the initial motivation for the MUSiC analysis and would clearly be the greatest achievement we can hope for. However, the calculation of the exclusion limits provides a valuable source of information which can be used by many other physicists independent of whether we find something or not.

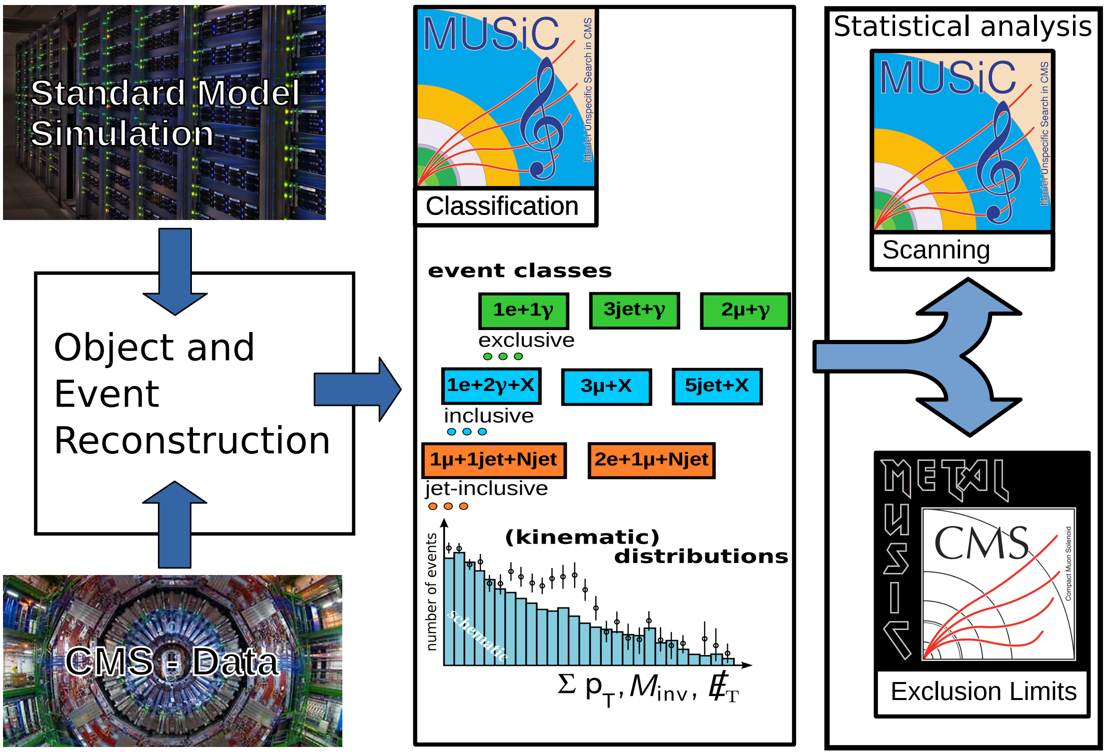

Figure 5.1.: Schematic image of the full MUSiC workflow. Standard Model simulation as well as the CMS data are reconstructed and classified in the same way. Distributions for the three kinematic variables: $\sum p_{\mathrm{T}}$, M_{inv} (M_{T}) and MET are produced for every event class. The results are then scanned for deviation between data and Standard Model expectation(discussed in [1]) and used to calculate model independent exclusion limits on the number of additional signal events (discussed in this thesis).

5.3. Classification and Kinematic Distributions

5.3.1. Classification

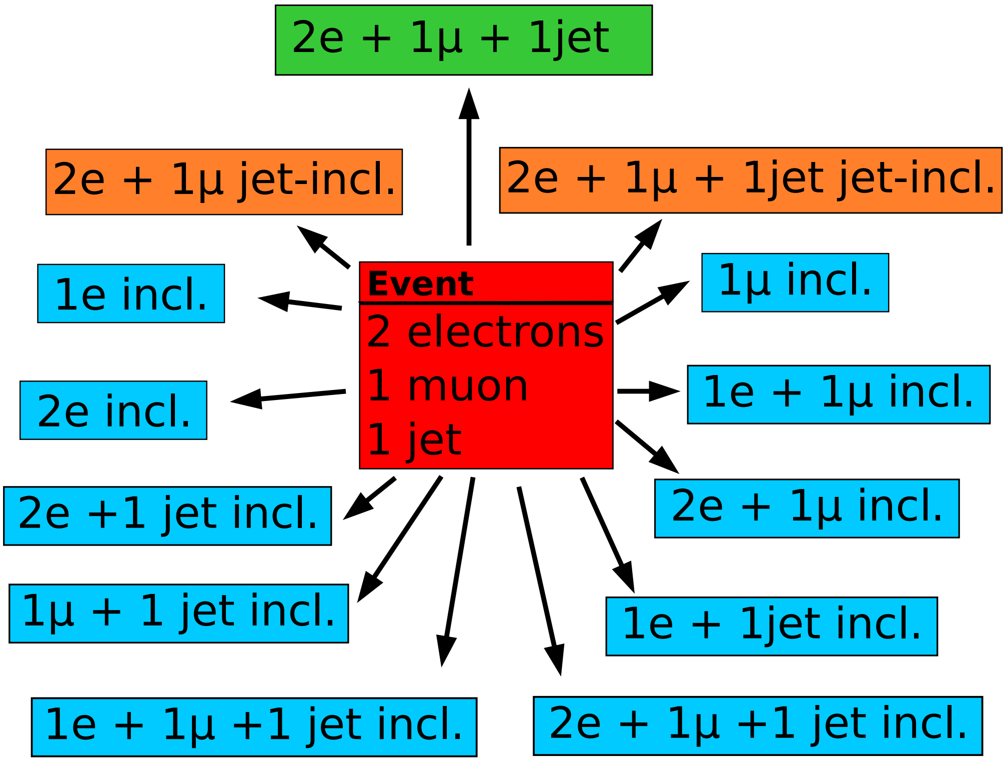

Figure 5.2.: Example of the classification for an event containing two electrons, one muon and one jet in the final state. The event will be sorted into one exclusive (green), two jet-inclusive (orange) and into 10 inclusive (blue) event classes.

The event classification used to prepare the collected data for the statistical analysis is performed using the physics object content in the final state of an event as the defining property for classification. At the moment, five different physics objects are taken into consideration by the MUSiC classification: Muons, electrons, photons, jets and MET. The number of objects of each of those five types in the final state of an event defines the event class it is assigned to. Using these 5 objects, all Standard Model particles which can emerge at a collision are covered. Every visible object which is neither a muon or a electron or a photon will be covered by a jet. Information on neutrinos are taken into account by using MET. There is the possibility to introduce further sub-categories to the jet-object by using identification algorithms which separate b-jet or hadronically decaying taus against jets produced by light quarks or gluons, but it was decided to not use these sub-categories at the moment since they would introduce further complexities into an already very complex analysis. It is possible to include those in future versions of MUSiC.

There are three different categories of event classes: Exclusive, inclusive and jet-inclusive. Every event is sorted in at least one class of each category. Exclusive event classes include all events which contain the exact number of objects stated in the event class name. Every event is sorted into exactly one exclusive class. Inclusive event classes include all events which contain at least the number of events stated in the event class name but may contain any additional number of objects. Events are typically sorted into many different inclusive classes. Jet-inclusive classes are similar to inclusive classes, but the additional objects each event may contain is restricted to jets. The lepton and photon content of an event in a jet-inclusive class is fixed.

The motivation for exclusive classes is to achieve a maximum separation of different processes. Since the criteria for an exclusive class are strictest for all event classes, the events within one class are most similar. Inclusive classes have the weakest criteria, and the events one class contains can be more diverse. This weakens the separation potential but it leads to the possibility that more events of a potential signal are concentrated in one event class since many potential signals can produce events with slightly different final states due to different decay modes. Jet-inclusive classes have been newly introduced by me to MUSiC for the analysis of the 2012 dataset. The motivation for this category of event classes is that the number of jets in the final state can vary even for identical decay modes of a new signal due to initial and final state gluon radiation. This results in a compromise between separation power and concentration of signal events.

An example of the classification for one type of event can be seen in Figure 5.2.

5.3.2. Kinematic distributions

In principle, many different kinematic quantities could be used to perform a model unspecific search since different kinds of potential signals could display clear signatures in various kinematic distributions. Due to the lack of a dedicated signal in a model unspecific search, it is necessary to select kinematic quantities which can cover a wide range of possible signatures. It is also important to restrain the number of different kinematic quantities used in the analysis to a minimum since a simultaneous usage of a large number of those would not only cause too much computational cost for the analysis, but also lead to complications in the statistical analysis caused by the so called “Look-elsewhere-effect”. This effect describes the fact that it becomes more likely to observe a significant statistical fluctuation in one search region if the overall number of considered search regions is increased. The Look-elsewhere-effect already has an substantive impact on the search for deviations in the MUSiC analysis due to the large number of considered event classes and the variety of different search regions even when considering only one kinematic distribution. The effect is treated appropriately during the statistical analysis when calculating the significance of deviations between the data and the Standard Model expectation. Details on this can be found in [1]. Despite that, only a small number of kinematic distributions should be used in the analysis to minimize the additional complications.

It was decided to create only up to three kinematic distributions for each event class depending on the final state of the event class: the **scalar sum of all transverse momenta ($\sum \mathbf{p_T}$)**, the **combined mass ($\mathbf{M_{inv}}$ or $\mathbf{M_T}$)** and the **missing transverse**

energy (MET). MET is a measure for the amount of transverse momentum that is carried by particles that have remained undetected. Details on how it is calculated are described in Chapter 7.

The scalar sum of the transverse momenta of all objects in an event

$$\sum p_T = \sum_{i}^{objects} |p_T^i| \tag{5.1}$$

is the only distribution which is created for every event class. It is the most general of the three quantities and describes the total momentum transfer at the hard interaction. It is sensitive to most possible signals since the differential cross section of most new processes should depend on this quantity.

The combined mass distribution which is the invariant mass of the combined four-vector of all objects in the final state

$$M_{inv} = \sqrt{(\sum_{i}^{objects} E_i)^2 - (\sum_{i}^{objects} \boldsymbol{p_i})^2} \tag{5.2}$$

(with $\sum_{\mathrm{i}}^{\mathrm{objects}} \boldsymbol{p_i}$ being the vector sum of the momentum vectors) is only created if the event class contains at least two objects. In this case it can be interpreted as the invariant mass of a possible mother particle which has decayed into the final state objects. In case that MET is present in the event, the transverse mass

$$M_T = \sqrt{(\sum_{i}^{objects} E_T^i)^2 - (\sum_{i}^{objects} \boldsymbol{p_T^i})^2} \tag{5.3}$$

is calculated.

The combined mass is especially sensitive to signals which contain new particles which can be produced in resonance since they lead to peaks in the combined mass distribution.

The distribution of MET is most sensitive to signals which contain new stable particles which cannot be detected directly (e.g. dark matter). These particles would cause a large momentum imbalance which results in events with a large amount of MET. Since basically every event contains at least a small amount of MET due to measurement uncertainties, it is necessary to define a minimum starting value at which MET is considered as a dedicated object in the sense of MUSiC. The MET distribution is only created if there is such a MET object in the final state of the event class.

In the case of inclusive and jet-inclusive classes not all objects in the event are used to calculate the kinematic quantities but only the ones which are stated explicitly in the event name. For example, an event which contains two electrons, one muon and one jet would be among others sorted into the `2e incl.` class. In this case, only the two electrons would be used to calculate $\sum \mathrm{p_T}$ and $\mathrm{M_{inv}}$. If there are more objects of the same type in the event than stated explicitly in the event class name, the ones with the largest transverse momentum will be used to calculate the kinematic properties. To continue the example above, the electron with the larger transverse momentum of the two would be used to calculate $\sum p_T$ which becomes p_T^e in the case of the `1e incl.` class.

The binning of the kinematic distributions is chosen to represent the resolution of the corresponding kinematic quantity which is in general a function of the quantity itself. This means that the binning cannot be constant within a distribution. More precisely, the resolution is dependent on the momenta of the different objects which yield the kinematic quantity and not the quantity itself. All kinematic quantities are obviously also dependent on the momentum of these objects but the dependence is not bijective: Different combinations of momentum values of the final state objects can lead to the same value of the kinematic quantity in MUSiC. Since they end up in the same bin of the kinematic distribution, the binning must be independent from the specific composition. In case of the combined mass it is even more complicated since it also depends on the direction of flight of each object. To achieve a generally valid binning, some simplifications are necessary: To determine the binning of the $\sum p_T$ distribution, it is assumed that the momentum is distributed equally between the different particles considered in the calculation of it and the resolutions of the separate objects are propagated on $\sum p_T$ by adding them up quadratically. For the combined mass it is additionally assumed that the pseudo-rapidity of all objects is zero and their distribution in ϕ is equidistant. In this simplified case the combined mass becomes equal to $\sum p_T$ and the same resolution can be assumed. For the MET distribution we use the fact that for sufficiently large values, the MET calculation is dominated by the $\sum p_T$ of all other objects in the event. We calculate the resolution for this $\sum p_T$ in the same way as explained above and adopt it to the MET distribution.

5.4. Analysis challenges and solutions

The concept of the MUSiC analysis is quite unique among analyses performed at particle colliders and aspects of the analysis give rise to particular challenges for which no standard procedures exist. In this section these challenges as well as the solutions developed within the MUSiC analysis group are presented.

5.4.1. Object overlap and duplicate removal

There is one important requirement the description of the final states of events has to fulfill in order for the classification algorithm to work: The unambiguous assignment of all reconstructed objects to one object type. The reconstruction of objects based on the detector information and the identification of these objects is not always clear. It is possible that a reconstructed object matches the requirements for more than one object type or that parts of the detector information are used for more than one reconstructed object (called "object overlap"). This is due to the fact that the reconstruction and identification is often developed separately for different object types by different working groups and for the most parts they are not affected by interplay. The reconstruction algorithms create object lists and it is possible that entries from different lists are originating from the same object in the detector. These additional objects are called "duplicates". For most analyses this is no problem since they are only interested in specific kinds of objects and do not care for duplicates. For example, it does not matter for an anlysis which reconstructs the resonance mass of the Z-boson if the two electrons originating from the Z-boson decay would also match the identification criteria of a photon as long as they match the criteria for electrons. However, for the MUSiC analysis this would be a problem since the additional photons would lead to a wrong final state description since there are three identified objects for only two signals in the detector. Some efforts were made within the CMS collaboration to develop a general event description without duplicates. For this purpose (among others) the "particle flow event reconstruction"[56] was developed. It is an algorithm which uses the full detector information and reconstructs the whole event in a consistent manner. If a reconstructed object could be matched to more than one object type, the most likely one is chosen. Details on the algorithm can be found in Chapter 7. Although particle flow is used in the MUSiC analysis, an additional object overlap and duplicate removal is performed in the MUSiC analysis since other more specialized object reconstruction algorithms are used in addition which spoil the unambiguity of the particle flow event description. Details on the event and object reconstruction and identification used for the analysis version described in this thesis can be found in Chapter 7.

The decision criterion used in the MUSiC object overlap and duplicate removal is the general potential to correctly identify a specific type of object. Muon is the most reliable type of object due to the fact that the CMS detector contains dedicated muon detectors which enable a clear identification of those. The second most reliable object is the electron since the tracker as well as the calorimeter can be used to reconstruct it simultaneously. Less reliable is the identification of photons which can only be detected in the calorimeter. The object with the lowest priority is the jet. Jets are built from particle flow objects that are clustered together by a clustering algorithm (details on this can be found in Section 7.5) into a single object. Since every particle flow object is regarded as a starting point for the clustering algorithm, basically every object (which fulfills a very basic set of requirements) would also pass as a jet. The only distinction against the other types of objects is done by testing if objects under investigation do not pass the identification criteria for any of the other.

The removal is performed in consecutive steps:

- In the first step, all electrons are tested against each other. If two electrons are within $\Delta R = 0.4$ and share the same track or the same supercluster seed[2], the one with the lower energy is removed.
- Next, all remaining electrons are removed which are closer than $\Delta R = 0.4$ to a muon.
- After that, photons are cleaned against each other. If two photons are closer to

---

[2] The supercluster seed is a property of the energy reconstruction algorithm using information of the electromagnetic calorimeter. It describes the starting point of the clustering algorithm which groups together the energy measurements of single calorimeter crystals to the full energy deposited by one object. Details on the energy reconstruction will be given in Chapter 7

each other than $\Delta R = 0.4$ and share the same supercluster seed, the one with the lower energy is removed.

- Remaining photons which are closer than $\Delta R = 0.4$ to either an remaining electron of muon are removed next.
- At last, all jets are removed which are closer than $\Delta R = 0.4$ to any remaining object.

After this algorithm has been performed, all duplicates or overlaps should be removed and the event is suited for the classification.

5.4.2. Limited number of simulated Standard Model events

As was mentioned before, the Standard Model expectation used in this analysis is exclusively derived from simulation. These simulations are done with well established particle physics event simulation programs which are called "event generators". In order to simulate the events predicted by the Standard Model, the simulation is divided into different processes and each is calculated separately. Different event generators exist with each being specialized for different Standard Model processes and phase space regions. The processes taken into account for this analysis as well as the generators used for each are documented in Chapter 6.

Due to the high luminosity and center of mass energy of the LHC, a large number of final states with a wide range of phase-space become accessible by the analysis. To cover all possible search regions with a sufficient amount of simulated events is not possible and it is inevitable that the description of Standard Model expectation becomes insufficient in some of those regions. Since a statistical evaluation of those regions is futile and would lead to incorrect result, they must be dealt with. In the past, methods have been tried to use the information from neighboring regions to extrapolate information into the problematic regions, but this approach has been discarded lately. Instead of this, it was decided to exclude these regions from the analysis. It is important to note that in general this does not mean that the data in this region is discarded since the region in general is part of larger regions which contains an overall sufficient Standard Model description. It is possible that the Standard Model description of the larger region is valid even if it is invalid for sub-regions since the larger region is treated as a single bin for which the contributions of the sub-regions are pooled together (see toy example elucidating this feature in Figure 5.3).

In the following section a short overview of the criteria used to determine if a region should be skipped is given. This method was developed in [1] which also contains a more detailed description. Two different features can occur which would render the Standard Model description in a region to be invalid. The first one is a very low number of simulated events in the region which implies a large statistical uncertainty on the description, and the second one is the complete absence of a dominant process. The first is easy to identify since the number of simulated events and therefore the statistical uncertainty is known: If the relative statistical uncertainty on the background prediction is larger than 60% the region is skipped. The statistical uncertainty on the background

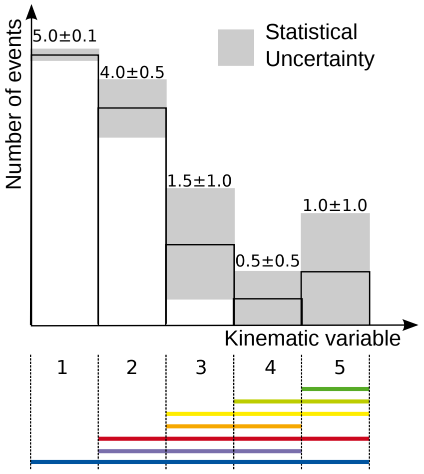

Example Regions:

Bins in Region	**N_{SM} in Region**	σ_{SM}^{stat}	$\sigma_{SM}^{stat}/N_{SM}$
5 - 5	1.0	1.00	100% ✗
4 - 5	1.5	1.12	75% ✗
3 - 5	3.0	1.50	50% ✓
3 - 4	2.0	1.12	56% ✓
2 - 5	7.0	1.58	23% ✓
2 - 4	6.0	1.22	20% ✓
1 - 5	12.0	1.87	16% ✓

...

Figure 5.3.: Combination of bins into search regions and the overall statistical uncertainty on the Standard Model description in each region [1]. The black line in the plot on the left denotes the expectation value and the dark band the statistical uncertainty. The colored lines on the bottom indicate some possible regions. In the table on the right, the expectation values of the Standard Model expectation and the statistical uncertainty on this (resulting from the combination of bins) are given for each region. A region is skipped if the relative statistical uncertainty is larger than 60%.

prediction is calculated as the square root of the quadratic sum of the event weights (ω) of all simulated events in a region:

$$\sigma_{SM}^{stat} = \sqrt{\sum_{i}^{n_{events}} \omega_i^2} \tag{5.4}$$

The event weights consist of the product of the luminosity scale factor and the scale factor of the pileup reweighting procedure. The luminosity scale factor is used to correct the number of simulated events to the expected number of events given by the cross section of the different simulated processes and the integrated luminosity of the measured data. The pileup reweighting procedure is needed to correct the simulation for differences between the generated and the actual distribution of pileup collisions. Since the number of pileup event varies between events, the event weight is also event specific. Details on the event scaling can be found in section 6.2.3.

The second one is more complicated since it is necessary to identify which missing process would be dominant in a region. To achieve this a so called neighborhood criterion is used: The contribution of each process in the four bins left and right of the region under investigation (called "neighborhood") is added up separately for each process and the leading ones which add up to at least 95% of the full contribution in the neighborhood are chosen to be the dominant backgrounds. Those have to be a non-zero contribution in the region under investigation in order to be considered valid. A visualization of the neighborhood region can be found in Figure 5.4.

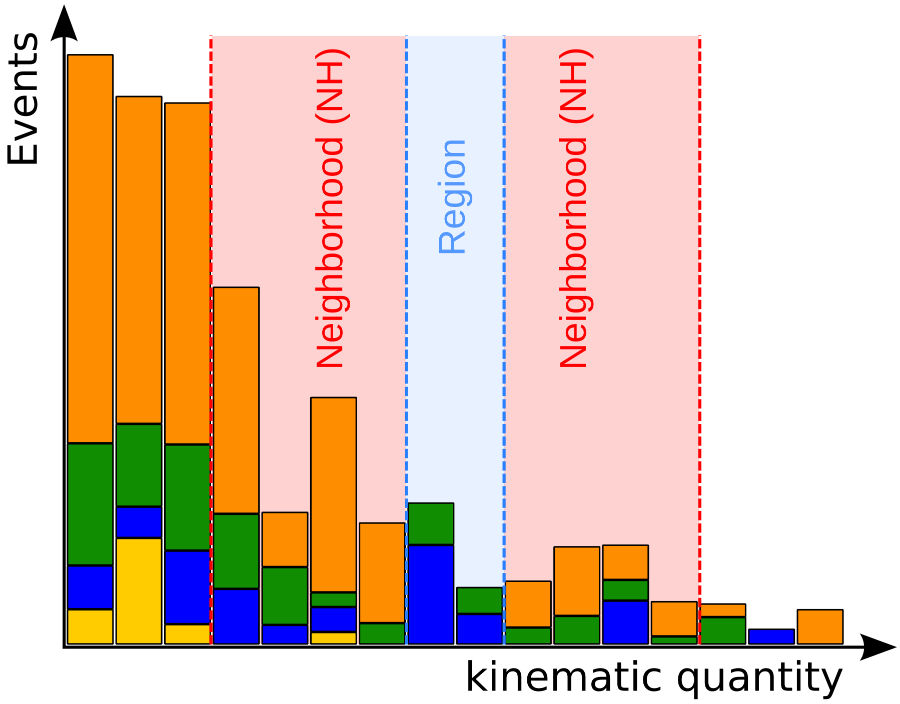

Figure 5.4.: Visualization of the neighborhood region used to determine the dominant processes in a search region (adapted from [1]).

5.4.3. Treatment of systematic uncertainties

Various systematic uncertainties on the expected number of Standard Model events have an influence on the results of the MUSiC analysis. These uncertainties can either be due to the limited precision of the cross-section calculation of the various processes, uncertainties on the collision properties (luminosity, pileup) or imperfections of the simulation of the detector and read-out electronics. The effect of each uncertainty on the number of expected background events is taken into account separately by varying the respective quantity within its uncertainty and repeat the analysis. The difference in the event yield in each bin of each of the altered distributions relative to the unaltered one gives the uncertainty on the event number caused by this specific uncertainty. Due to the change of object properties caused by the variation of energy scales, the assignment of events to event classes can change, and events from one event class can contribute to the uncertainty in another one. The alteration of an object's energy has a direct influence on the value of MET which is taken into account when treating the different energy uncertainties. Up to now, only the energy scale uncertainty of jets was considered in the MUSiC analysis. I have included the treatment of the energy scale uncertainties of all the other objects in the classification of the 8 TeV dataset which required major changes to the classification software.

Some uncertainties do not alter the shape of the distributions but only affect the global scale. For those uncertainties the analysis is not repeated but the distributions are rescaled accordingly. Examples for those kinds of uncertainties are the luminosity uncertainty and the uncertainties on the total cross sections of the different Standard Model processes.

In order to get the overall uncertainty on a search region, first the uncertainties caused by the various effects are added up separately for all bins of the search region. Correlations are taken into account for the combination of the uncertainties. For example the uncertainty on the number of events in each bin caused by the uncertainty on the cross section of a specific Standard Model process is fully correlated between all bins of a region which is why they are added up linearly. The uncertainty caused by the limited number of simulated events ($\sigma_{\mathrm{SM}}^{\mathrm{stat}}$ see equation 5.4 for definition) on the other hand are uncorrelated for all bins and are added up quadratically. After that, the uncertainties on the number of expected Standard Model events caused by the various effects are combined into a single overall systematic uncertainty by adding up all contributions quadratically since all effects are assumed to be uncorrelated. After this, every search region is characterized by three numbers: The number of observed data events, the number of expected Standard Model events and the uncertainty on this expectation.

The various systematic uncertainties will be discussed while reviewing the quantities which are connected to them (for example: The electron resolution uncertainty will be discussed in the section about electron energy reconstruction). A collection of all values can be found in Table 5.1.

5.4.4. Events with large number of jets

At a hadron collider such as the LHC, any kind of hard interaction can be accompanied by a large number of additional jets caused by initial or final state gluon radiation. The simulation of such events with a large number of jets poses a complex challenge. The matrix element calculations implemented in the different event generators do not include processes with as many additional jets as actually observed in the collision data since each additional jet introduces an additional order to the initial process and this becomes increasingly difficult to calculate. This problem is addressed by adding additional jets to the generated events based on effective models which are tuned on data and are performed using the program Pythia6 or Pythia8 [68, 69]. Since the accuracy of this prediction decreases with increasing number of jets, it was decided to introduce an upper threshold on the number of jets used to define event classes of $\mathrm{n_{jet}} = 6$. Events that contain more jets are not treated in an exclusive manner and are only included in inclusive and jet inclusive event classes with the number of jets in the explicit part of the event class equal to the threshold. For example, an event containing one electron, one muon and seven jets would be inserted into the `1e` 1μ `6jet incl.` and `1e` 1μ `6jet jet-incl.` event classes but there will be no `1e` 1μ `7jet excl.` event class. The concept of this solution was introduced to the MUSiC classification by me along with the implementation of the jet-inclusive event classes.

Type	Value	Remark and Sources
luminosity	2.6 %	pixel cluster counting [57]
number of simulated events	various	sample dependent
parton density functions	various	procedure following pdf4LHC working group [58]
object identification efficiencies		covering difference data vs MC
muon	1%	[59]
electron	2%	[60]
photon	3%	[61]
object misidentification probability		covering difference data vs MC
muon	50%	[62]
electron	100%	[62]
photon	100%	[63]
object energy scale		covering difference data vs MC
muon	5%	[64]
electron barrel	0.6%	[65]
electron endcap	1.5%	[65]
photon	0.6%	[65]
jet	various	p_T and η dependent [66]
unclustered energy	10%	[67]
cross section uncertainty		dependent on process order
samples at LO	50%	[1]
H_T-binned W+jets samples at NLO	30%	since LO → NLO k-factor strongly dependent on H_T [1]
electroweak samples NLO and approximate NNLO (NNLL)	10%	[1]
$t\bar{t}$ samples	10%	[1]
samples at NNLO	5%	[1]

Table 5.1.: Summary of all systematic uncertainties considered in this analysis.

6. Analysis Input

6.1. Collision data

In this section details are given on the collision data used for this analysis. The dataset comprises the data taken during the full proton-proton collision period in the year 2012 at a center of mass energy of $\sqrt{s} = 8$ TeV which corresponds to an integrated luminosity of $L = 19.7\ \mathrm{fb}^{-1}$. The luminosity was determined with a method called "pixel cluster counting". In this method the number of clusters in the pixel detector is used to calculate the instantaneous luminosity per bunch-crossing depending on the total visible cross section of the proton-proton collision. This visible cross section is calibrated by using Van der Meer scans. Details on the luminosity determination method can be found in [57]. The uncertainty on the luminosity value is evaluated to 2.6 % which is a combination of the statistical and systematical uncertainty stated in [57].

The analysis is restricted to data preselected by at least one of the four types of lepton based triggers listed in Table 6.1.

Type	Name	Description
single muon	HLT_IsoMu24_eta2p1_v*	single isolated muon with $p_T^{\mu} > 24$ GeV
single electron	HLT_Ele80_CaloIdVT_TrkIdT_v* **or** HLT_Ele80_CaloIdVT_GsfTrkIdT_v*	single electron with $p_T^{e} > 80$ GeV and loose calorimeter and track quality requirements
double muon	HLT_Mu17_Mu8_v*	Two muons with $p_T^{\mu 1} > 17$ GeV and $p_T^{\mu 2} > 8$ GeV
double electron	HLT_Ele17_CaloIdT_CaloIsoVL_TrkIdVL_TrkIsoVL_v* **or** HLT_Ele8_CaloIdT_CaloIsoVL_TrkIdVL_TrkIsoVL_v*	Two electrons with $p_T^{e} > 17$ GeV for both **or** $p_T^{e} > 8$ GeV for both and loose calorimeter and track quality requirements

Table 6.1.: List of triggers used by this analysis. Different versions of the triggers have been used (indicated with "v*" in the name) and in the case of the single and double electron triggers, one larger change had been made at one point during the data taking period, resulting in a new trigger name for each.

There have been various versions of the different triggers differing in small details of their precise implementation (indicated with "v*" in the name). They have been developed over the course of the data taking to adapt the selection to changes in the run conditions. For both the single and double electron trigger, one larger change to the trigger requirements have been made during the data taking period and both changed triggers have received a new name. For the single electron trigger the track reconstruction algorithm was changed and for the double electron trigger the momentum threshold for the electrons was adapted. Details on the object and event selection performed by the CMS trigger system and the trigger efficiencies can be found in [35].

Those triggers have been chosen for this analysis since they impose a very loose set of requirements which is important for a model unspecific search in order to not exclude potentially interesting events from the analysis. Of course the requirement of at least one lepton represents a noticeable restriction of the analysis but including further triggers would increase the amount of work needed for this analysis drastically and is not done here. There has been a dedicated analysis which performed a MUSiC analysis on events triggered by high energetic hadronic jets [70].

In addition to the requirement of a positive trigger decision, all events have to be certified by CMS detector experts who verify that all detector components have worked correctly. The analysis documented in this thesis uses the official CMS certification file called *Cert_190456-208686_8TeV_22Jan2013ReReco_Collisions12_JSON.txt* to identify the validated events.

6.2. Standard Model prediction

In order to search for new phenomena in the collected data, it is necessary to gain a precise knowledge what data is predicted by the Standard Model. As was said before, we do not deduce any information on the Standard Model prediction from the collected data (as is often done by dedicated analyses) since signal free control regions are needed for this approach. As no assumptions are made on the properties of possible signals within the MUSiC analysis, it is not possible to define those regions. Instead, the prediction is completely deduced from theoretical calculations and simulation.

6.2.1. Calculation of Standard Model processes

The simulation of the Standard Model expectation is done by programs called "event generators" which are widely used in particle physics. The description of the full Standard Model is divided into various processes and different event generators are used to provide the best description since each of them is specialized on different aspects of the simulation. The precision to which different processes can be calculated differs depending on the underlying theory which results in different uncertainties for different contributions to the full Standard Model description. Processes mediated by electroweak processes are often known at next-to-next-to-leading-order (NNLO) precision of QCD corrections while QCD processes are in many cases only simulated at leading order precision[1]. The event generators use random number generators to produce samples of pseudo-events with properties following the differential distributions of the different processes and therefore they are often referred to as “Monte Carlo event generators” (and subsequently, the pseudo-events samples are sometimes called “Monte Carlo samples”). Additionally to the calculation of the hard interaction of the main process, parton showering and hadronization has to be simulated in order to describe the final state of the event correctly. Parton showering describes the initial and final state radiation consisting of color charged particles and hadronization describes the formation of color-neutral hadrons out of quarks or gluons. It is performed with the programs Pythia6(8) [68, 69] which use effective models for this task since a full QCD calculation is not possible since the processes in the parton shower happen at a small momentum scale where pertubative QCD calculations are impossible.

6.2.2. Detector simulation

After the events of a process have been generated, a full simulation of the response of the CMS detector and the read-out electronics is performed. The results of this detector simulation are then treated in the same way as the recorded data and the full event and object reconstruction is performed for it. After this step, the data and the Standard Model simulation should be in the same condition and they can be compared directly since they are stored in the same data format. The object information before the detector simulation is called “generator level” information and after the full detector simulation and the object reconstruction “reconstruction level” information. The simulation of the CMS detector was done within the GEANT4 software framework [71] which predicts the response of the detector from basic principles describing particle interaction with matter and fields and known material properties. Since this simulation can only approximate the true detector response, some corrections have to be applied to the simulation which are calculated by several groups within the CMS collaboration. Some of these corrections are determined from datasets which are also used in the MUSiC search (e.g. correction factors for lepton identification efficiencies) which is why they are not applied in this analysis to minimize the biasing of the search but are considered as systematic uncertainties. Those corrections and the corresponding systematic uncertainties are documented in Chapter 7.

6.2.3. Event scaling

Since all produced samples contain a number of events ($\mathrm{N_{MC}}$) independent of the recorded dataset, they have to be scaled to the correct number of expected events depending on the inclusive cross section of the process under consideration (σ) and the integrated luminosity of the collision data (L). For this purpose, a weight factor

$$w = \frac{\sigma \cdot L}{N_{MC}} \tag{6.1}$$

---

[1] The calculation of cross sections done in the context of quantum field theory is performed by using an expansion of the process in terms of the number of interaction vertices contributing to the process. Leading order denotes the subprocess with the minimum number of vertices needed.

is assigned to each generated event.

A second type of event weight is used to account for differences between the pileup conditions during data taking and the conditions assumed during sample production. Pileup is strongly dependent on the instantaneous luminosity of the collider. Since the production is done beforehand, a subsequent correction is needed. The pileup simulation is done in the way that a specific number of simulated minimum bias interactions[2] is added to each event following a predefined distribution. The correction is then done by comparing the distribution of the expected pileup interactions in the recorded data with the distribution used during the sample production and calculating the deviation factor between data and simulation for each number of pileup interactions. The factor corresponding to the number of pileup events in a simulated event is then assigned as an additional weight to each event. This procedure is called “pileup reweighting”.

The challenge of this approach is to determine the number of pileup interactions in a recorded data event. For the 2012 data taking period it was decided to calculate this number by using the total inclusive proton-proton collision cross section and the instantaneous luminosity for each bunch crossing. This total inclusive cross section can be determined by using a measurement performed on the 2011 dataset at a center of mass energy of $\sqrt{s} = 7$ TeV and extrapolating the results to $\sqrt{s} = 8$ TeV or by direct measurement in the 2012 dataset. The result of the former approach is used to calculate the correction weights while the latter one is used to calculate a second set of weights which are used to estimate the systematic uncertainty caused by the pileup reweighting.

6.2.4. Sample production

The production of Standard Model samples is performed centrally by the CMS collaboration. Those samples consist of a set of events of a specific particle physics process within some kinematic boundary conditions (a minimum momentum transfer threshold of the hard interaction is set for many samples while most of the times no explicit upper threshold exist other than given by the maximum possible amount of momentum carried by the initial state partons). Large numbers of generated events are needed for the different processes in order to achieve a description with sufficient statistical precision over the interesting phase-space[3] within those boundaries. Processes with larger cross section apparently need samples with a larger number of events to achieve the same precision as samples with smaller cross sections but due to limitations in computing capacity, losses in precision have to be accepted for samples with very large cross section (like W-boson production or QCD induced multi-jet production). To soften the effect of limited statistical precision, those samples are further divided into separate samples for

---

[2] Minimum bias means in this context that a very loose pre-selection of the process type was done for this interaction. It can be any type of process described by the Standard Model that causes a signal in the detector strong enough to distinguish it from electronic noise. However, since the probability of one process type to occur depends on the cross section of the process, basically all events will be QCD induced jet production with low momentum transfer.

[3] The statistical precision will of course decrease with decreasing differential cross section and at some point it will be insufficient for a valid description of the Standard Model expectation. The goal is to provide enough events that this will not happen in regions of the phase-space where data events are expected.

different phase-space regions. By doing this, the number of events in rare phase-space regions can be enhanced without increasing the overall number of events too much. Due to the independent production of most of the samples, some overlap between different samples is quite common and has to be removed. This is done by rejecting all events from the more general sample which are located in the phase-space region of a more specific sample. A careful composition of the set of used Standard Model samples is needed to gain the best possible and complete description of the Standard Model expectation for the MUSiC analysis. This was done by [1] and an overview of the composition can be found in Appendix A.

6.2.5. Parton distribution functions

One important part of the event generation is the correct description of the parton distribution functions (pdfs) for the purpose of cross section calculation. The initial state particles of the processes calculated by the event generators are not the protons but the partons within the protons. The center of mass energy of this system ($\sqrt{\hat{\mathrm{s}}}$) is not the same as the center of mass energy of the proton system since the partons only carrying a fraction of the full momentum (x_1 and x_2) which results in $\sqrt{\hat{\mathrm{s}}} = \sqrt{\mathrm{x}_1 \cdot \mathrm{x}_2} \cdot \sqrt{\mathrm{s}} = \sqrt{\mathrm{x}_1 \cdot \mathrm{x}_2} \cdot 8$ TeV. Parton distribution functions describe the probability density for a parton to carry a specific momentum fraction (see also Section 2.3). This information is needed to calculate the full production cross section of a process by integrating the differential production cross section at parton level ($\hat{\sigma}_{\mathrm{i,j}}(\mathrm{x}_1, \mathrm{x}_2, \hat{\mathrm{s}}, \mu^2)$) over the full phase space weighted by the pdfs ($\mathrm{f}(\mathrm{x}_1, \mu^2)$, $\mathrm{f}(\mathrm{x}_2, \mu^2)$) and summed over all partons (i,j):

$$\sigma = \sum_{i,j} \int_0^1 \int_0^1 dx_1 dx_2 f_i(x_1, \mu^2) f_j(x_2, \mu^2) \hat{\sigma}_{i,j}(x_1, x_2, \hat{s}, \mu^2) \tag{6.2}$$

where μ^2 is the factorization scale used to separate the hard interaction from the processes described by the pdf (see Section 2.3).

There are many different groups who calculate pdf sets using different selections of input data and calculation methods. For each generated sample one specific pdf set is used. The uncertainty on these pdf sets is an important uncertainty for this analysis since it directly influences the Standard Model expectation and its influence on the final results has to be taken into account. Since the different pdf sets calculated by the various working groups do not match each other perfectly, the difference between the various sets has to be taken into account as well. This is done by following the recommendation of the pdf4LHC working group[58]. It instructs to take into account three independent pdf set groups and their uncertainties and propagate the effect of the variation of the differential production cross section onto the final distributions. Simultaneously, also α_{s} is varied within its uncertainty since it has a large impact on the pdf. The envelope of the predictions of all variations is then used as the final uncertainty. The straight approach to do this would be to generate each Standard Model sample many times with the varied pdf sets which is not feasible since it would create too much workload for the available computing resources. Instead, a set of weights is produced for each varied pdf set and these events are used to reweight the initial sample.

The pdf sets used in this analysis to calculate the uncertainties are: `CT10`[72], `MSTW2008`[73] and `NNpdf2.3`[74].

7. Object and Event Reconstruction

In order to perform the MUSiC classification it is necessary to reconstruct and identify the different physics objects within each event and to reject events which feature some sort of experimental flaws. These flaws can be unusually high noise in some of the detector parts, contamination by beam halo particles or similar effects. Standard algorithms specifically designed for the experimental conditions during the 2012 measurement period are used to reconstruct and identify the different objects and determine the quality of the events. These algorithms have not been developed by experts of the CMS collaborations and are used in this analysis according to general recommendation. In the following chapter, a short overview of these algorithms will be presented as well as the reconstruction qualities achieved by those. An overview of the p_T and η acceptance for all physics objects can be found in Table 7.1.

Object	kinematic acceptance	geometric acceptance
Muon	$p_T > 25$ GeV	$\lvert\eta\rvert < 2.1$
Electron	$p_T > 25$ GeV	$\lvert\eta\rvert < 2.5$ with $1.442 < \lvert\eta\rvert < 1.56$ excluded
Photon	$p_T > 25$ GeV	$\lvert\eta\rvert < 1.442$
Jet	$p_T > 50$ GeV	$\lvert\eta\rvert < 2.4$
MET	MET > 50 GeV	

Table 7.1.: Acceptance in p_T and η for all physics objects used by the MUSiC analysis. These are the minimum requirements for any object to be considered in the analysis. In addition, stronger thresholds are required for the leading electron or muon in events triggered by the single electron or single muon trigger in order to account for the higher p_T thresholds demanded by the trigger selection (see Table 7.2).

7.1. Particle Flow

The particle flow (PF) algorithm [56] is the main algorithm to reconstruct and identify event and object properties within the CMS collaboration for the 2012 dataset. Instead of reconstructing different objects independently from each other, as it was done by previous algorithms, the PF algorithm takes into account the whole detector information simultaneously in order to create a complete and unambiguous set of particles for each event. Beside the obvious advantage of the algorithm that double assignment of objects and detector information is avoided, it also improves the reconstruction quality of derived physics objects like jets and missing transverse energy. In the past (and at previous experiments), both objects where mainly reconstructed by only using information from the calorimeters: Jets were reconstructed by clustering together energy deposits in calorimeter cells and MET was determined by adding up all transverse energy components measured by the calorimeter. Instead of this, the PF algorithm uses individual particles in order to reconstruct the jets and determine the MET. This improves the energy resolution of those objects since information from different subdetectors are used in order to reconstruct the constituent particles and not just the calorimeter information.

A short overview of the algorithm will be provided in this section. More detailed information can be found in [56]. The algorithm starts with the independent reconstruction of energy clusters in the calorimeters as well as tracks in the silicon tracker and the muon system. After that, these subdetector objects are linked together into units than can be associated to different particle hypotheses (called "blocks"). For example, a muon would be associated to a block consisting of a track in the muon system that is linked to a track in the silicon tracker but won't contain any calorimeter energy cluster. The linking is not unambiguous and all possible hypotheses are tried in order to find the one which is most likely. The quality of the links is quantified by the $\frac{\chi^2}{\mathrm{N_{dof}}}$ of the combined fit of tracks in the muon system and the silicon tracker and the distance of the center of the energy clusters to tracks extrapolated into the calorimeter. After that, the algorithm assigns each block to a specific particle type. This assignment is done iteratively starting with the particle which is easiest to identify (the muon) and then proceeds to the more challenging objects (electrons, charged hadrons, photons, neutral hadrons). Particle types are assigned to the blocks based on how compatible the observed properties are with the expected properties of the different types.

Due to the fact that the algorithm has to be very generic, special algorithms and extensions have been developed for some physics objects to take care of special requirement like high purity or momentum reconstruction at high energies. These special algorithms are explained in more detail in the following sections.

7.2. Muon

7.2.1. Reconstruction

The key feature of the muon reconstruction is the reconstruction of its track since the muon energy cannot be measured in the calorimeter. It is important to determine the bending of the muon track in the magnetic field with high precision up to high momenta. This can be achieved by combining the track information from the silicon tracker with the measurements in the muon chambers. However, it is not always the best choice to use the full information from the muon system since the measurement in the outer chambers can be flawed due to multiple scattering or high energy loss by bremsstrahlung in the iron return yoke of the magnet. The latter is especially important for muons with very high momentum since the radiation loss of energy becomes stronger with rising momentum. This energy loss can alter the bending of the trajectory in the outer chambers and there can be additional hits due to secondary particles caused by the radiation emitted by the muon. Several different track reconstruction algorithms have been developed to account for this and an additional algorithm (called "cocktail" algorithm) decides for each muon which of the algorithms yields the best track reconstruction quality. The transverse momentum resolution achieved by this algorithm can be seen in Figure 3.4 in Chapter 3. This approach is recommended by the CMS muon experts and is also used in the high energy muon benchmark analysis [59]. The initial algorithms have been introduced in [75]. An uncertainty of 5%[1] is assumed on the description of the energy scale in the simulation [64]. Detailed information on the updated version developed specifically for the 2012 data which is also used in the analysis described in this thesis can be found in [76]. The track reconstruction algorithms to choose from are:

- **Tracker Muon:** The momentum of the muon is determined exclusively from the track reconstructed in the silicon tracker. The track has to be tagged to a valid segment in the muon system to be considered as a muon candidate. This algorithm performs best for muons with low or medium momentum ($p_T < 200$ GeV). For these muons, the curvature of the track is still large enough that the lower precision in the muon system due to multiple scattering in the iron would surpass the gain of observing a longer part of the track.

- **Global Muon:** The global muon uses a combined fit to all hits in the tracker and the muon system assigned to one track to reconstruct the momentum of the muon. This can be a good choice once the multiple scattering (which decreases with momentum) is small enough and the disturbance caused by radiative energy loss (which increases with momentum) is not yet too high.

- **Tracker plus first muon station (TPFMS) Muon:** For muons with very high energy it is often the best choice to combine the information from the tracker only with the information from the first muon station since it is located in front of the first layer of the iron yoke. The muon chambers after that are influenced by possible particle showers caused by the energy loss of muons in this layer of iron and therefore the quality of their measurement is worse.

- **Picky Muon:** This algorithm is an extension of the TPFMS algorithm. Not all muon chambers after the first one are dismissed by default but instead for each one it is tested if a particle shower has aggravated the measurement and only those are dismissed. This test is based on the number of hits in the muon station which will be unusually high if a shower has occurred.

7.2.2. Identification

The muon identification is based on sets of requirements an object has to fulfill in order to be denoted as a muon. The set used in this analysis is called "Tight Muon ID". The main two features used to identify muons are the reconstruction quality of the

---

[1] This relatively large uncertainty is caused by the fact that it must provide a valid description of the momentum uncertainty at large momenta where the reconstruction becomes challenging due to a small curvature of the muon track.

track and the isolation of the object. The former one is slightly modified for muons with $p_T > 200$ GeV which is then called “High p_T Muon ID”. Additionally, the muon candidate must fulfill $p_T > 25$ GeV since the identification selection was only validated for those and $\eta < 2.1$ to be consistent with the single muon trigger. A short discussion of the different requirements is given in the following list:

Track quality

- **Global track fit quality:** $\frac{\chi^2}{N_{dof}} < 10$ for global track fit, at least one muon chamber hit is included in the global fit and muon segments[2] are reconstructed in at least two muon stations. This selection suppresses misidentification due to signals in the muon system not related to a muon. This can happen due to remnants of hadronic showers reaching the muon system (called “punch-through”).
- **Global muon:** The muon has to be reconstructible as a global muon (even when the cocktail algorithm chooses another p_T reconstruction algorithm).
- **Particle flow muon:** The muon is identified by the particle flow algorithm.
- **Impact parameter of tracker track:** The impact parameter is a measure for the distance the extrapolated starting point of the particle track has relative to the primary vertex of the event. For this selection a version of the track is used which is reconstructed by solely using information from the silicon tracker since this yields the highest precision for the impact parameter. The distance is calculated separately for the transverse plane (d_{xy}) and along the beam axis (d_z). A large distance is evidence that the track is not caused by a muon originating from the hard interaction (called “prompt muons”) but caused by a cosmic muon, a muon from an in-flight decay of a hadron or from pileup. The thresholds for the two quantities are: $d_{xy} < 2\,\text{mm}$ and $d_z < 5\,\text{mm}$.
- **Number of pixel hits > 0:** The requirement that at least one hit of the track is found in the pixel detector is a further way to suppress muons from in-flight decays since it is very likely that no pixel hit compatible with the track would be found if the in flight decay would happen behind the pixel detector.
- **Number of tracker layers with hits > 5:** This selection ensures a good p_T resolution of the track measured in the silicon tracker.

Modifications for High p_T Muon ID

In order to recover the efficiency loss for the identification of high p_T muons caused by the more challenging reconstruction of their tracks, some requirements on the track quality are weakened: The requirement on $\frac{\chi^2}{N_{dof}}$ is dropped and the muon candidate does not have to fulfill the particle flow muon identification anymore. Since the correct

---

[2] A muon segment is a consistent set of hits in one muon chamber which can be used as input for the global track fit.

measurement of the transverse momentum becomes more difficult due to a decreasing bending of the track, an additional requirement on the relative transverse momentum uncertainty is introduced in order to reject muons with largely mis-measured momentum: $(\frac{\Delta p_T}{p_T})$ has to be less than 30 %.

Isolation

The main property used to reject muons which originate from hadron decays within jets is the isolation. Isolation describes how much energy is carried by objects close to the muon candidate. Muons within jets are accompanied by many other jet constituents which leads to a large energy deposit close to the muon, while prompt muons are usually accompanied by very few (or none) particles with low energy. The isolation selection used in this analysis is based on the energy sum over all objects not identified as pileup that are located within a cone of $\Delta R = \sqrt{\Delta\phi^2 + \Delta\eta^2} < 0.4$ around the muon candidate (but excluding the muon candidate itself). The identification of pileup objects is done by checking if their tracks can be matched to the primary vertex. This is only possible for charged particles since trajectories of neutral particles cannot be measured. To account for neutral pileup objects, 50% of the charged pileup contribution is additionally subtracted from the isolation energy sum. The ratio of two charged pileup objects for every neutral pileup object is motivated by the isospin symmetry which predicts that on average two charged pions are produced for every neutral one. This had also been found to be a good approximation for the real pileup composition in previous investigations. To account for outliers, the neutral pileup subtraction is truncated to not be larger than the overall neutral object contribution to the isolation energy sum.

$$\begin{aligned} E_T^{iso} &= \sum E_T(chargedHad) + \\ &max(0, \sum E_T(neutralHad) + \sum E_T(photons) - 0.5 \cdot \sum E_T(chargedPU)) \end{aligned} \tag{7.1}$$

If the isolation energy sum is larger than 12% of the muon transverse momentum, the muon is rejected.

To cover potential differences in the description of the muon identification between measured data and simulation, an uncertainty of 1% is assigned to the identification efficiency. This value is derived from [59] where a scale factor of 0.99 was determined to correct the simulation for the efficiency observed in data. In the context of the MUSiC analysis scale factors derived from data should be avoided but the uncertainty of 1% was chosen to cover the difference. A similar approach was chosen to estimate the uncertainty on the probability that the object that is reconstructed as a muon is no true muon (called "misidentification probability"): In [62] large deviations in the order of 50% where observed between data and simulation for this quantity and therefore this value is chosen as the uncertainty in the MUSiC analysis. This uncertainty seems to be very large but the muon misidentification probability itself is very small so the overall effect of this uncertainty on the results is still small.

7.3. Electron

7.3.1. Reconstruction

Instead of using the default CMS electron reconstruction and identification, special developments for electrons with high energy are used in the MUSiC analysis (called "HEEPv4.1")[77]. Instead of switching from the default approach to the high energy approach at a specific energy threshold, as is done for muons, the high energy approach is used for the full energy range since it was found that it also provides sufficiently good results for electrons at low and medium energy. The main difference compared to the particle flow electrons is that the energy reconstruction is done using only information from the calorimeter. The tracker is merely used to measure the direction of the electron. This must be done since the standard algorithm sometimes discards the calorimeter information completely due to some mismatches and uses track information only which can lead to very high and wrong values of $\mathrm{p_T}$. Using only calorimeter information is feasible since the combined energy measurement is completely dominated by the calorimeter above $\mathrm{p_T^{ele}} > 25$ GeV (as shown in [77]). The track reconstruction is done using the so called "Gaussian sum filter"(gsf) [78] approach which accounts for the electron's energy loss due to bremsstrahlung and the resulting change of curvature resulting while performing the track fit. Details can be found in [78, 79]. The energy loss due to bremsstrahlung has also to be taken into account when reconstructing the energy of the electron with the calorimeter. Between 33% and 86% of the initial energy is radiated before the electron reaches the calorimeter depending on how much material it had to traverse. These photons hit the calorimeter in a strip in ϕ relative to the impact point of the electron due to the bending of the track. The algorithm that clusters together the energy deposits in the calorimeter was developed to add those photons to the electron calorimeter energy in order to obtain the initial electron energy. The final result of the clustering is called supercluster. Details on the clustering algorithm can be found in [77]. The difference between the energy reconstruction in recorded data and simulation is taken into account by assigning an uncertainty of 0.6% to the energy scale of electrons measured in the barrel and 1.5% to electrons measured in the endcaps [65].

7.3.2. Identification

The identification of electrons relies mainly on the properties of the energy deposition in the calorimeters. Charged hadrons like $\pi^{\pm}$ also produce tracks in the silicon tracker and deposit all their energy in the calorimeters but the shape of the particle shower in the calorimeter as well as the ratio of energy deposit in the electromagnetic calorimeter relative to the one in the hadronic calorimeter is different compared to electron induced signals. Another source for possible misidentification are photons which can produce an electron-positron pair early on in the detector. Those can be suppressed by exploiting properties of the track. Non prompt electrons which can be produced by hadron decays within jets are suppressed in the same manner as it is done for muons by requiring the electron candidate to be isolated. All electrons must have a transverse momentum larger than 25 GeV. The geometrical acceptance goes up to the pseudo-rapidity of $|\eta| < 2.5$

but excluding the barrel-endcap transition region $1.442 < |\eta| < 1.56$. The exclusion is done since the calorimeter isolation and the transverse shower shape selection, which are an important part of the electron identification, do not work there. In the following, a short overview of the electron identification selection is presented. Candidates which are measured in the endcaps have to fulfill a slightly different set of requirements compared to electrons measured in the barrel. Details can be found in [60].

Common criteria for barrel and endcap:

- **Track to calorimeter match in ϕ:** The difference between the ϕ value of the energy cluster associated with the candidate and the ϕ value determined from the track extrapolated in the calorimeter ($\Delta\phi_{\mathrm{in}}$) should be smaller than 0.06.

- **Ratio of energy measured in ECAL and HCAL:** The ratio of the candidate's energy measured in the hadronic calorimeter relative to the one measured in the electromagnetic calorimeter (H/E) must be smaller than 5%. This requirement especially suppresses misidentification of charged hadrons as electrons.

- **Missing track hits:** The number of missing hits in the innermost layers of the tracker in front of the first hit that is used by the gsf track fit must be smaller than two. This rejects photons which have produced an electron-positron pair early in the detector.

Additional criteria for candidates in the barrel:

- **Track to calorimeter match in η:** The difference between the η value of the energy cluster associated with the candidate and the η value determined from the track extrapolated in the calorimeter ($\Delta\eta_{\mathrm{in}}$) should be smaller than 0.005.

- **Transverse shower shape:** The transverse shower shape is investigated by either comparing the energy in the 2x5 (η x ϕ) calorimeter crystals (E_{2x5}) or the energy in the 1x5 calorimeter crystals (E_{1x5}) to the energy in the 5x5 crystals (E_{5x5}) centered around the seed crystal of the candidate super-cluster. If $E_{2x5}/E_{5x5} > 0.94$ or $E_{1x5}/E_{5x5} > 0.83$ the candidate passes this selection.

- **Transverse impact parameter:** The transverse impact parameter d_{xy} relative to the primary vertex has to be smaller than 0.2 mm. This selection is much more strict for electrons than for muons since it is needed to suppress the misidentification of photons as electrons due to photon conversion which is irrelevant in the case of muons.

Additional criteria for candidates in the endcap:

- **Track to calorimeter match in η:** The test is performed in the same way as in the barrel but the threshold is loosened to $\Delta\eta_{\mathrm{in}} < 0.007$.

- **Transverse shower shape:** The covariance ($\sigma_{\mathrm{i}\eta\mathrm{i}\eta}$) of the 5x5 matrix describing the energy weighted distance of each crystal relative to the seed in the 5x5 grid around this seed is used as the test quantity for the transverse shower shape (for exact definition see [60]). If $\sigma_{\mathrm{i}\eta\mathrm{i}\eta}$ is smaller than 0.03, the candidate passes this selection.

- **Transverse impact parameter:** The requirement on the transverse impact parameter $\mathrm{d_{xy}}$ is also loosened to 0.5 mm.

Isolation

Two different kinds of isolation quantities are checked which both have to be fulfilled in order for the electron candidate to be considered isolated. The first one is calculated using only tracker information ("tracker isolation") and the second one relies completely on calorimeter information ("calorimeter isolation").

- **Tracker isolation:** For this quantity the $\mathrm{p_T}$ of all tracks between an inner cone with $\Delta\mathrm{R} = 0.04$ and an outer cone with $\Delta\mathrm{R} = 0.3$ are summed up if they match two additional requirements: The $\mathrm{p_T}$ of the track has to be larger than 0.7 GeV and the difference of the track's minimum distance in z to the origin of ordinates and the candidate-track's minimum distance (Δz) has to be smaller than 0.2 cm. If the sum is smaller than 5 GeV, the electron candidate is considered to be isolated in the tracker. The exclusion of tracks located in the inner cone prevents tracks from converted bremsstrahlung photons being added to the isolation sum since their $\mathrm{p_T}$ actually belongs to the electron candidate. The requirement on Δz rejects tracks originating from pileup collisions. The tracker isolation is used in the same way for electron candidates in the barrel and in the endcaps.

- **Calorimeter isolation:** The calorimeter isolation is formed as the sum of the ECAL isolation and the HCAL depth one isolation (see below). For the ECAL isolation, the $\mathrm{E_T}$ of all crystals in the barrel with $\mathrm{E_T} > 80$ Mev (in the endcaps with $\mathrm{E_T} > 100$ Mev) is summed up if they are located within a cone of $\Delta\mathrm{R} = 0.3$ around the electron candidate. Excluded from this sum are all crystals within a smaller circle with radius equal to 3 crystals directly around the candidate and all crystals in a strip in ϕ direction with the width in η equal to 3 crystals. The exclusion of this strip prevents bremsstrahlung photons from entering the isolation.

  The HCAL depth one isolation is the sum over $\mathrm{E_T}$ of all HCAL towers of the first layer located between an inner cone of $\Delta\mathrm{R} = 0.15$ and an outer cone of $\Delta\mathrm{R} = 0.3$ around the electron candidate.

  In order to correct the calorimeter isolation for pileup influences, an estimator for the pileup $\mathrm{E_T}$ contribution to the isolation sum is calculated for each event. This is achieved by determining the mean pileup energy density (ρ) per event and by multiplying it with the effective area of the isolation cone. The effective area was determined to be approximately constant at 0.28 for all electron candidates (see [60]) but the mean pileup energy density has to be calculated for each event. This is done by identifying so called “quiet” areas in the detector which are free from contributions from the hard interaction. These areas are identified by the absence of tracks originating from the primary vertex. The energy density in those areas is assumed to be dominated by pileup.

The candidate is considered to be isolated if the sum of the tracker isolation and the calorimeter isolation minus the pileup contribution is smaller than $2\ \mathrm{GeV} + 0.03 \cdot \mathrm{E}_\mathrm{T}^\mathrm{ele}$ in the barrel or smaller than $2\ \mathrm{GeV} + 0.03 \cdot (\mathrm{E}_\mathrm{T}^\mathrm{ele} - 50\ \mathrm{GeV})$ in the endcaps for $\mathrm{E}_\mathrm{T}^\mathrm{ele} > 50\ \mathrm{GeV}$ (smaller than 2.5 GeV for $\mathrm{E}_\mathrm{T}^\mathrm{ele} < 50\ \mathrm{GeV}$).

An uncertainty of 2% is assigned to the electron identification efficiency based on observed deviations between simulation and measurement [60](Figure 5.18) and 100% on the probability that an object is falsely identified as an electron (misidentification probability) [62](Table 15 compared with Table 16).

7.4. Photon

7.4.1. Reconstruction

The photon reconstruction [80] is mainly done with information from the electromagnetic calorimeter since the photon does not produce signals in the tracker as long as it does not convert into an electron-positron pair. The clustering algorithm in the calorimeter is not dedicated to any specific object and the photon reconstruction uses the same superclusters that are used by the electron reconstruction (see section above). In fact, a large portion of the photons do not reach the calorimeter undisturbed but convert into an electron-positron pair in the tracker. In this case the energy of the photon is not measured in the calorimeter directly but the energy of those secondary particles. Due to this, the energy reconstruction of photon candidates is performed in two different ways: In case no conversion has occurred, the energy sum of a simple cluster of 5x5 crystals around a seed crystal is used while in the conversion case the electron energy reconstruction algorithm is used. The decision whether the photon has converted or not is based on the R_9 variable. This variable is defined as the energy sum of the 3x3 crystals centered on the crystal with the most energy of a supercluster divided by the full energy of the supercluster. In the case of $\mathrm{R}_9 > 0.94$ in the barrel ($\mathrm{R}_9 > 0.95$ in the endcaps), the photon candidate is assumed to be unconverted. In the case that a conversion happened early enough to produce signals in three layers of the tracker, track fits are performed for the electron and positron emerging from the conversion. These tracks are used to gain additional information for identification and isolation purposes but do not enter the energy measurement. The uncertainty on the photon energy scale is assumed to be 0.6% [65] for photons in the barrel ($|\eta| < 1.442$). Photons that are measured in the endcaps are not used in this analysis since the modeling of their misidentification probability in simulation was found to be problematic.

7.4.2. Identification

The main sources for photon misidentification are electrons, and meson decays. The discrimination against electrons is done by using the inverted approach as it is done to discriminate electrons against photons and meson decays are dealt with by exploiting isolation and shower shape requirements similar to those used for electron identification:

- **Pixel seed electron veto:** To suppress electrons being misidentified as photons, information from the pixel detector are used. An electron produces signals in the detector starting from the very first layer of pixels while photon conversion into electron-positron pair happens somewhat later in the detector. If a pixel seed consisting of at least two hits is found for a track that is consistent with the calorimeter cluster of the photon candidate, the candidate is rejected.

- **Transverse shower shape:** Again, the quality $\sigma_{\mathrm{i}\eta\mathrm{i}\eta}$ is used which was introduced in the section on electron reconstruction. If $\sigma_{\mathrm{i}\eta\mathrm{i}\eta}$ is larger than 0.011 the candidate is rejected.

- **HCAL to ECAL energy ration:** The ratio of the energy measured in the HCAL tower directly behind the supercluster seed crystal relative to the energy of the supercluster (H/E) must be smaller than 0.05.

All photon candidates have to fulfill acceptance requirements of $\mathrm{p_T} > 25$ GeV and $|\eta| < 1.442$.

Isolation

The isolation test for photon candidates is divided into three different parts: a) the charged hadron isolation, b) the neutral hadron isolation and c) the photon isolation. For all of those, the transverse momenta of all corresponding objects reconstructed by the particle flow algorithm within a cone with $\Delta\mathrm{R} = 0.3$ around the candidate are summed up. After that, a pileup correction based on the mean pileup energy density similar to the one used for electrons is applied to the neutral hadron and photon isolation sums. The difference between the methods for electrons and photons is that the effective area is not constant for photons (as is the case for electrons) but depends on the η direction of the photon candidate. Additionally, all particle flow photons are rejected from the photon isolation sum that have a $\Delta\eta < 0.015$ relative to the candidate object and all charged hadrons are rejected from the charged hadron isolation sum that are closer than $\Delta\mathrm{R} = 0.02$. The thresholds for the three isolation sums, which all have to be met in order for a candidate object to be considered isolated, are:

- **Charged hadron isolation:** $\mathrm{Iso_{chad}} < 0.5$ GeV

- **Neutral hadron isolation:** $\mathrm{Iso_{nhad}} < 1.5\ \mathrm{GeV} + 0.04 \cdot \mathrm{p_T^{\gamma}}$

- **Photon isolation:** $\mathrm{Iso_{\gamma}} < 1.0\ \mathrm{GeV} + 0.005 \cdot \mathrm{p_T^{\gamma}}$

The uncertainty on the efficiency and misidentification probability is again derived from the difference observed between simulation and measurement for both quantities with 3% being assigned to the efficiency uncertainty [61] and 100% to the misidentification probability uncertainty [63].

7.5. Jet

7.5.1. Reconstruction

The main task of a jet reconstruction algorithm is to identify all particles that have emerged from a single initial particle and group them together into an object that represents the kinematics of this initial particle. The jet reconstruction procedure in this analysis uses the so called "anti-kt" algorithm [81] to assign particles to jets. It is an iterative clustering algorithm that uses a $\mathrm{p_T}$ weighted distance parameter (Equation 7.2) to decide whether an object should be assigned to the jet or not. The clustering is performed on objects called "protojets" which can either be single particles or combined objects consisting of more than one particle after they have been already clustered together. The particle collection produced by the particle flow algorithm is used as input for the anti-kt algorithm with all particles being considered as initial protojets. The algorithms starts by identifying the particle with the highest energy which is used as the initial seed for the clustering and then combines it with the protojet closest to it. The distance measure

$$d_{ij} = min(k_{Ti}^{-2}, k_{Tj}^{-2}) \frac{(\Delta R)^2}{r^2} \tag{7.2}$$

is used for this with $\mathrm{k_T}$ being the transverse momentum of the two protojets and $\Delta\mathrm{R}$ the distance between the two in (η,ϕ). The parameter r is used to adjust the algorithm and is set to 0.5 in this analysis. If the smallest possible distance $\mathrm{d_{ij}}$ of protojet "i" to any other protojet in the collection is larger than $\mathrm{d_{iB}} = \mathrm{k_{Ti}^{-2}}$, protojet "i" is defined as a final jet and removed from the collection of protojets. After that the algorithm starts again by searching for the protojet with the highest energy to use as the next seed. This continues until no protojets are left. The anti-kt algorithm is used as the standard jet reconstruction algorithm in CMS since it is infrared and colinear safe and it behaves like an idealized cone algorithm (jets with only soft fragmentation are conically shaped).

The final step of the jet reconstruction is the energy calibration which is much more complex than for any of the previously explained particles since it depends on many different factors. The goal is to calibrate the jet energy in a way that it represents the energy of the initial parton with maximum accuracy. It is done centrally by CMS jet object experts and detailed information can be found in [66]. Systematic uncertainties on the jet energy scale have to be taken into account as well. They are provided as a consistent set of uncertainty values depending on the jet's $\mathrm{p_T}$ and η. The values of this uncertainty are typically a few percent.

7.5.2. Identification

A loose set of identification criteria is applied to jet candidates since misidentification as one of the other previously described particles as jets is not an issue here. Well identified and isolated particles cannot be misidentified as jets since the jet candidate collection is cleaned against those objects during the MUSiC overlap removal (see 5.4.1). If any of those particles does not fulfill the dedicated identification or isolation, it is not really a problem either since the rate of this is much smaller than the occurrence of real jets. It could even be argued that it is better to retain those objects as jets instead of losing them completely. However, the jet identification is needed to suppress jets that are reconstructed from detector noise instead of real particles emerging from the collision. To achieve this, the following set of requirements is used which is called “LooseJetID”:

- **Neutral hadron fraction:** The fraction of neutral hadron energy contribution relative to the full jet energy must be smaller than 0.99.
- **Neutral electromagnetic fraction:** The fraction of neutral electromagnetic energy contribution relative to the full jet energy must be smaller than 0.99.
- **Number of constituents:** Number of particle flow objects clustered together for this jet must be larger than one.
- **Muon fraction:** Energy fraction of the jet contributed by muons must be smaller than 0.8.
- **Charged hadron fraction:** The fraction of charged hadron energy contribution relative to the full jet energy must be greater than 0.
- **Charged electromagnetic fraction:** The fraction of charged electromagnetic energy contribution relative to the full jet energy must be smaller than 0.99.
- **Charged object multiplicity:** The number of charged constituents in the jet must be greater than zero.

Jets must have a transverse momentum larger than 50 GeV and must be within a pseudo-rapidity range of $|\eta| < 2.4$ to be considered in the MUSiC analysis. The relatively large threshold for $\mathrm{p_T}$ is chosen to veto soft hadronic activity which is problematic to simulate. By restricting jets to the acceptance of the tracker it is ensured that the full information can be used for the reconstruction.

7.6. MET

The missing transverse momentum vector ($\boldsymbol{p_T^{miss}}$) in an event is defined as the negative vectorial sum over the transverse momentum of all objects measured in the detector:

$$\boldsymbol{p_T^{miss}} = -\sum^{objects} \boldsymbol{p_T^{i}} \tag{7.3}$$

These objects include the ones discussed in this chapter as well as all other additional objects measured by the detector which are not used by the MUSiC analysis. The magnitude of the $\boldsymbol{p_T^{miss}}$ vector which is called “missing transverse energy” (MET)[3] is a measure for the momentum that has left the detector undetected since the transverse momentum of the initial state is approximately zero and it should add up to zero in the final state, too, as long as all contributions are measured. This quantity can therefore be used to deduce information on final state particles produced in an event which have a life-time long enough to leave the detector but do not interact with the detector in a way to produce a measurable signal. The only known particle of that type is the neutrino but many theories predict new particles with the same properties whereof dark matter is the most prominent example. A precise momentum and energy measurement of all objects within an event is crucial for the reconstruction of MET since wrongly measured momentum would spoil the momentum sum and lead to a value of MET that is not correlated with an undetectable particle. The second important feature which is needed for a precise MET measurement is that the detector covers as much distance in η as possible since particles that leave the detector outside the acceptance do also have an influence on the momentum sum. This is the reason why CMS has equipped the hadron forward calorimeters which extend the coverage of the detector up to $\eta = 5.2$.

To further improve the MET reconstruction quality, three different types of corrections are applied to it: Pileup correction, Jet energy scale corrections and xy-shift corrections. A short explanation of the corrections are given in the following. For details see [67].

- **Pileup correction:** The large number of objects with relatively low energy produced in typical pileup interactions can be a problem during the calculation of MET since the calorimeter is calibrated for much higher energies and therefore the measurement of particles with low energy will be systematically off. This is especially a problem since it only affects neutral particles since charged particles are measured very precisely in the tracker. The correction aims at removing all contributions caused by pileup particles from MET. The identification of charged contributions from pileup is done by assigning tracks to the interaction vertices which is of course not possible for neutral contributions. They are instead identified indirectly: It is assumed that the pileup interactions do not contain genuine MET which is true for the vast majority of cases which then implies that the neutral component must exactly cancel the imbalance in the vectorial momentum sum of the charged contribution.

- **Jet energy scale corrections:** Instead of adding up the momenta of all particles from the hard interaction directly, the contribution of particles that have been clustered together during the jet reconstruction are replaced by the momentum of the jet object for which various corrections have been calculated previously.

---

[3] The reason for the word “energy” instead of “momentum” in the name is historical: In previous experiments it was calculated by adding up all transverse energy contributions measured in the calorimeter which is approximately equal to the transverse momentum as long as the mass of the particles is small compared to their energy. Only due to the usage of the particle flow algorithms it has become possible to add up the momenta directly.

- **xy-shift corrections:** Due to the symmetry of CMS, MET should on average not depend on the angle ϕ. However, an asymmetry was found in data which was caused by alignment offsets of the detector and asymmetries in the hadron forward calorimeters. This is corrected by shifting the momentum vector of all objects in x and y direction to counteract the asymmetry. The shift vectors have been determined by MET object experts.

Despite of all the corrections, it is impossible to gain a perfect description and small values of MET will be present in every event whether there is genuine MET or not. Therefore, in order to gain a meaningful differentiation of events into classes with and without MET, a threshold of 50 GeV is applied which MET has to exceed in order to be considered in terms of the MUSiC analysis. The uncertainty on MET is caused by the uncertainties on the momentum reconstruction of its components which have been discussed in the previous sections with the exception of one: All signals within the detector which have not been identified as one of the above objects still enters the calculation of MET and the uncertainty on those contribution is estimated to 10% [67].

7.7. Event quality

Since every physics object in every event that enters the analysis has an influence on the result of the MUSiC classification, it is very important to restrict the analysis to those events in which every aspect of the reconstruction has worked without any problems. This is not yet covered by the event certification described in Chapter 6 which contains looser requirements on the event quality since there are other analyses in CMS which are not affected by all reconstruction problems critical for MUSiC. For example, any analysis which is not interested in MET does not need to reject events with a wrong calculation of MET. In order to select good events for the MUSiC analysis, two additional aspects are checked: Each event must contain at least one good primary vertex and the event must pass a set of filters developed by CMS detector experts. A primary vertex is considered to be good if more than four tracks have been used to reconstruct it and its distance to the interaction point has to be smaller than 24 cm in z-direction and 2 cm in r-direction (within the transverse plane). An overview of the additional event quality filters used in this analysis is given in the following list [82]:

- **Scraping filter:** If an event contains more than ten tracks, 25% of those must be reconstructed with high quality or the event is rejected.

- **Tight beam halo filter:** The LHC proton beams are accompanied by a halo of secondary particles which emerge from collisions of protons with residual gas within the beampipe or with collimators. This filter rejects events which are contaminated with beam halo particles that have reached CMS and caused a signal in the detector.

- **HCAL laser filter:** The energy response of the HCAL is calibrated during data-taking by firing a laser in the calorimeter and adjust the measurement to the known laser properties. This should be done between two bunch crossings but sometimes the timing is off and the calibration event happens during a collision event. All events which are affected by this are rejected.

- **ECAL dead cell trigger primitive filter:** About 1% of the crystals in the ECAL do not work properly and are removed from the event reconstruction ("dead cells"). If information from the surrounding crystals indicate that a considerable amount of energy has been deposited in this dead cell, the event is rejected to prevent a mismeasurement of MET.
- **Tracking failure filter:** Events with a large displaced primary vertex which causes the track reconstruction to fail are rejected by this filter.
- **Bad ECAL endcap supercrystal filter:** Two 5x5 ECAl crystal regions occasionally produce anomalous, high amplitude pulses whose cause is not yet fully understood. Events affected by this are removed.
- **ECAL laser correction filter:** The ECAL contains some crystals with anomalous high energy calibration factors. Events are rejected if they are affected by energy measured in those crystals.
- **Anomalous tracks filter:** Events are rejected if the track reconstruction partially failed or if the tracking was affected by coherent noise in tracker strips.

The overall number of measured events rejected by these filters is very small ($\approx 2\%$) and therefore it is not necessary to correct the number of simulated events for the effect of the filters.

Finally, events are rejected when the leptons that have triggered the recording of an event have a p_T too close to the p_T threshold of the activated trigger. This veto is not designed to exclude events with bad reconstruction quality but which are known to be problematic to simulate. The challenging part of the simulation concerns the correct description of the trigger selection efficiency: The efficiency is not directly at its maximum value once the kinematic requirements of the trigger path are matched but rises steeply before it reaches a constant value. This behavior of the trigger selection can be seen in Figure 7.1 which shows the efficiency of the single electron trigger in the barrel and the endcaps separately depending on the transverse energy of the electron. Both plots show a steeply rising distribution which reaches a plateau at a transverse energy of approximately 100 GeV.

It is very complicated to simulate the behavior of this trigger efficiency turn-on effect correctly during the generation of the Standard Model prediction and a correct description cannot be guaranteed. In order to avoid a mismodeling, events which are located in the trigger turn-on region are excluded from the analysis. For this purpose, an additional p_T requirement is set on the leptons which have triggered the recording of an event. The threshold is chosen for each trigger path in a way that the efficiency of this trigger is approximately constant above this value. The different thresholds for all triggers used in this analysis can be found in Table 7.2.

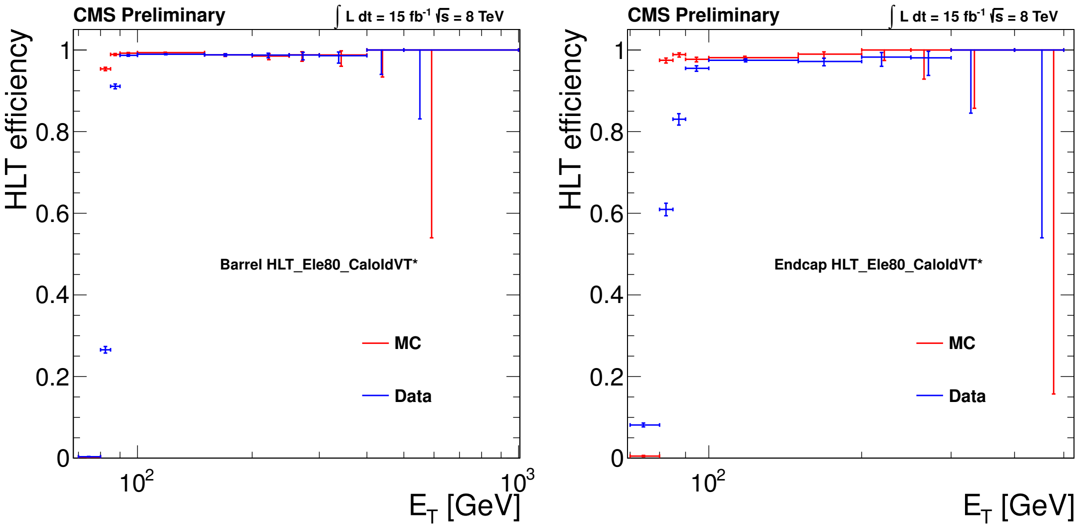

Figure 7.1.: Efficiency of the single electron trigger depending on the transverse energy of the electron [83]. The left plot shows the distribution for electrons measured in the barrel and the right plot for electrons measured in the endcaps. The distribution of the efficiency reaches a plateau at approximately 100 GeV for both plots.

Trigger type	Additional requirement
single muon	1μ with $p_T > 30$ GeV
single electron	1e with $p_T > 100$ GeV
double muon	2μ with $p_T > 25$ GeV
double electron	2e with $p_T > 25$ GeV

Table 7.2.: Additional p_T requirements on triggering object for each used trigger path. “Trigger type” corresponds to the names in Table 6.1.

8. MUSiC Classification Results

In this chapter, an overview of the results of the MUSiC classification algorithm (described in Chapter 5) will be given. These results act as the input for the limit calculation tool which will be described in the next chapter. The classification was performed on the data collected in the year 2012 which are described in Chapter 6 after they have been prepared by the methods described in Chapter 7.

8.1. General overview

The overall number of measured data events that pass the trigger and event quality selection and enter the classification is $n_{\mathrm{data}} = 8.8 \cdot 10^7$. This is in good agreement with the expected number of Standard Model events $n_{\mathrm{SM}} = (9 \pm 0.7) \cdot 10^7$ passing the same selection. The measured data events as well as the simulated Standard Model are sorted into 307 exclusive, 374 inclusive and 351 jet-inclusive event classes with $\approx 70\%$ of those contain at least one electron, $\approx 70\%$ at least one muon and $\approx 40\%$ at least one photon. MET exceeds the threshold of 50 GeV in $\approx 45\%$ of those classes. A total of 221 exclusive, 272 inclusive and 255 jet-inclusive classes contain at least one bin region with a valid Standard Model description according to the restrictions presented in Section 5.4.2. The overall number of valid bin regions is approximately $3 \cdot 10^6$.

8.2. Informational content of event classes

In this section, the informational content of the event class data structure will be presented which is used as the input of the limit calculation tool. Additionally, the differences between the three types of event classes will be explained which each provide advantages in terms of sensitivity for different types of signals. For this purpose I will discuss one example event class of each type and explain its different features. The three event classes: `1e + MET excl.`, `1e + MET incl.` and `1e + MET jet-incl.` have been chosen as they can illustrate most features while not being too complicated. The explicit particle content was chosen to be the same for all three classes so that they are directly comparable.

Figure 8.1 shows the event yield and relative uncertainty of the `1e + MET excl.` class depending on $\sum p_{\mathrm{T}}$. In the upper plot, the black dots indicate the event yield measured in data and the Standard Model expectation is shown as a stack of colored areas, each color denoting the contribution of a specific process to the full event yield. The gray shaded area shows the combined systematic uncertainty on the Standard Model expectation in each bin. In addition, the full information on the composition of the systematic uncertainty is conserved in order to enable the correct combination of uncertainties considering bin-to-bin correlations when summing up bins into bin regions. The lower plot of Figure 8.1 shows the contribution of the systematic uncertainties on various quantities on the total uncertainty in each bin. Since MET is present as an additional physics object in this event class, the distributions of M_T and MET are also created and can be found in Figure 8.2. The Standard Model expectation of all three kinematic distributions is dominated by the leptonic decay of the W-boson which is expected since the final state matches the object content of the event class exactly. The peak of the resonant W production cannot be seen in the distributions since the p_T threshold on MET is too high. The distribution of M_T extends down close to zero since there are events where the W is boosted transverse to the beam line which can lead to values of p_T for the electron and values of MET above the object thresholds even if the transverse mass of the electron-MET combination is low. The peak in the MET distribution at 200 GeV is caused by the fact that we require the electron that activated the single electron trigger to have 100 GeV transverse momentum (see Table 7.2). Since most of the events of the W production should lead to the same amount of MET as the electron has transverse momentum, this results in a peak at 200 GeV. The same kinematic distributions and systematic uncertainty information are also stored for the inclusive and jet-inclusive event classes. In the chosen example of `1e + MET incl.` and `1e + MET jet-incl.` $\sum p_T$ and M_T is again calculated for the electron-MET object pair which is indicated by the explicit part of the event class name. It is possible that events that enter the inclusive class contain more than one electron. In this case the one with the highest p_T is used to calculate the kinematic quantities. All events that are included in the jet-inclusive class are also contained in the inclusive class and the event content of the exclusive class is in turn a subset of the jet-inclusive class (as long as the explicit particle content is the same). In Figure 8.3 the $\sum p_T$ distributions are shown for the `1e + MET incl.` and `1e + MET jet-incl.` event classes. The subset relation between the three example event classes is reflected in the fact that the $\sum p_T$ distribution of the inclusive class contains more entries ($n_{obs} = 3.9 \cdot 10^5$, $n_{SM} = 3.7 \cdot 10^5$) than the one of the jet-inclusive ($n_{obs} = 2.8 \cdot 10^5$, $n_{SM} = 2.7 \cdot 10^5$) which in turn contains more than the one of the exclusive class ($n_{obs} = 4.3 \cdot 10^4$, $n_{SM} = 4.2 \cdot 10^4$) (Figure 8.1). This implies that when testing a new signal with the model unspecific limits, the inclusive classes will have the highest signal acceptance while the exclusive classes should have the highest purity. Which of those qualities would gain the highest sensitivity depends on the specific properties of the signal.

One interesting feature concerning the trigger selection can be seen when comparing the two plots in Figure 8.3 and the upper one in Figure 8.1: The `1e + MET jet-incl.` and `1e + MET excl.` event classes can only contain events that are triggered by the single electron trigger since the events must not contain any additional leptons. This results in a minimum value of $\sum p_T$ of 150 GeV given by the minimum value for MET of 50 GeV and the minimum electron p_T requirement of 100 GeV caused by the single electron trigger. The `1e + MET incl.` on the other hand can contain additional leptons and can therefore contain events that are selected by other triggers. This leads to additional entries in the $\sum p_T$ distribution below 150 GeV which are expected to originate mainly from Drell-Yan processes since they contain two leptons in the final state and can therefore be triggered by di-lepton triggers.

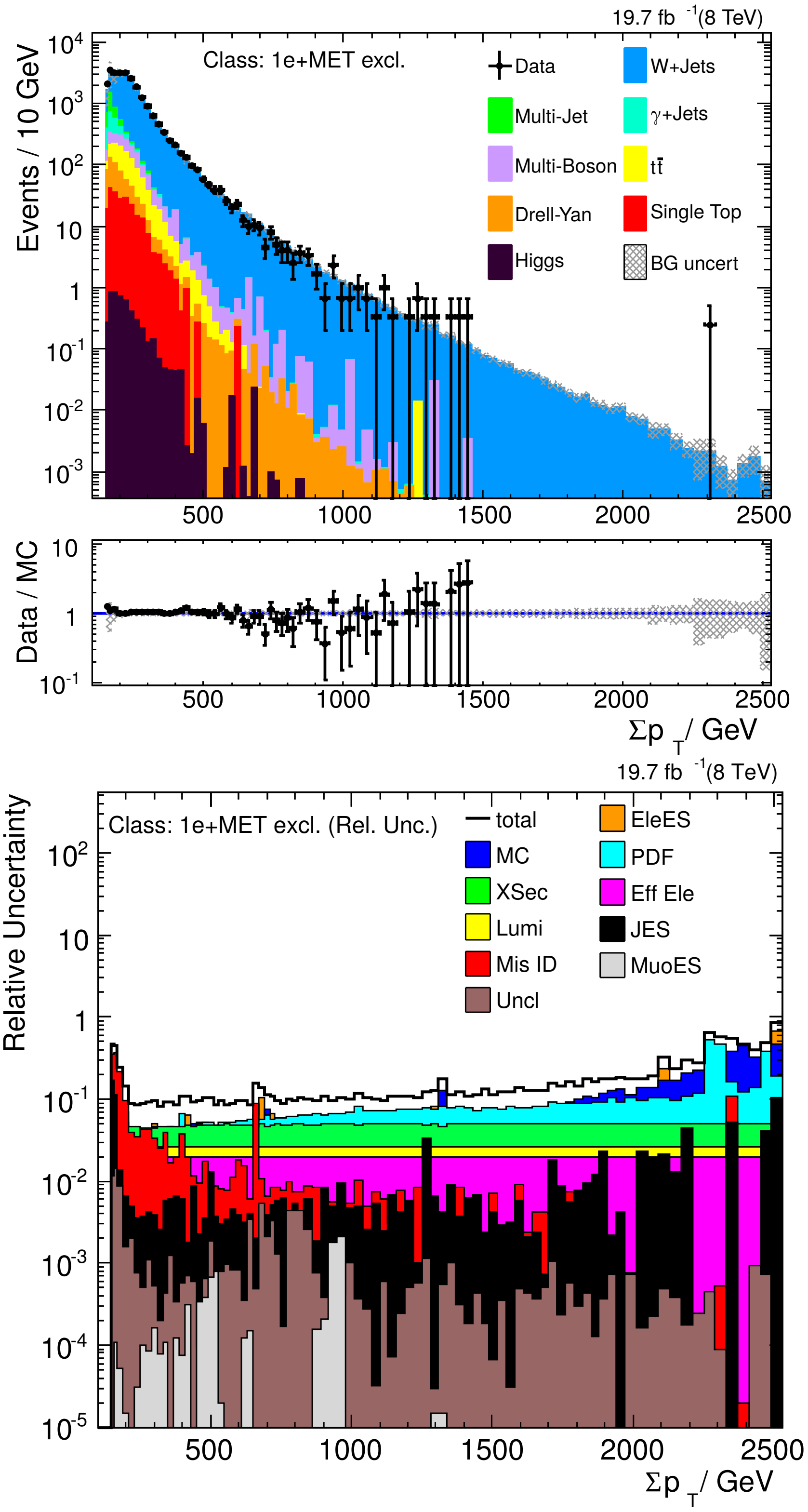

Figure 8.1.: Event yield and relative uncertainty distribution of the `1e + MET excl.` class depending on $\sum p_T$.

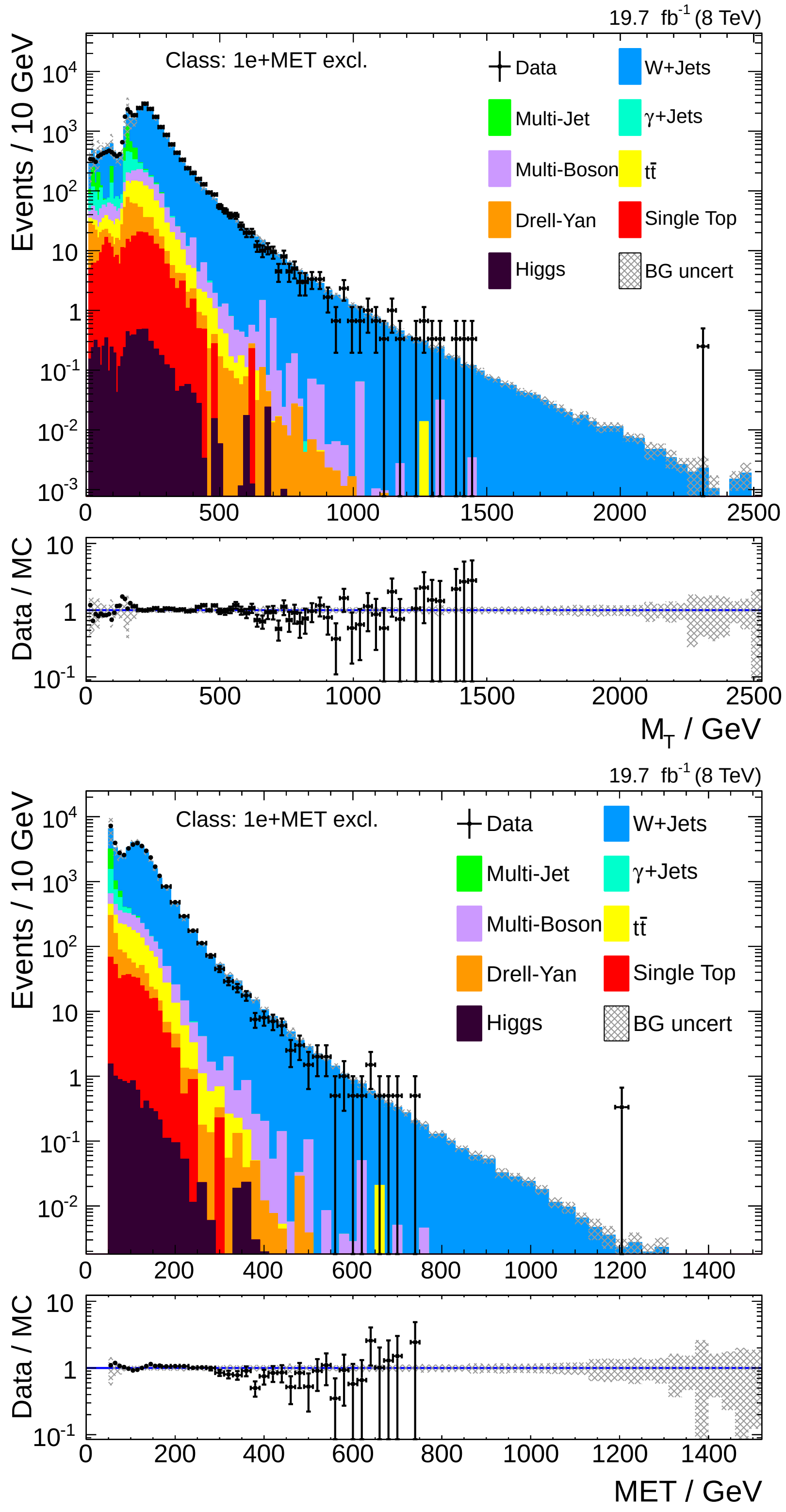

Figure 8.2.: Event yield of the `1e + MET excl.` class depending on M_T and MET. The structures at the beginning of both spectra are caused by trigger thresholds and requirements on the transverse momentum of the electron and the minimum value of MET.

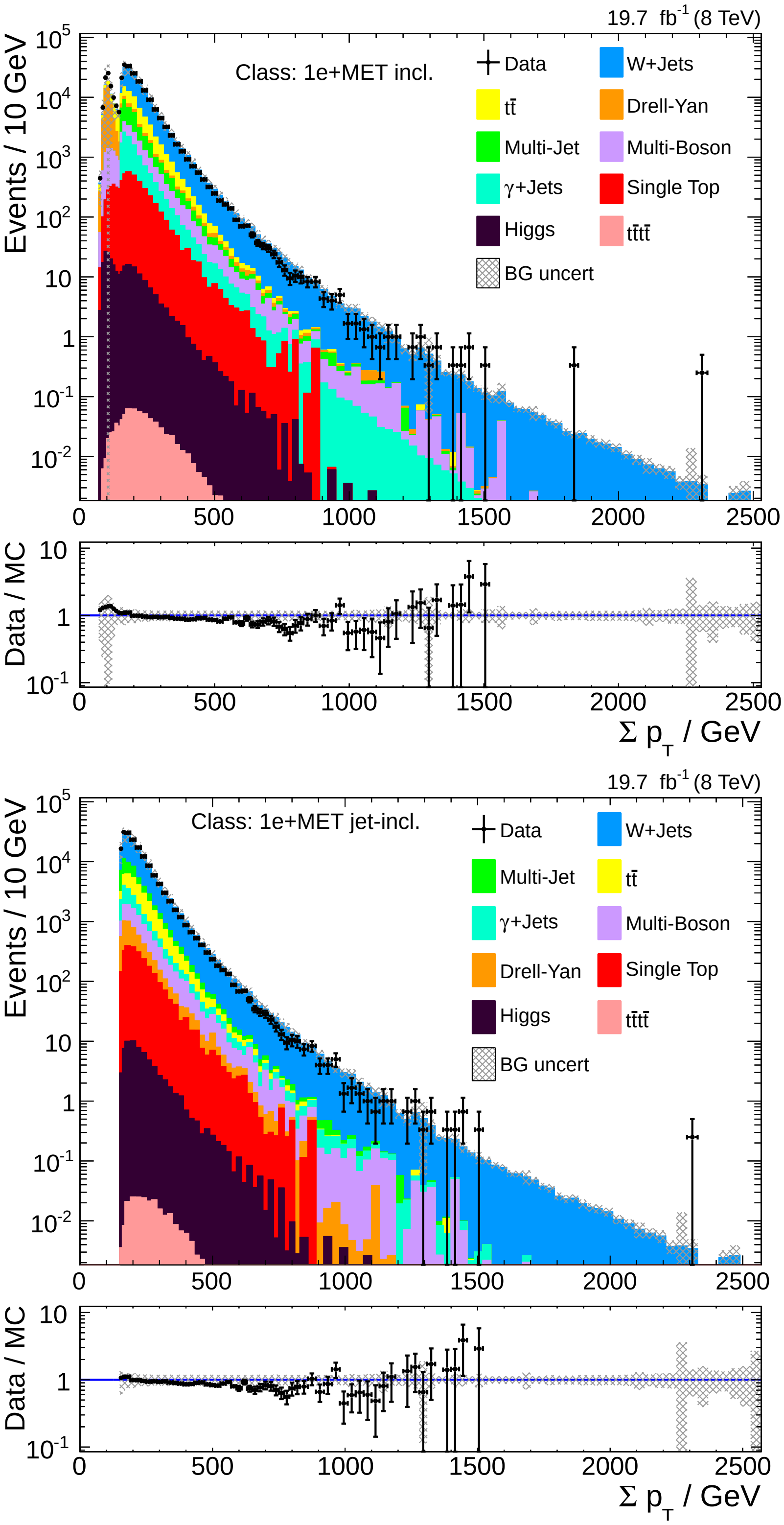

Figure 8.3.: Event yield of the `1e + MET incl.` and `1e + MET jet-incl.` class depending on $\sum p_T$.

8.3. Degree of agreement between measurement and SM expectation

The validity of exclusion limits on signal processes is dependent on the quality of the background description used in the statistical test. Deviations in some regions of the analysis do not necessarily render the background description invalid since they could occur by chance due to the large number of overall possible regions under investigation or even by a signal. However, a good agreement between Standard Model expectation and measurement over a majority of all regions is a plausible indicator that the overall modeling of the Standard Model should be applicable. Information on the agreement between Standard Model expectation and measurement can be deduced from the results of the MUSiC scan for deviations which is described briefly in the following section. More details can be found in in [1].

8.3.1. MUSiC scan for deviations

In the MUSiC analysis a scan for deviations between the observed number of events and the expected number of Standard Model event is performed that uses a p-value (called $\mathrm{p_{data}}$) to quantify the statistical significance of observed deviations:

$$p_{data} = \begin{cases} \sum\limits_{i=N_{\mathrm{obs}}}^{\infty} C \cdot \int\limits_{0}^{\infty} \mathrm{d}\lambda \, \exp\left(-\frac{(\lambda - N_{\mathrm{SM}})^2}{2\,\sigma_{\mathrm{SM}}^2}\right) \cdot \frac{\mathrm{e}^{-\lambda}\,\lambda^i}{i!}, & \text{if } N_{\mathrm{obs}} \geq N_{\mathrm{SM}} \\ \sum\limits_{i=0}^{N_{\mathrm{obs}}} C \cdot \int\limits_{0}^{\infty} \mathrm{d}\lambda \, \exp\left(-\frac{(\lambda - N_{\mathrm{SM}})^2}{2\,\sigma_{\mathrm{SM}}^2}\right) \cdot \frac{\mathrm{e}^{-\lambda}\,\lambda^i}{i!}, & \text{if } N_{\mathrm{obs}} < N_{\mathrm{SM}} \end{cases}$$

The p-value describes the probability to observe a deviation more extreme than the one observed in data given that the Standard Model only hypothesis is true. It is calculated separately for the two cases that the observed number of events is larger or smaller than the expected number of Standard Model events. The probability to observe a specific number of events is calculated as the convolution of a Poisson distribution with a Gaussian distribution. The Poisson distribution models the statistical behavior of the counting experiment and the Gaussian distribution models the systematic uncertainty of the Standard Model expectation. The p-value is determined as the sum of the probabilities corresponding to each possible outcome leading to a more extreme deviation than observed in data. The factor “C” is used to scale the Gaussian distribution, which is truncated at zero, to unity.

This p-value is evaluated for every valid region of every kinematic distribution (see section 5.4.2) of each event class in order to find the region with the most significant deviation in each distribution. This region is called the “Region of Interest” (RoI) and the p-value describes the local significance of the deviation.

The global significance of the most significant deviation is calculated in each distribution in a second step. In contrast to the local significance which describes the probability to observe a more extreme deviation in this exact region, the global significance describes the probability to observe a more extreme deviation anywhere in the distribution. This is done to take into account the so called look-elsewhere effect: When a larger number of search regions is investigated, it becomes more likely to observe a significant deviation in any of those regions. The global significance (called $\tilde{\mathrm{p}}$) is determined with a Monte Carlo approach for each kinematic distribution of every event class separately: First, many random pseudo-data distributions are produced ($\mathcal{O}(10^5)$) according to the statistical expectation of the Standard Model only hypothesis of that kinematic distribution. For each of those pseudo-data distributions, the RoI is determined and the distribution of $\mathrm{p}_{\mathrm{data}}^{\mathrm{RoI}}$ is constructed. The global significance is then determined as the fraction of pseudo-data distributions with a value of $\mathrm{p}_{\mathrm{data}}^{\mathrm{RoI}}$ smaller than the one observed in data relative to the overall number of pseudo-data distributions:

$$\tilde{p} = \frac{\text{number of pseudo-data distributions with } p_{\text{pseudo-data}}^{\text{RoI}} < p_{\text{data}}^{\text{RoI}}}{\text{total number of pseudo-data distributions}} \tag{8.1}$$

An example for this method is illustrated in Figure 8.4.

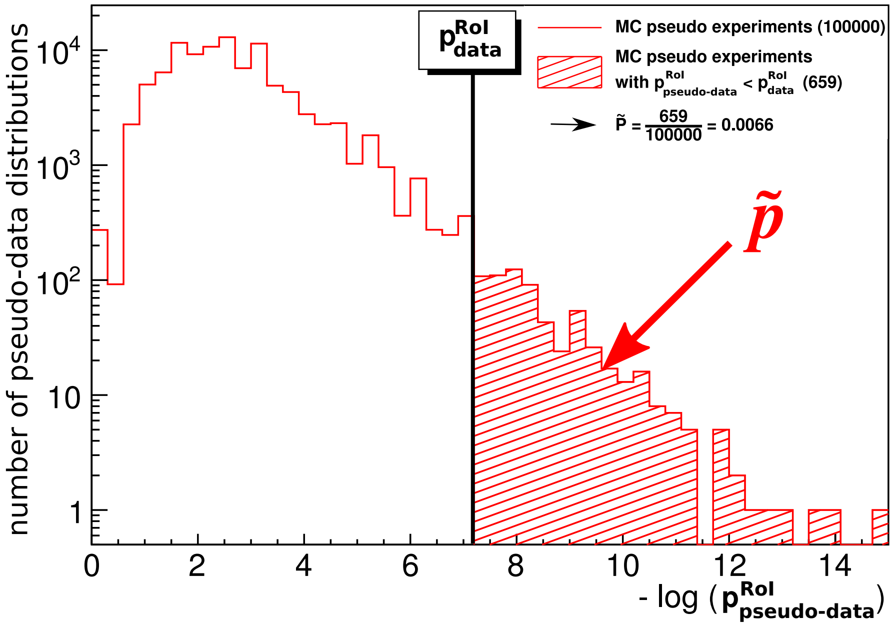

Figure 8.4.: Exemplary calculation of $\tilde{\mathrm{p}}$ using pseudo-data.

8.3.2. Global scan results

The results of the full MUSiC scan for deviations shows that the overall agreement between observed data and Standard Model expectation is good over the full phase space investigated by MUSiC. To summarize the information on the agreement, three plots taken from [1] are featured in the Figures 8.5, 8.6, 8.7 which show the distributions of the global significances of the strongest deviation in each distribution of all exclusive classes found by the MUSiC scan. The number of classes is plotted against the negative decadic logarithm of $\tilde{\mathrm{p}}$ in order to emphasize small values. Small significances are of special interest since they denote strong deviations. In addition to the distribution of the global significances observed in data (black dots), various statistical measures are shown of the expected distribution calculated under the assumption that the Standard-Model-only hypothesis is true: The cyan line denotes the mean number of distributions calculated from a large number of pseudo-experiments; the dotted line shows the expected median of the distribution and the two bands indicate the expected one and two sigma intervals of the distribution. No deviation was found in data that exceeds 3σ significance and all observed deviations are in reasonable agreement with the expectation from the Standard Model-only hypothesis. The corresponding distributions for the inclusive and jet-inclusive classes can be found in [1].

The overall good agreement between the observed data and the expectation according to the Standard Model indicates that the Standard Model simulation used in this analysis is sufficiently reliable in order to calculate exclusion limits based on its predictions. The calculation of those limits will be discussed in the following chapters.

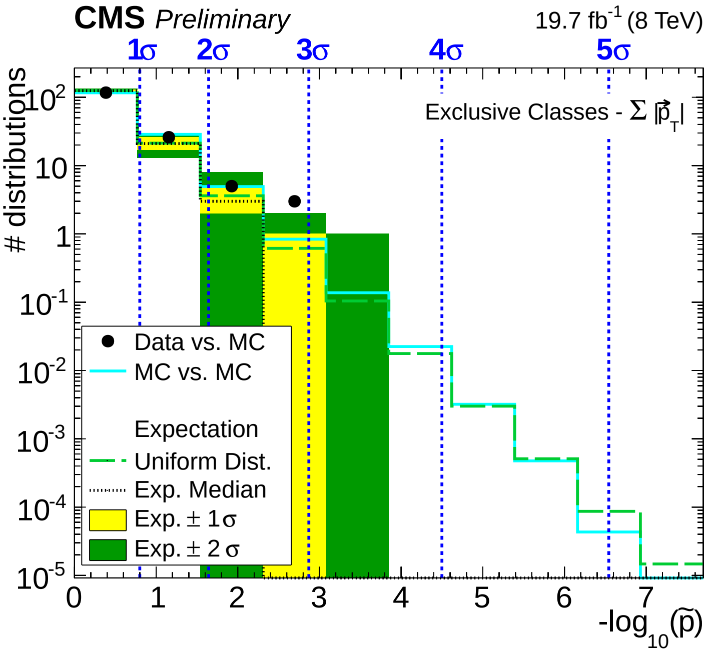

Figure 8.5.: $\tilde{p}$ distributions of $\sum p_T$distributions of the exclusive event classes (taken from [2]).

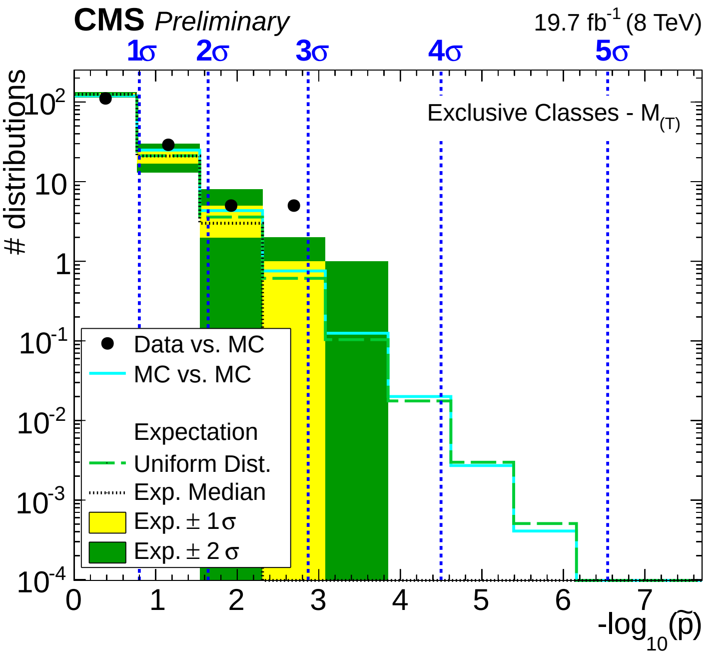

Figure 8.6.: p̃ distributions of $M_{(T)}$ distributions of the exclusive event classes (taken from [2]).

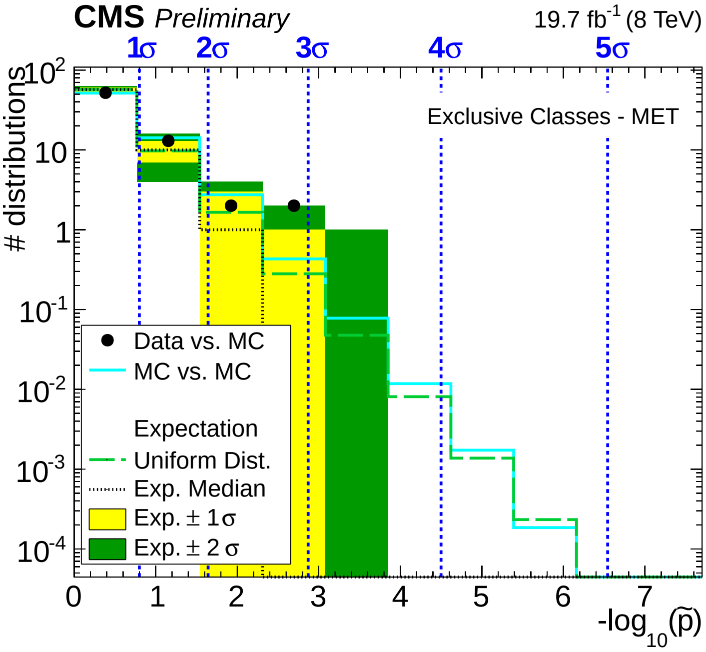

Figure 8.7.: p̃ distributions of MET distributions of the exclusive event classes (taken from [2]).

Part III.

Exclusion Limits and Reinterpretation

9. The METAL Project

9.1. Motivation

A large number of theories and models exist which extend the Standard Model of particle physics and describe additional proposed processes (called “signal”). The MUSiC project so far aims at finding deviations between the data and the Standard Model prediction which could be signs for new signals but it does not yet provide any information that could be use to constrain the parameters of any signal model on the basis of the analysed data. The standard approach pursued by dedicated analyses is to directly calculate exclusion limits on parameters of the model they are investigating, in case that they do not find evidence for the existence of that model in the data. The model unspecific search does not investigate any specific model but the information gained during the MUSiC classification provides a promising opportunity to constrain any given model afterwards. Since the MUSiC classification constructs kinematic distributions for a large variety of final states, some sensitivity can be expected for many different signal models.

The goal of the work described in this thesis is the development of a software framework called ‘METAL”(MUSiC Embedded Toolkit for Ascertaining Limits) which performs this reprocessing of the classification results and provides a tool which can be used to access these reprocessed results and apply them to a given model. The framework is intended as a fast and easy to use complementary approach to time consuming full-scale dedicated searches with optimized search strategies. The targeted user group are theorists outside the CMS collaboration with limited access to data, tools and information required to perform dedicated searches. The tool should therefore be usable standalone without links to CMS software and should not require knowledge of CMS data analysis procedures. It is also useful for CMS data analysts to gain first results in order to estimate how promising a full-scale analysis would be and if it is worth the effort.

9.2. Concept

Three tasks have to be solved in order to use the results of the MUSiC search to set constrains on specific signal models:

1. Define eligible test regions which provide good sensitivity for many different signals based on the classification output.
2. Provide a procedure to determine the expected contribution of any given signal in each of these regions.
3. Find the test region which yields the best sensitivity to the signal under investigation and calculate the exclusion limit.

1) Define eligible test regions

Since no assumptions are made on the properties a potential model should feature in order to be suited for the investigation (beside the general constrains of the MUSiC analysis[1]) various final states can be of interest. Therefore, every event class should be considered as a potential search channel in order to use the full potential of the analysis. Within each search channel the sensitivity can be enhanced by exploiting the kinematic properties of the signal under investigation instead of only using the overall event yield. Each of the three kinematic quantities considered by the MUSiC analysis ($\sum \mathrm{p_T}$, $\mathrm{M_{(T)}}$ or MET) can be used for this and each of them could yield the best result depending on the properties of the potential signal: If the signal predicts the resonant production of a new particle it is most likely that the distribution of the combined mass yields the best sensitivity while for many dark matter models the distribution of the missing transverse energy would most likely be the best choice. The shape of the signal distribution in combination with the shape of the background distribution determines which kinematic region will yield the best sensitivity: A compromise on the width of the region has to be found in order to include as much signal contribution as possible while not including too much background contribution. Since the shape of the distributions of the kinematic properties can vary greatly between different signals, regions with many different widths and starting at various thresholds should be considered as possible test regions. A sketch illustrating this concept can be found in Figure 9.1. In conclusion, various kinematic regions with different lower and upper thresholds in each kinematic distribution of all event classes should be considered as possible test regions in the METAL framework. The most inclusive approach is to consider every valid single bin and possible combination of adjacent bins as a potential test region as it is done for the MUSiC scan for deviations.

2) Determine expected signal contribution

In order to determine the expected signal contribution to the various test regions, a sample of simulated signal events has to be produced. This simulation needs to consider the detector response and the effects of the event and object reconstruction. This can either be done by running the full CMS detector simulation and reconstruction algorithms or by using the Delphes software framework [84] which uses a parametrization of the detector and reconstruction effects (details on Delphes will be given in Chapter 11). An emulation of the MUSiC classification algorithm is used to sort the signal events into the MUSiC event classes which then provide the expected signal contribution in every test region.

3) Find the region with the best sensitivity and determine the exclusion limit.

A brute force method is used to determine the test region with the best sensitivity for each signal under investigation: The expected exclusion limit on the total inclusive signal cross-section (σ_{excl}) is calculated for every test region that has a non-zero signal

---

[1] If a signal model does not predict any electron or muon within the acceptance of the used triggers, no sensitivity can be expected.

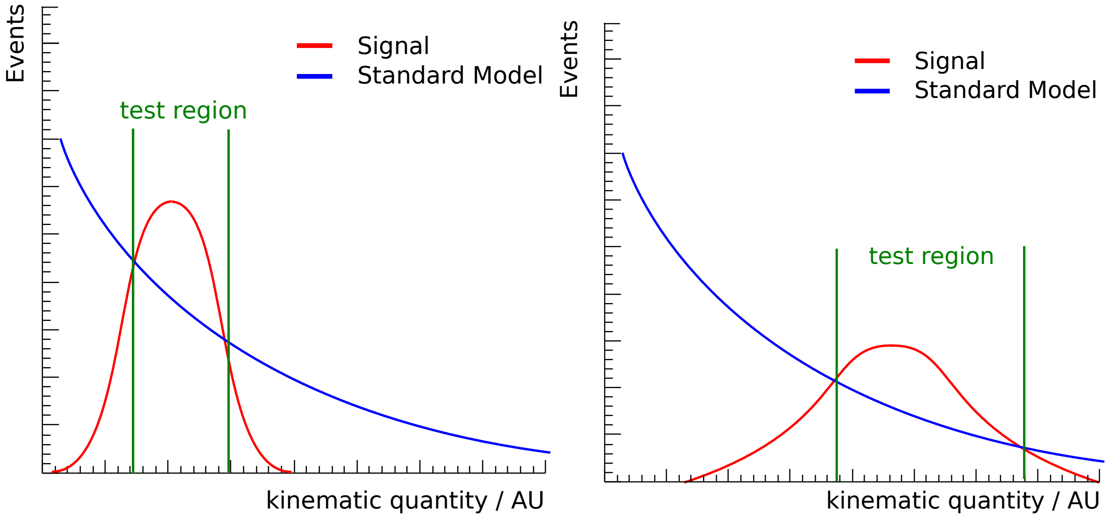

Figure 9.1.: Sketch of signals with different kinematic signature superimposed on an exemplary background distribution. The green lines indicate the test regions that would potentially yield the best sensitivity to the two signals. Since the set of eligible test regions should be prepared for all kinds of potential signals, regions with many different widths and starting at various thresholds should be considered.

contribution and the limit which yields the best expected limit is selected as the region with the best sensitivity. The region with the best expected limit is used and not the region with the best observed limit to prevent observation bias.

Since the calculation of exclusion limits takes a lot of time and a large number of limits has to be calculated in order to preform this brute force method it is not feasible to do this every time a specific signal is tested. Instead, model independent exclusion limits on the number of additional events above the Standard Model expectation are calculated for every eligible test region once in advance which are then reused every time a signal is tested. These limits are constructed as one sided confidence intervals on the number of additional events (as discussed in Chapter 4) starting always at zero and ending at an upper limit equal to the maximum number of additional events still consistent with the observed data at 95% CL in this test region ($\mathrm{n}_{\mathrm{excl}}$). For this limit calculation, each test region is considered as a single bin, characterized by three values: The overall data event yield ($\mathrm{n}_{\mathrm{obs}}$) in this region, the event yield expected from the Standard Model (n_{SM}) and the associated uncertainty ($\sigma_{\mathrm{n}_{\mathrm{SM}}}$)

When testing a specific signal model, these expected limits on the number of events have to be translated into the expected limit on the total inclusive signal cross section. This cross section limit depends on the acceptance ($\mathcal{A}$) of this bin region for the given signal model, the signal selection efficiency (ϵ) of the MUSiC classification and the integrated luminosity of the dataset (L). The product of acceptance and efficiency is defined as the fraction of signal events located in this test region relative to the total number of events in the signal sample: $\mathcal{A} \cdot \epsilon = \frac{\mathrm{N}_{\mathrm{signal}}(\text{bin region})}{\mathrm{N}_{\mathrm{signal}}(\text{total})}$ ($\mathrm{N}_{\mathrm{signal}}$(bin region) is determined as mentioned in task 2). Taking all this into account the excluded cross section can be calculated as

$$\sigma_{excl} = \frac{n_{excl}}{L \cdot \mathcal{A} \cdot \epsilon} \tag{9.1}$$

which in other words describes the total cross section needed for this model to contribute a number of $\mathrm{n_{excl}}$ events in the test region under investigation. The signal model is excluded if the observed cross section limit that is yielded from the region with the best sensitivity is larger than the cross section predicted by the model.

This method of translating model unspecific limits on additional event yield into limits for a particular model is called "recasting".

9.3. Structure of the software framework

The METAL framework is divided into two different programs: The first one is used to calculate the model independent exclusion limits on the number of additional events above the Standard Model expectation $\mathrm{n_{excl}}$ and the second one is used to perform the recasting of these limits into the model specific limits.

The calculation of $\mathrm{n_{excl}}$ for all eligible test regions has to be performed once by a member of the MUSiC analysis group for every data taking period of the LHC. The full MUSiC framework and the CMS computing infrastructure is needed in addition to the METAL framework to perform this task. The program is not intended to be used outside of the CMS collaboration and the results have to be provided to the end user in addition to the tool that performs the recasting of the limits. The methods to calculate $\mathrm{n_{excl}}$ are described in detail in Chapter 10.

The second program of the METAL framework contains the tool necessary to perform the recasting of the limits. This is intended to be used outside of the MUSiC working group and will be released standalone[2]. Within in this program, the Delphes simulation of the signal sample and the emulation of the MUSiC classification is performed and the results are used to calculate the signal acceptance and efficiency for all test regions. The program also runs the determination of the most sensitive region and provides the final exclusion limit together with various additional information as well as a plot of the kinematic distribution of the limit superimposed on the background distribution. All of this runs fully automated and the user only has to provide the theory input. Details on the implementation of the tool and a validation of its results performed on the classification results discussed in Chapter 8 will be given in Chapter 11. Instructions on how to get the tool and a short users manual can be found in the Appendix B.

9.4. Similar existing concepts

METAL is not the first software tool developed with the aim to provide a way to reuse existing results to constrain new theories and models. For example, there are

---

[2] As a first step, it will be made accessible for all members of the CMS collaboration but not for the general public, yet. This second step is planned to be done sometime in the future once the tool is approved by the collaboration.

CheckMATE [85], RECAST [86] and QUAERO [87, 88] which all use different approaches to accomplish this goal.

CheckMATE and RECAST use an approach in which the reinterpretation is done by calculating the signal efficiency for a new model for various existing dedicated analyses and using this information to translate the exclusion limit on the old model into limits on the new one. For both tools it is necessary to manually implement a representation of each dedicated analysis into the framework in order to make it accessible for the reinterpretation. The difference between the two is the way in which the analyses are implemented and the way the results are published. CheckMATE uses the software framework Delphes [84] to simulate the detector response for various high energy physics experiments and a standardized analysis implementation within the framework to further process those data while RECAST provides only an interface and the actual simulation of the signal and the implementation of the analysis is left to the original analyst.

QUAERO on the other hand is an automated tool which is much more comparable to METAL: Similar to the idea described in this thesis, QUAERO determines the region of phase space accessible to the analysis that gains the best sensitivity to a specific model and calculates the exclusion limit in this region based on the measured event yield and the Standard Model expectation as well as the signal efficiency in this region. There are two different version of QUAERO: The first one [87] is based on the SLEUTH analysis [45] performed at DØ similar to the way METAL is based on the MUSiC analysis and the second one [88] is based on the general search [49] performed at HERA.

10. Model Independent Exclusion Limits

The procedure used by METAL to calculate the exclusion limits on the number of additional events above the Standard Model expectation ($\mathrm{n_{excl}}$) will be presented in this chapter. The decision which methods to use and how to realize the actual implementation was determined by the various challenges that arise from the large amount of connected bin regions ($\mathrm{n_{region}} \sim 10^6$) and the large variation of the event yield and uncertainty between different regions: The expected number of events predicted by the Standard Model ($\mathrm{n_{SM}}$) can vary over many orders of magnitude from $\mathrm{n_{SM}} \sim 10^{-4}$ up to $\mathrm{n_{SM}} \sim 10^8$ and the uncertainty can vary from a few percent up to more than hundred percent. Therefore, the procedure needs to be fast, valid over a large range of input parameters and numerically stable. To achieve this, a simple approach is chosen for the limit calculation that only uses three input quantities: The number of observed events ($\mathrm{n_{obs}}$), the number of expected events ($\mathrm{n_{SM}}$) and the total uncertainty on the number of expected events ($\sigma_{\mathrm{n_{SM}}}$). A limit is calculated for every valid test region. Regions that consists of more than one bin of the initial kinematic distribution are nevertheless considered as one bin: The contributions of the initial bins are added up to get the overall number of observed and expected events for this test region. The overall systematic uncertainty on the number of expected events is obtained from the individual contributions as described in section 5.4.3. Automated cross-checks and validations are implemented in order to guarantee the validity of the limit result since they cannot all be checked manually.

10.1. General approach for limit calculation

Frequentist statistics is used in the METAL framework to calculate exclusion limits (see Chapter 4). Three different methods are utilized for the calculation in order to optimize the needed CPU time: The first one uses Monte Carlo techniques to determine the distributions of the test statistic of the hypothesis test (called “Monte Carlo limit calculation method”) while the second one describes the distributions approximately by asymptotic formulas (called “asymptotic limit calculation method”) which are only valid for sufficiently large values of $\mathrm{n_{SM}}$. The last one uses a simple approach which is only valid in regions where the uncertainty on the expected Standard Model event yield is dominated by the systematic uncertainty (called “simplified limit calculation method”). In this case the event yield itself is used as the test statistic with its distribution described by the same log-normal function used to model the systematic uncertainty. The last two methods are approximations which are much faster than the first one which is therefore only used in regions where the approximations are not valid. Details on the methods and their ranges of validity will be given in the following sections.

The choice of Frequentist statistics for METAL was mainly motivated by the fact that no methods exist which have a CPU time performance comparable to the two approximation methods that use a Bayesian approach. Besides that, a Bayesian approach would not gain any advantage over the Frequentist approach since it cannot utilize any prior knowledge on the signal model since no such model is assumed at the time of limit calculation. In the following sections, the three different limit calculation methods are discussed. A property of the limits called "coverage" is used in this discussion, which is therefore introduced beforehand. Finally, limit results for two example distributions are shown to visualize some features of the limit calculation methods.

10.2. Coverage of limits

10.2.1. Concept

The property of an exclusion limit called coverage describes if the confidence interval defined by the limit would contain the true value of the parameter of interest with a frequency equal to the stated confidence level when a large number of independent statistical tests (performed under identical conditions) are used to calculate the interval many times. If the parameter of interest is contained within the interval fewer times than claimed by the confidence level, the limit is labeled to have "undercoverage". The opposite case is denoted as "overcoverage". In the case of undercoverage the limit is considered to be too aggressive since a true signal hypothesis would be falsely rejected too often (the type I error rate (α) would be too high). Consequently, in the case of overcoverage, the limit is considered to be conservative since the type I error rate would be smaller than stated. Both cases should be avoided when calculating limits but undercoverage is the more problematic case since a false rejection is more likely than stated while overcoverage only reduces the sensitivity of the method. Coverage investigations will be used to check the validity of the different limit calculation methods in the following sections.

10.2.2. Implementation of the coverage test

The coverage of a limit calculation method is tested using a large set of pseudo data which are diced according to a signal plus background model with a given signal strength ($\mathrm{n}_{\mathrm{signal}}^{\mathrm{true}}$), Standard Model expectation (n_{SM}) and uncertainty $\sigma_{\mathrm{n}_{\mathrm{SM}}}$. The number of signal events ($\mathrm{n}_{\mathrm{signal}}$) is the parameter of interest in this case. For each diced pseudo data value an upper limit on the number of signal events is calculated ($\mathrm{n}_{\mathrm{signal}}^{\mathrm{excl}}$) and it is tested if the true value of the signal strength is included in the confidence interval ($\mathrm{n}_{\mathrm{signal}}^{\mathrm{excl}} > \mathrm{n}_{\mathrm{signal}}^{\mathrm{true}}$). The fraction of pseudo data dicing rounds that result in an exclusion limit smaller or equal to the true number of signal events relative to the overall number of dicing rounds is equal to the type I error rate

$$\alpha = \frac{n_{\mathrm{dice}}(n_{\mathrm{signal}}^{\mathrm{excl}} \leq n_{\mathrm{signal}}^{\mathrm{true}})}{n_{\mathrm{dice}}(\mathrm{total})}. \tag{10.1}$$

This simple approach to calculate the coverage of exclusion limits is very time consuming since a large amount of limits (~ 1000) has to be calculated for every parameter-point under investigation in order to get a reasonable precision. Taking into account the large range of possible input parameters ($\sim 10^{-4} \lesssim \mathrm{n_{SM}} \lesssim 10^{8}$ and $1\% \lesssim \sigma_{\mathrm{n_{SM}}} \lesssim 100\%$) that should be tested for coverage this approach is not feasible. Instead, a modification of the approach is realized that exploits the fact that the exclusion limit is monotonic dependent on the number of observed events as long as the other parameters are fixed:

1. Select value of $\mathrm{n_{SM}}$ and $\sigma_{\mathrm{n_{SM}}}$ that should be tested.
2. Choose a value $\mathrm{n_{observed}} = \mathrm{n^{start}_{pseudo\text{-}data}}$ and calculate a limit ($\mathrm{n_{excl}}$) for these three values.
3. Define the true value for the signal strength to be equal to that limit ($\mathrm{n^{true}_{signal}} = \mathrm{n_{excl}}$).
4. Dice many pseudo-data values for the number of observed events ($\mathrm{n_{pseudo\text{-}data}}$) according to the signal plus background model with the signal strength set to the true value calculated in the previous step.
5. If $\mathrm{n_{pseudo\text{-}data}} \leq \mathrm{n^{start}_{pseudo\text{-}data}}$: The limit corresponding to $\mathrm{n_{pseudo\text{-}data}}$ would be smaller than (or equal to) the true signal strength (due to the monotonic behavior) which means that the limit would be falsely rejected (typeI error): $\alpha = \frac{\mathrm{n_{dice}}(\mathrm{n_{pseudo\text{-}data}} \leq \mathrm{n^{start}_{pseudo\text{-}data}})}{\mathrm{n_{dice}}(\mathrm{total})}$

By using this approach, a limit has to be calculated only once per parameter point. The CPU time needed for the dicing of the pseudo-data can be neglected relative to the CPU time needed for the limit calculation.

10.3. Monte Carlo limit calculation method

This method uses the CLs technique (see Chapter 4) to perform the hypothesis test with the likelihood ratio

$$\frac{L(n_{signal} + n_{SM}^{exp}(\hat{\hat{\theta}}), \hat{\hat{\theta}})}{L(\hat{n}_{signal} + n_{SM}^{exp}(\hat{\theta}), \hat{\theta})} \tag{10.2}$$

as the test statistic for the hypothesis test and the number of signal events $\mathrm{n_{signal}}$ being the parameter of interest. The likelihood is constructed as the Poisson probability for the number of observed events depending on the number of SM events and the number of signal events. The true number of SM events is not known exactly and the expected SM event yield ($\mathrm{n^{exp}_{SM}}$) is modeled as the best estimator for the number of SM events $\mathrm{n_{SM}}$ multiplied with a log-normal distributed factor based on the relative systematic uncertainty on the background expectation ($\sigma_{\mathrm{n_{SM}}}$):

$$n_{SM}^{exp} = n_{SM} \cdot (1 + \sigma_{n_{SM}})^{\theta} \tag{10.3}$$

A log-normal distribution describes a random variable which logarithm follows a normal distribution. This means that the nuisance parameter θ, which enters the background description in the exponent, has to be normally distributed in order for the systematic uncertainty to be log normal distributed.

$\mathrm{L}(\mathrm{n}_{\mathrm{signal}} + \mathrm{n}_{\mathrm{SM}}(\hat{\hat{\theta}}), \hat{\hat{\theta}})$ is the profile likelihood function where the nuisance parameter θ was profiled out depending on the parameter of interest ($\mathrm{n}_{\mathrm{signal}}$). This means that conditional maximum likelihood estimators $\hat{\hat{\theta}}$ are determined that maximize the likelihood function for each entry of a chosen set of possible values for $\mathrm{n}_{\mathrm{signal}}$. The denominator is the unconditional maximum likelihood where both parameters $\mathrm{n}_{\mathrm{signal}}$ and θ have been used simultaneously to optimize the likelihood function. $\hat{\mathrm{n}}_{\mathrm{signal}}$ and $\hat{\theta}$ denote the maximum likelihood estimators for both parameters.

The hypothesis test is performed using a software framework developed by the Higgs analysis group of the CMS collaboration [89] which is based on the "RooStats" software libraries [90].

Since the hypothesis test can only consider values for $\mathrm{n}_{\mathrm{signal}}$ that are part of the set of values used in the profiling, it is important to construct this set in a reasonable way. The lower boundary ($\mathrm{n}^{\mathrm{min}}_{\mathrm{signal}}$) of the set is chosen to be zero which is motivated by the fact that one sided intervals are constructed. The upper boundary ($\mathrm{n}^{\mathrm{max}}_{\mathrm{signal}}$) is chosen to be at least three times larger than the resulting exclusion limit on $\mathrm{n}_{\mathrm{signal}}$ but smaller than five times the limit, following the recommendation from [89]. Since this can only be checked after the limit calculation, an iterative approach is chosen. In the first step, a simple estimation for the exclusion limit is used to determine a starting value for $\mathrm{n}^{\mathrm{max}}_{\mathrm{signal}}$:

$$\begin{aligned} n_{signal}^{max,\, start} &= 4 \cdot \sqrt{(\sigma_{n_{SM}} \cdot n_{SM})^2 + n_{SM} + (n_{SM} - n_{obs})^2} && \text{if } n_{SM} < n_{obs} \qquad (10.4) \\ n_{signal}^{max,\, start} &= 4 \cdot \sqrt{(\sigma_{n_{SM}} \cdot n_{SM})^2 + n_{SM}} && \text{else.} \end{aligned}$$

This starting value uses the combined systematical and statistical uncertainty on the number of expected Standard Model events as a crude estimator for the limit value. In case that there are more observed events than expected events in one region, an additional summand ($\mathrm{n}_{\mathrm{SM}} - \mathrm{n}_{\mathrm{obs}}$) is added quadratically which represents the diminution of the limit due to the excess of data events. The factor four in the equation as well as the square on the last summand was found empirically to yield a generally good approximation for most of the possible input values. An exception are very small event numbers for which the approximation yields a too small starting value. This is due to the fact that the CLs limit value approaches three events but the simple estimator approaches zero if n_{SM} approaches zero. To account for this, a lower boundary $\mathrm{n}^{\mathrm{max,\, start}}_{\mathrm{signal}} = 12$ is introduced which is equal to four times the lowest possible limit value.

With this starting value for the upper boundary of the set of possible values for $\mathrm{n}_{\mathrm{signal}}$, expected and observed limits are calculated. If $\mathrm{n}^{\mathrm{max,\, start}}_{\mathrm{signal}}$ is smaller than three times the expected or three times the observed limit, it is identified as being too small. If it is more than five times larger than the larger one of the two limits, it is identified as being too large. In both cases a new value is chosen for $\mathrm{n}^{\mathrm{max}}_{\mathrm{signal}}$: If the initial value was too large, it is halved and in the other case it is doubled. With this new value, new limits are calculated and the test is repeated. At each step the smallest value for $\mathrm{n}^{\mathrm{max}}_{\mathrm{signal}}$ which was still too large or the largest value which was still too small is saved (if one of the cases occur). If both values have been defined for the first time, the new value of $\mathrm{n}^{\mathrm{max}}_{\mathrm{signal}}$ is chosen to be exactly in the middle of the two values. This is repeated until a valid value for $n_{\text{signal}}^{\text{max}}$ is found. The expected and observed exclusion limits calculated with this upper boundary on the parameter of interest are used as the final result for the limit calculation.

10.4. Asymptotic limit calculation method

The same likelihood function as described in the previous section is used again to perform a hypothesis test following the CLs technique as described in the section before. Also, the same $n_{\text{signal}}^{\text{max}}$ optimization algorithm is used. The only difference between the asymptotic and the Monte Carlo limit calculation method is the method used to determine the probability density distributions of the test statistic: The asymptotic limit calculation method uses the approach described in [40] to determine an approximate analytical description of the probability density distributions while the previously described method uses Monte Carlo techniques to sample the distributions. The advantage of the analytical description of the distributions of the test statistic is that it speeds up the limit calculation by approximately a factor of 300 compared to the Monte Carlo approach. The asymptotic limit calculation method is implemented using the “RooStats” software libraries [90].

The problem with this approach is that the accuracy of the analytical approximation decreases for a decreasing number of expected Standard Model events n_{SM} and for very low numbers it yields wrong results. For this reason a study was performed to identify the region of the parameter space where the asymptotic limit calculation method yields valid results. For the first step of this study the coverage of the asymptotic limits is determined for small numbers of expected SM events and different uncertainties on this expected number. The signal strength for the coverage test is chosen to be equal to the observed limit corresponding to zero observed events and the value of the two other parameters at every parameter point. The results can be seen in the left plot of Figure 10.1 where the actual confidence level (one minus the type I error rate) of the limit divided by the claimed confidence level of 0.95 is plotted as a color map dependent on n_{SM} (x-axis) and $\sigma_{n_{\text{SM}}}$ (y-axis). The actual confidence level drops to 90% of the claimed one for n_{SM} approaching zero. The plot on the right of Figure 10.1 shows the same distribution for limits that have been calculated with the Monte Carlo limit calculation method as a comparison: No undercoverage is observed in this case. Both distributions show slight overcoverage for larger values of n_{SM} which is expected since the CLs technique was used for both limit calculations. No dependency of the coverage from the uncertainty $\sigma_{n_{\text{SM}}}$ is observed in both cases. The asymptotic limit calculation method reaches full coverage for numbers of expected Standard Model events of more than approximately 0.8. Below this value, the Monte Carlo limit calculation method must be used instead.

When combining the methods, it is important to ensure that the transition between the two is smooth. No step in the values of the exclusion limits dependent on the number of expected events must be introduced by the switching of the methods. This is checked with the plots in Figure 10.2 which shows the relative deviation between the expected limit calculated with the two methods dependent on the number of expected events and their relative uncertainty as a color map (left plot) and the direct comparison of the expected limit calculated with the two methods for a fixed relative uncertainty on

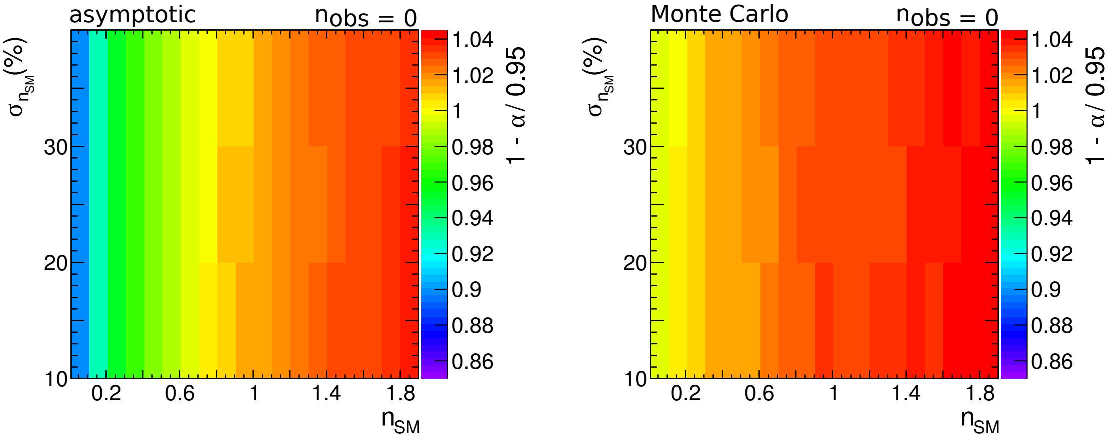

Figure 10.1.: Coverage of limits at small $\mathrm{n_{SM}}$. Both plots show the coverage properties $(\frac{1-\text{typeI error rate}(\alpha)}{\text{claimed confidence (0.95)}})$ as a color map depending on the expected number of Standard Model events ($\mathrm{n_{SM}}$) and their uncertainties ($\sigma_{\mathrm{n_{SM}}}$). The left plot contains the results for the asymptotic limit calculation method and the right one of the Monte Carlo method. For both plots, the signal strength for the coverage test is chosen to be equal to the observed limit corresponding to zero observed events and the value of the two other parameters ($\mathrm{n_{SM}}$ and $\sigma_{\mathrm{n_{SM}}}$) at every parameter point. The asymptotic method shows undercoverage for values $\mathrm{n_{SM}} \lesssim 0.8$ independent of their uncertainty.

the Standard Model expectation of 30% (right plot). Both plots are calculated for the case of zero observed events. The limit values converge against each other with rising $\mathrm{n_{SM}}$ and meet at approximately 0.8. Above that point the deviation between the two methods is statistically distributed and is caused by the limited numerical accuracy of the Monte Carlo method which is expected to be around 5% [89]. Next, the agreement of the observed limit is checked: Figure 10.3 shows the comparison of the observed limit calculated with the two methods for 30% uncertainty on the expected number of events and zero observed events (left plot) or one observed event (right plot). In both cases, the observed limit calculated with the asymptotic limit calculation method is larger than the one calculated with the Monte Carlo method. However, for the case of one observed event, the deviation is quite small and of similar size as the statistical accuracy of the Monte Carlo method and therefore acceptable. For the case of zero observed events the deviation is much larger but since the observed limit calculated with the Monte Carlo method is approximately constant at $\mathrm{n_{excl}} = 3$ independent of $\mathrm{n_{SM}}$, the results of the asymptotic method can be remedied by fixing them at this value for the case of zero observed events.

10.5. Simplified limit calculation method

When the absolute systematic uncertainty of the background becomes too large, a problem arises when applying one of the previously mentioned limit calculation method:

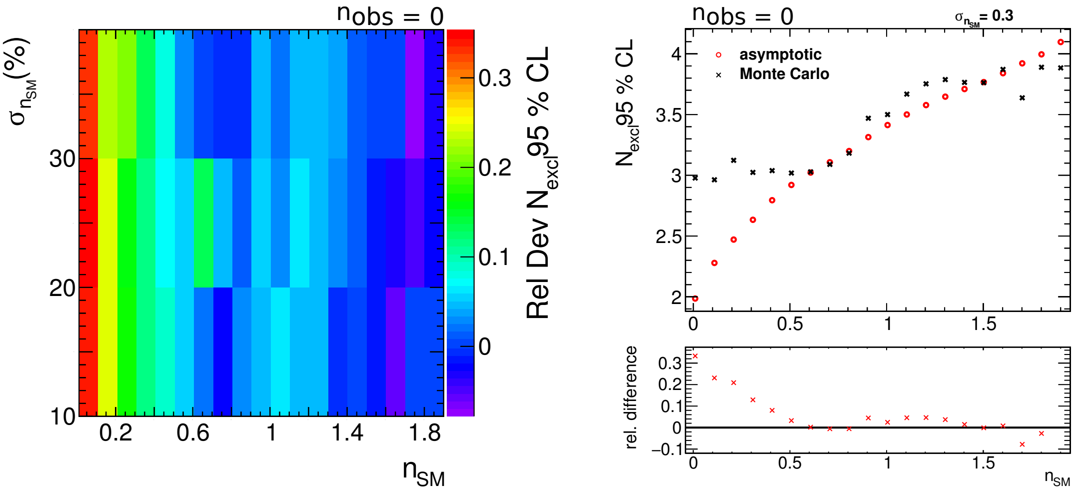

Figure 10.2.: This two plots show the comparison of the expected limit calculated with the asymptotic method and the Monte Carlo method. The left plot shows the relative difference between the two limits as a color map dependent on $\mathrm{n_{SM}}$ and $\sigma_{\mathrm{n_{SM}}}$ while the right plot show the direct comparison dependent on $\mathrm{n_{SM}}$ for a fixed uncertainty of $\sigma_{\mathrm{n_{SM}}} = 0.3$. A smooth transition can be observed between the two methods for rising $\mathrm{n_{SM}}$.

The determination of the maximum likelihood estimators for the test statistic becomes error-prone since a fit has to be performed with a very broad likelihood function which sometimes fails to converge. It was found that this is especially problematic in the determination of the profile likelihood at large values of the parameter of interest. This could partially be avoided by restricting the upper boundary of the interval of possible parameters of interest ($\mathrm{poi_{max}}$) to smaller values than five times the final limit value but it must not be smaller than three times the limit value in order to be valid. This leads to various parameter points for which the limit calculation fails with both of the previously mentioned methods. This is illustrated in the left plot of Figure 10.4 which shows the coverage for the asymptotic method for a signal strength equal to the observed limit obtained for $\mathrm{n_{SM}} = \mathrm{n_{obs}}$: The white areas indicate the regions in the parameter space where the limit calculation failed. This plot also shows that some undercoverage occurs for the asymptotic method at large uncertainties and large number of expected Standard Model events. Therefore, an additional, more simplified limit calculation approach was developed which can be used in these regions of the parameter space.

The idea for the simplified approach is that in the regions of large absolute systematic uncertainties the statistical distribution of the number of expected events can be neglected: The likelihood ratio as the test statistic is replaced by the event yield itself and its distribution is described solely by the log-normal distribution which is also used to model the systematic uncertainty in the likelihood function. An example for the distributions of the test statistic for the signal plus Standard Model and the Standard Model only hypotheses can be seen in Figure 10.5. The distribution for the signal + Standard Model hypothesis is obtained by shifting the distribution of the Standard Model only hypothesis

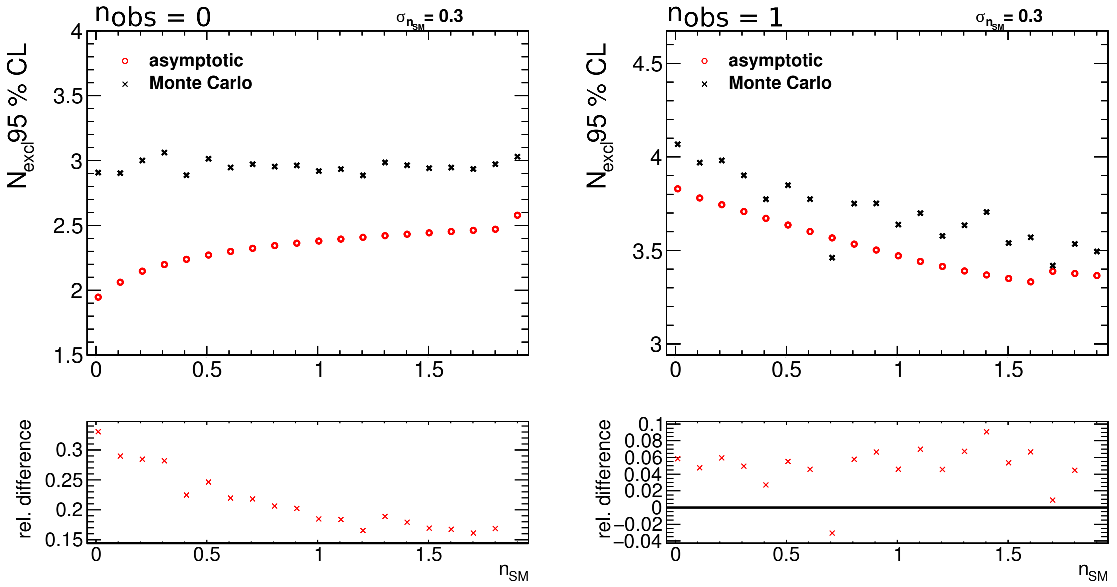

Figure 10.3.: The two plots show the direct comparison between the observed limit calculated with the asymptotic method and the Monte Carlo method. For the left plot the number of observed events is fixed at zero and for the right plot at one.

by the number of signal events n_{signal}. CLs can be calculated from these two distributions and the exclusion limit is equal to the number of signal events that corresponds to CLs $= 0.05$.

The right plot of Figure 10.4 shows the coverage of the limits calculated with the simplified method for a signal strength equal to the observed limit obtained for $n_{\mathrm{SM}} = n_{\mathrm{obs}}$. The behavior of the coverage depending on the two parameters is inverse to the one obtained from the asymptotic method. For increasing absolute uncertainties the coverage increases and reaches full coverage once $\sqrt{n_{\mathrm{SM}}}$ is approximately less than 15% of the systematic uncertainty. Strong undercoverage is observed for small absolute uncertainties (caused by small number of expected Standard Model events or small relative uncertainties) which is expected. The regions of the parameter space where the asymptotic method fails or shows undercoverage are all above the threshold where the simplified method reaches full coverage. Consequently, they can all be revised by switching from the asymptotic to the simplified method at that threshold. The left plot in Figure 10.6 shows the coverage of the combination of the two methods and the right plot shows the relative deviation between the coverage of the two methods in the transition region. The black line indicates the threshold $\sqrt{n_{\mathrm{SM}}} = 0.15 \cdot \sigma_{n_{\mathrm{SM}}} \cdot n_{\mathrm{SM}}$. Close to full coverage is achieved over the full parameter space and the transition between the two regions is accomplished without a noticeable offset.

By combining all three limit calculation methods, valid limits can be calculated for the full parameter space of foreseeable input values in the context of the MUSiC analysis in a time efficient manner. Table 10.1 summarizes which method is applied for which range

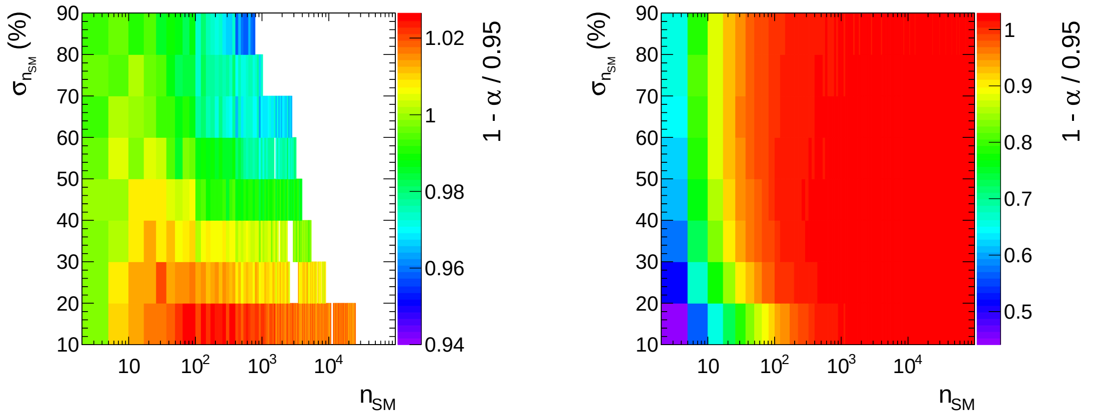

Figure 10.4.: Coverage of the asymptotic (left) and simplified (right) limit calculation method. The tested signal strength is equal to the observed limit obtained with $n_{SM} = n_{obs}$ and the corresponding uncertainty at each parameter point. The white areas in the left plot indicate parameter points where the limit calculation failed.

of n_{SM} and $\sigma_{n_{SM}}$.

Method	Range of application
Monte Carlo method	$n_{SM} < 0.8$
Asymptotic method	$n_{SM} \geq 0.8$ and $\sqrt{n_{SM}} > 0.15 \cdot \sigma_{n_{SM}} \cdot n_{SM}$
Simplified method	$\sqrt{n_{SM}} \leq 0.15 \cdot \sigma_{n_{SM}} \cdot n_{SM}$

Table 10.1.: Range of application for the three different limit calculation method used in this thesis. The ranges where optimized to gain the best overall computation time while still producing valid limits for each parameter point.

10.6. Preselection of bin regions for limit calculation

Despite the elaborated effort which was spent to optimize the CPU time of the limit calculation, the runtime is still too large to calculate limits for all of the $2.78 \cdot 10^6$ valid bin regions constructed by the MUSiC classification which makes it necessary to reduce the number of regions for the limit calculation. The general idea chosen for this reduction is to skip regions that cover kinematic ranges which are already covered by a large fraction by a region which is already accepted for limit calculation. To catch the motivation for this, it is necessary to recall the initial motivation for having many different regions in the first place: The model independent limits are intended to be applied on any possible theory and many different bins are needed to find the region which is sensitive to the signal. If a region is skipped which would provide the best sensitivity on a specific model

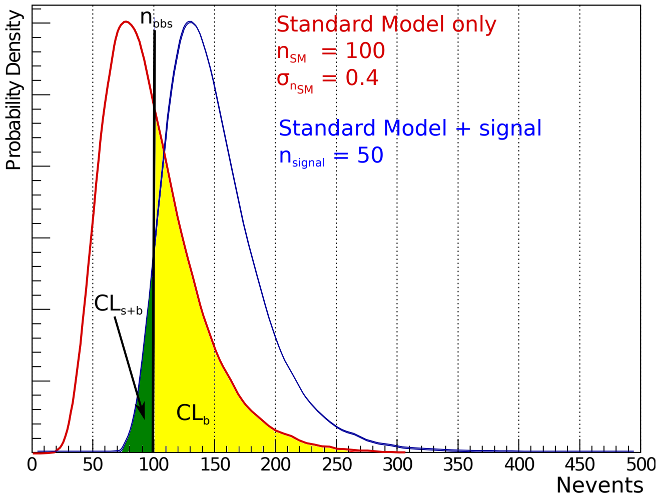

Figure 10.5.: Example for the test statistic distributions of the simple limit calculation method. The number of events is used directly as the test statistic quantity. The red distributions corresponds to the Standard Model only hypothesis and the blue one to the Standard Model plus signal hypothesis. Both are described analytically by a log-normal distribution with the width given by the systematic uncertainty on the number of events expected by the Standard Model. The signal plus Standard Model distribution is equal to the Standard Model only distribution with the exception of a global shift given by the number of expected signal events. CLb, CLs+b and CLs are calculated from these distributions in the usual manner.

(e.g. it would cover most of the signal contribution) but there is another region which covers almost the same kinematic range, the loss of sensitivity would be small.

The reduction of regions is realized by the following approach: Every valid bin of every distribution is used as a starting point for a region but not every following bin is used as an endpoint for an associated region. The skipping of endpoint bins should be done in a way that results in many small regions and fewer large regions. The motivation for this is obvious: Adding a single bin to an already large region does not change much while adding a single bin to a small region can have a large impact.

It was chosen that the region size should be growing exponentially with the base 1.5 with the number of bins included in the region being the measure for the size of the region. This is realized by only keeping regions in which the number of bins between the start bin and the endpoint bin is equal to a number “n” matching the equation $n = \lfloor 1.5^{i} \rfloor$ with $i \in \mathbb{N}$. The region with the endpoint bin equal to the last valid bin of the distribution is always kept. Furthermore, the minimum region width is set to contain at least 3 bins to further reduces the number of regions without loosing much efficiency to most signals since very narrow resonances are rare. A visualization of this concept can be seen in Figure 10.7.

Additional to this, all bin regions are rejected in which the difference between the

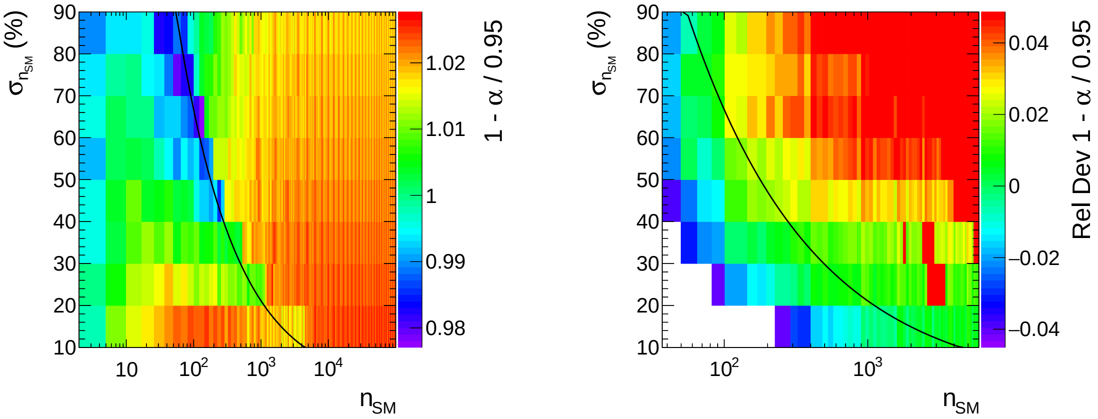

Figure 10.6.: Coverage of the combination the asymptotic and simplified limit calculation method. The left plot shows the coverage over the full parameter space when combining the asymptotic and the simplified method with the transition taking place at $\sqrt{n_{SM}} = 0.15 \cdot \sigma_{n_{SM}} \cdot n_{SM}$ (black line). Close to full coverage is achieved over the full range. The right plot shows the relative deviation between the coverage of the two methods for the transition region and indicates a smooth transition.

Standard Model expectation and the observed data is larger than two times the quadratically combined statistical and systematical uncertainty on the background expectation ($\sigma^{abs}_{combined} = \sqrt{n_{SM} + (\sigma_{n_{SM}} \cdot n_{SM})^2}$). This is done since the automatic limit calculation becomes somewhat prone to failure when the deviation between Standard Model expectation and observation becomes too large. In addition to this, these regions are much more interesting concerning a possible discovery than an exclusion and are therefore treated in the analysis described in [1] which has its focus on the search for those potential discoveries.

10.7. Exclusion limits for example distributions

In the following, the results of the exclusion limit calculation for two example distributions are shown. The first one is the $\sum p_T$ distribution of the `1e incl.` event class which is chosen as an example of a distribution with many valid bin regions, a very high event yield and many different contributing SM processes. The second one is the mass distribution of the `2e` 2μ `jetincl.` event class which is chosen as an example for an event class with a low event yield that is dominated by one process(Multi-Boson production). The results for the first example are shown in Figure 10.9 and the results for the second one in Figure 10.11. The first plot in both figures shows the kinematic distribution used as input for the limit calculation and the two plots in the second row of the figures show the expected limit (left) and the observed limit (right) on the number of additional events above the SM expectation for all regions passing the region preselection discussed in the

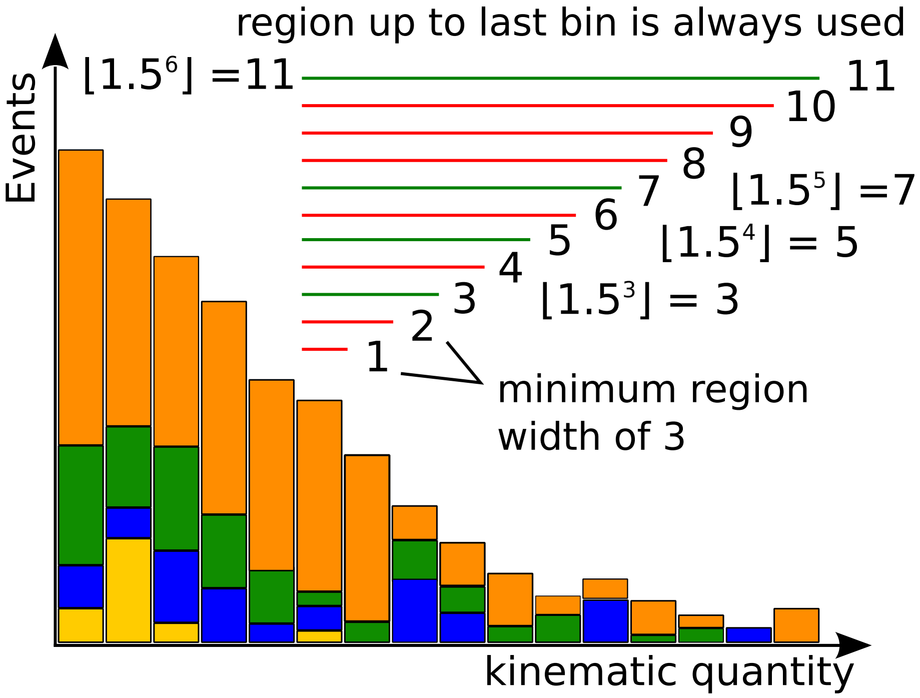

Figure 10.7.: Sketch of the limit region preselection algorithm: An example is shown for one start bin. The green lines indicate regions that are kept and the red lines regions that are rejected. For each accepted region, the matched requirement is stated. The first two regions are rejected because they are smaller than the minimal region width. In this example, the last region (which is always kept) does additionally fulfill the requirement of the exponential growth. This algorithm is repeated with each bin being used as a start bin.

previous section. The x-Axis indicates the lower boundary of the region and the y-Axis indicates the upper boundary. The color code shows the excluded number of events and a white region indicates that no limit has been calculated. The reason that no limit has been calculated is either an insufficient number of simulated Standard Model events (see section 5.4.2), the deviation between Standard Model expectation and observed data is too large (see previous section), or the region was rejected to reduce the overall number of regions (see previous section). The limit values in the first example vary from the minimum of three events calculated for regions in the high momentum tail of the distribution up to more than a million events for regions beginning at low momentum. The range of different limit values in the second example is much smaller and ranges from three events up to approximately ten events.

Analogous calculations have been performed for every distribution and every event class and are stored for further usage by the reinterpretation tool which will be presented in the next chapter.

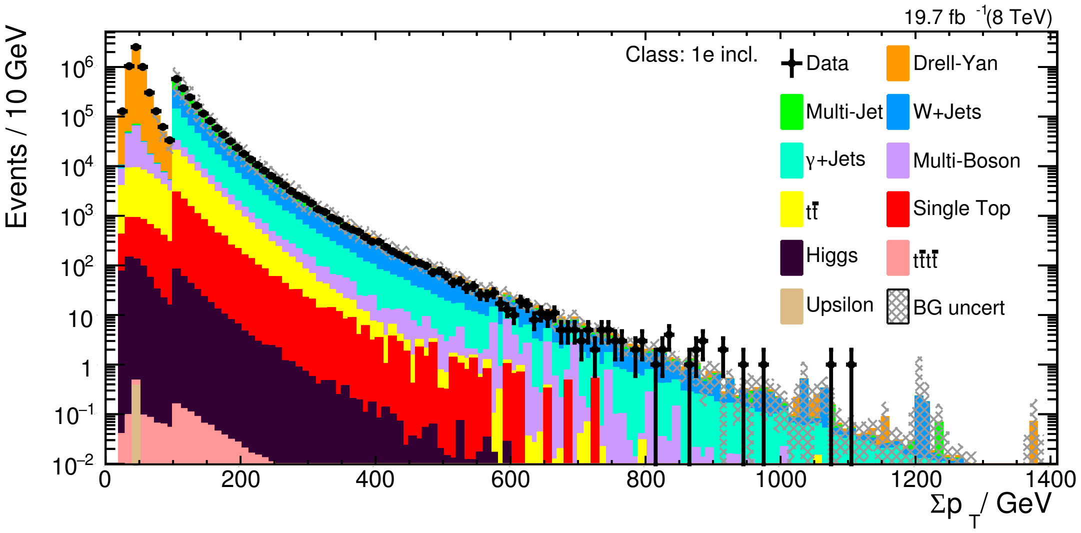

Figure 10.8.: $\sum p_T$ distribution of the `1e incl.` event class. The observed event yield and the Standard Model expectation visualized in this plot is used to calculate the exclusion limits of the example shown in Figure 10.9.

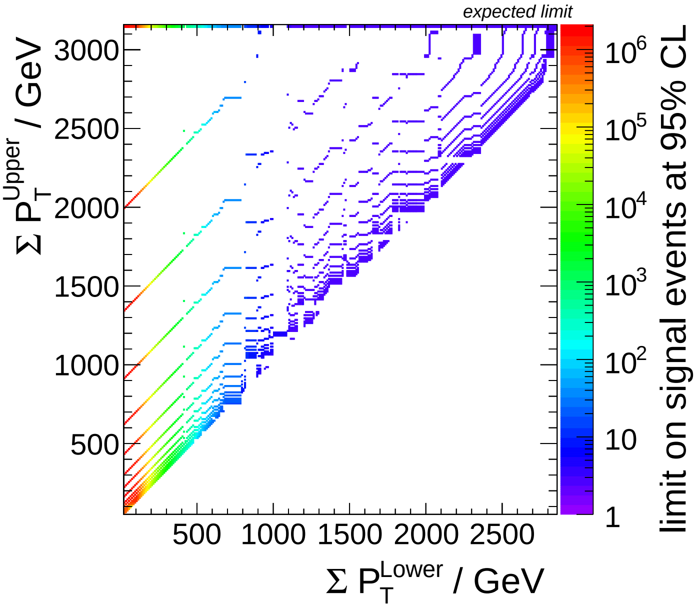

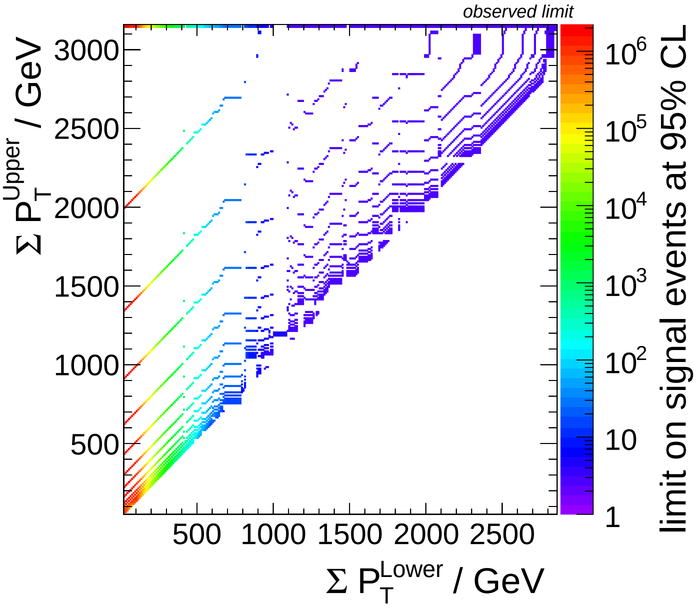

Figure 10.9.: Exclusion limit example for the $\sum p_T$ distribution of the `1e incl.` event class which is shown in Figure 10.8: The upper plot shows the expected limit and the lower plot shows the observed limit with the number of excluded events shown by the color coding. The x-Axis indicates the lower boundary of the region and the y-Axis indicates the upper boundary. Regions that have been skipped in the calculation are shown in white.

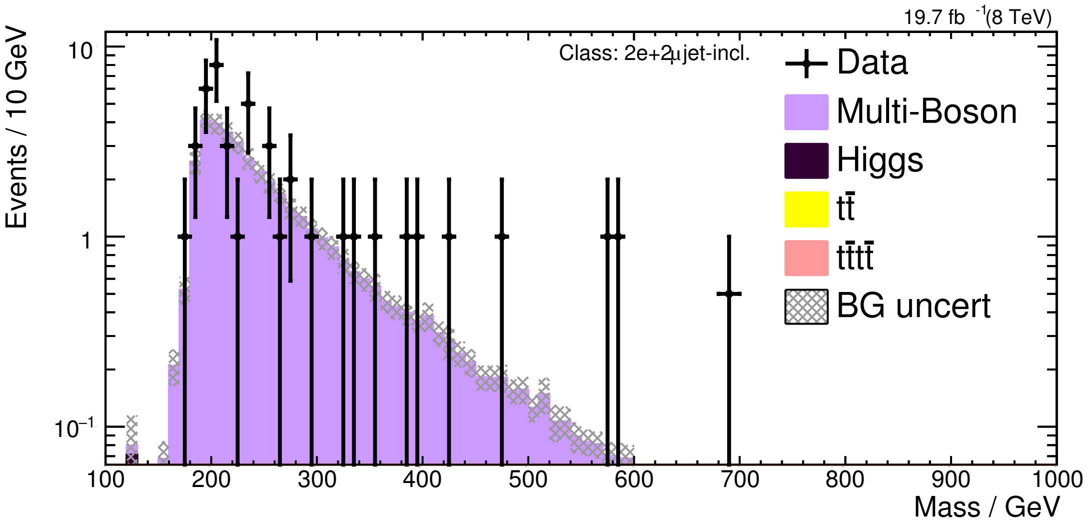

Figure 10.10.: Mass distribution of the `2e` 2μ `jetincl.` event class. The observed event yield and the Standard Model expectation visualized in this plot is used to calculate the exclusion limits of the example shown in Figure 10.11.

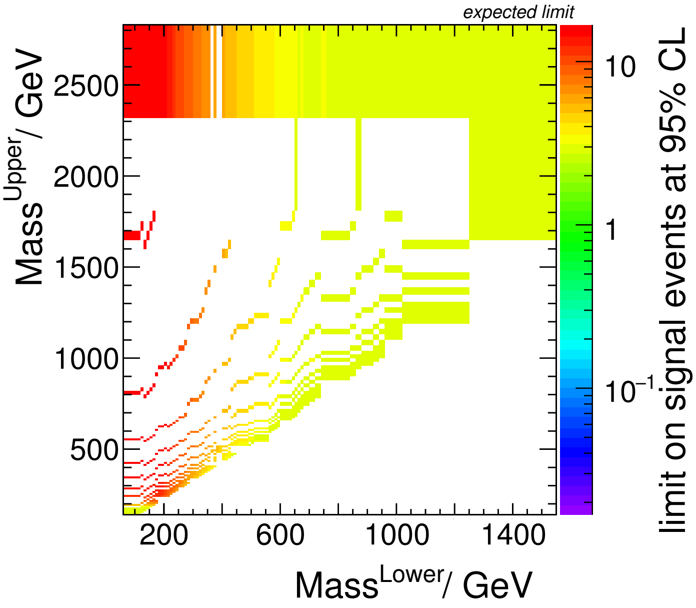

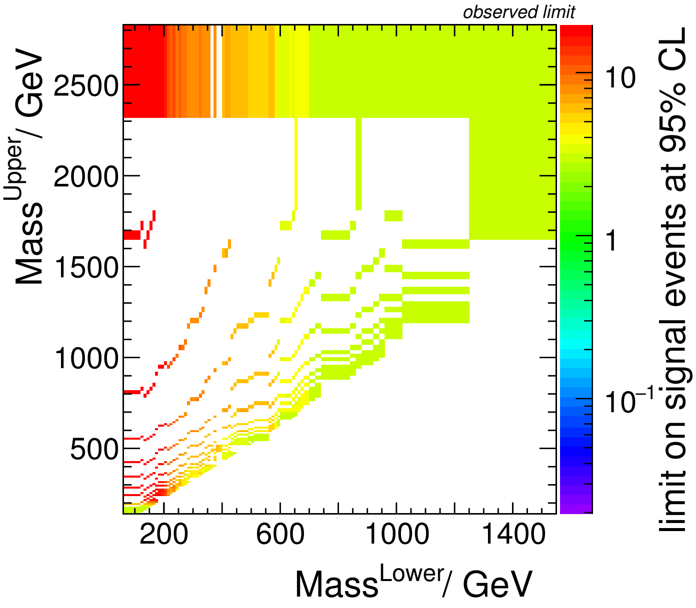

Figure 10.11.: Exclusion limit example for the mass distribution of the `2e` 2μ `jetincl.` event class which is shown in Figure 10.10: The upper plot shows the expected limit and the lower plot shows the observed limit with the number of excluded events shown by the color coding. The x-Axis indicates the lower boundary of the region and the y-Axis indicates the upper boundary. Regions that have been skipped in the calculation are shown in white.

11. Recasting the Limits

The final step of the METAL workflow is the recasting of the model independent limits for specific signal models in order to test if they are consistent with the data or if they are excluded. As mentioned in Chapter 9, this should be done by a standalone software framework that only uses publicly accessible software so that it could be used outside of the CMS collaboration. The basic idea of the recasting is to translate the limits on the number of additional events above the Standard Model expectation into limits on the signal cross section of the model under investigation. This is done by applying equation 9.1 to every bin-region for which the signal contribution is non-zero. To make this possible, the efficiency of the MUSiC selection for this signal model as well as the acceptance of each bin-region has to be determined. The main challenge for this is the simulation of the CMS detector response for signal events without using software restricted to CMS members. It was decided to use the Delphes software framework[84] for this task. Delphes uses parameterizations of the detector response and reconstruction algorithms to various physics objects in order to emulate the CMS event reconstruction. Since the Delphes developers could not access the full CMS detector information for their parameterization, the results can be improved by performing an optimization that takes into account results from the full CMS detector simulation. This optimization as well as the validation of the results and a presentation of the recast workflow will be given in the following chapter. The standalone software framework which performs the recast workflow is called “METAL-Forge”.

11.1. The recast procedure

In this section, the full workflow starting from the signal input and resulting in a statement on the signal model is discussed. This is done qualitatively in order to illustrate the general concepts. Validation results as well as limit results on three example theories will be given in the following sections.

11.1.1. Signal model input

There are three different data formats which can be used to enter signal models in the recast tool: LHEF [91], HepMC [92] and MUSiC classification results. The first two are standard event description formats commonly used in the high energy physics community while the latter one is the event format used by the MUSiC analysis group. The signal model data file should contain at least 10^4 simulated events in order to produce reliable results. If the final result shows that the overall sensitivity of the MUSiC analysis is very low for the model under investigation, it is advised to increase the number of simulated events in order to provide a reasonably smooth description of the signal spectrum in the distribution that yields the best expected limit.

The MUSiC classification result event format is produced by the full MUSiC software (using full CMS detector simulation and event reconstruction) and is not intended to be used by the end-user of the recast tool but by the METAL developers. Its purpose is to validate the results obtained with the first two input formats which use the Delphes simulation during development.

The HepMC data format contains the full collision event information prior to the simulation of the detector response for each simulated event. The full hadronisation of quarks and gluons, the decay of instable particles and the adding of additional jets from initial or final state radiation is already included in this data. A signal model that is fed into METAL-Forge in the HepMC format is directly processed by Delphes which produces output that corresponds to the reconstruction level information of the standard CMS workflow.

The LHEF ("Les Houches Event File") data format only contains information on the properties of the primary interaction. It is therefore necessary to preprocess input files in the LHEF format with the Pythia8 software package before the detector response can be emulated with Delphes. Pythia8 simulates hadronisation, particle decays and inital and final state radiation and produces intermediate output with the same information content as provided by HepMC.

11.1.2. Translation of model independent into model specific limits

The first step of translating the model independent into model dependent limits is the calculation of the efficiency(ϵ) of the MUSiC analysis for the signal model and the acceptance($\mathcal{A}$) of every bin region for which a model independent limit was calculated. This is done in one combined step within in the "METAl-Forge" by passing the Delphes output of the LHEF and HepMC input files into an emulation of the MUSiC event classification. The same kinematic and geometrical selections are performed and the same types of event classes and kinematic distributions are formed as is done by the MUSiC classification. The combined acceptance and efficiency (called "total signal efficiency" in the following) for each bin is then determined by dividing the number of signal events in every bin region by the overall number of signal events provided by the initial input file. The emulation of the MUSiC classification is of course skipped if the signal input is already provided in the format of MUSiC classification results.

After that, the expected and observed limit on the number of additional events above the Standard Model expectation for every bin region of every distributions is combined with the associated total signal efficiency and the luminosity according to equation 9.1. After this, a set of model specific limits on the signal cross section is available for every kinematic distribution and event class (with a non zero signal contribution) with every limit being mapped to a lower and a upper bin region threshold.

11.1.3. Best expected limit and final result

In the last step the region with the best expected limit is selected to perform the final test on the theory. Firstly, the region with the best expected limit is determined for every kinematic distribution and after that the kinematic distribution with the region that yields the overall best expected limit. A plot is produced for this kinematic distribution (for example see Figure 11.12 / 11.13 / 11.14) which shows the signal under investigation superimposed on the measured data and the background expectation. The two green dashed lines indicate the bin region which yields the best expected limit. Finally, the observed limit obtained from this region is stated together with the expected limit. If the model cross section is larger than the observed limit, the model is excluded with (at least) 95% CL.

The overall runtime of the METAL-Forge for a signal model depends on the overall number of events simulated for the model and the input format. LHEF files need more computation time than HepMC files since Pythia8 has to be executed in a separate step. However, the typical runtime for a sample with an overall number of simulated events in the order of 10^4 should only be a few minutes on a normal laptop even for a LHEF input file.

11.2. Delphes optimization

The Delphes software framework uses datacards that provide the parameters needed to emulate the detector simulation and the effects of the event reconstruction. Although a datacard is provided by the Delphes collaboration for the CMS detector, some additional improvements are needed since the members of the Delphes collaboration do not have access to the full knowledge about the CMS detector. In a first step, additional information taken from [93] is merged into the official datacard. Despite that, the description of the muon momentum smearing as well as the photon energy smearing had been found to be poor while the description of the electron energy smearing seems to be alright. For the investigation of the photon kinematic properties, the variance of the reconstructed energy relative to the generated energy is used. The reconstructed energy is expected to be distributed normally since it is measured directly from the light yield in the calorimeter. For the investigation of the muon kinematic properties, the distribution of the inverse transverse momentum is used instead since it reflects the underlying effect of momentum measurement responsible for the spreading of the measured momentum relative to the true value: The momentum is determined by measuring the bending of the particle's track. The uncertainty of the track bending can be assumed to be normally distributed since it is caused directly by the uncertainty of the measurement of the hits in the tracker and the muon system. Since the momentum is inversely proportional to the bending of the track, the inverse transverse momentum uncertainty is expected to be normal distributed and not the momentum uncertainty itself. Figure 11.1 shows the comparison of the simulation of kinematic properties for muons and photons done with the standard Delphes simulation and the full CMS software ("Full Sim"). While the muon distribution shows reasonable agreement at low momenta but deviates at higher ones, the variance of the photon energy reconstruction is nearly constantly off by approximately one order of magnitude over the full energy range.

For the photon investigation, Standard Model single photon samples[1] are used while the muon investigation is performed on the Zprime example model for a Z' boson with a mass of 1500 GeV which will be discussed in the next section.

In addition to a potentially wrong parametrization of the muon momentum reconstruction, one additional problem of the standard Delphes simulation is that it does not describe the distribution of the inverse transverse muon momentum with a normal distribution but the distribution of the transverse momentum itself.

The description of the reconstruction efficiencies for electrons, muons and photons taken from the default Delphes datacard seems to be correct. The validity of the efficiency description and the electron energy smearing will be shown in the next section. It was decided to use these efficiency parameterizations for all objects and the default description of the electron energy smearing but determine the photon energy and muon momentum smearing ourselves. This is done with Monte Carlo samples by investigating the difference between the kinematic properties of the objects before the full detector simulation (generator level) and after the full reconstruction is performed (reconstruction level).

The full Delphes parameter card used in this thesis can be found in the Appendix D.

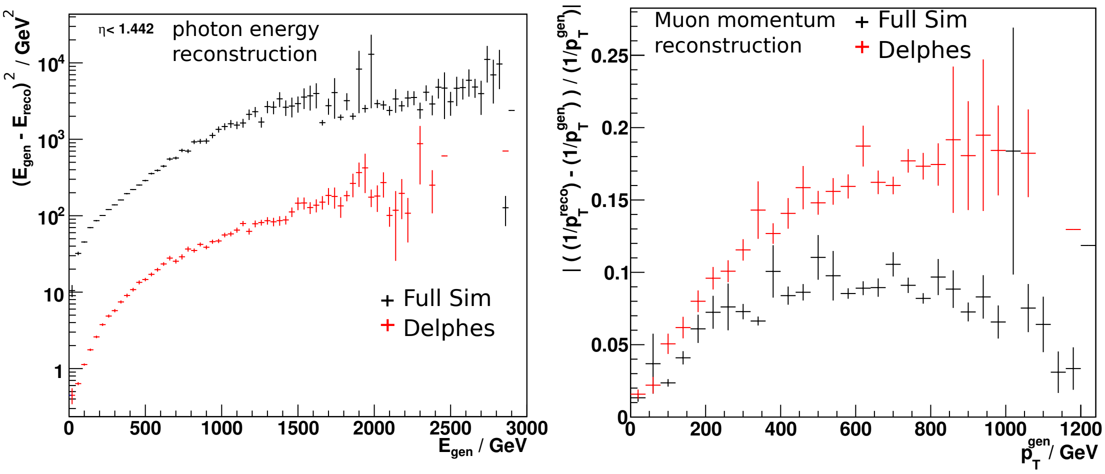

Figure 11.1.: Comparison of simulation of kinematic properties done by standard Delphes compared to Full Sim. Left: Mean value of the quadratic difference between generated and reconstructed photon energy. The standard Delphes results are too low by approximately one order of magnitude. Right: Mean value of the relative inverse muon transverse momentum smearing. The difference between standard Delphes and Full Sim is between 50% and 100%.

---

[1] GJets_HT(40,100,200,400)To(100,200,400,Inf)_8TeV-madgraph/Summer12_DR53XPU_S10_START53_V19v1AODSIM

11.2.1. Muon momentum smearing

The muon momentum smearing in the Delphes simulation must be optimized to better match the one that results from the muon reconstruction used in the MUSiC analysis (see section 7.2). The first step for this is to change the method of smearing the transverse momentum with a normal distribution to smearing the inverse of the transverse momentum instead. This is obtained from [94] where it was initially investigated and implemented. However, the parameterization of the inverse momentum smearing used in this work cannot be used since it was determined in the context of an upgrade study for a proposed future version of the CMS detector. Instead, the parameterization is determined for the current state of the detector by myself. Since muons are of particular interest in the context of the MUSiC analysis, it was decided to determine the parameterization separately for three different bins of the pseudo-rapidity ($|\eta| < 0.5$, $0.5 < |\eta| < 1.442$ and $1.442 < |\eta|$).

Figure 11.2 shows the results of polynomial fits to the different distributions in the first bin of η and Table 11.1 summarizes the parameterization resulting from all fits. The fits to the distributions in the other two bins can be found in the Appendix C.1. In the last $\mathrm{p_T}$ bin of each pseudo-rapidity region where the sample size of the Full Sim samples is too low to get meaningful results, the last value of the adjacent lower $\mathrm{p_T}$ region before is used as a constant in order to get an approximative description.

		$\lvert(\frac{1}{\mathrm{p_T^{reco}}} - \frac{1}{\mathrm{p_T^{gen}}})/\frac{1}{\mathrm{p_T^{gen}}}\rvert$
$\lvert\eta\rvert < 0.5$	$20\ \mathrm{GeV} < \mathrm{p_T^{gen}} < 1000\ \mathrm{GeV}$	$1.337 \cdot 10^{-10} \cdot (\mathrm{p_T/GeV})^3$
		$-2.773 \cdot 10^{-7} \cdot (\mathrm{p_T/GeV})^2$
		$+0.24 \cdot 10^{-3} \cdot (\mathrm{p_T/GeV}) + 0.01003$
	$1000\ \mathrm{GeV} < \mathrm{p_T^{gen}} < 2000\ \mathrm{GeV}$	$4.461 \cdot 10^{-5} \cdot (\mathrm{p_T/GeV}) + 0.0649$
	$2000\ \mathrm{GeV} < \mathrm{p_T^{gen}}\ \mathrm{GeV}$	0.154
$0.5 < \lvert\eta\rvert < 1.442$	$20\mathrm{GeV} < \mathrm{p_T^{gen}} < 1500\ \mathrm{GeV}$	$3.61 \cdot 10^{-11} \cdot (\mathrm{p_T/GeV})^3$
		$-1.314 \cdot 10^{-7} \cdot (\mathrm{p_T/GeV})^2 +$
		$0.19 \cdot 10^{-3} \cdot (\mathrm{p_T/GeV}) + 0.01362$
	$1500\ \mathrm{GeV} < \mathrm{p_T^{gen}}\ \mathrm{GeV}$	0.129
$1.442 < \lvert\eta\rvert$	$20\ \mathrm{GeV} < \mathrm{p_T^{gen}} < 800\ \mathrm{GeV}$	$7.42 \cdot 10^{-11} \cdot (\mathrm{p_T/GeV})^3$
		$-2.400 \cdot 10^{-7} \cdot (\mathrm{p_T/GeV})^2$
		$+0.32 \cdot 10^{-3} \cdot (\mathrm{p_T/GeV}) + 0.01012$
	$800\ \mathrm{GeV} < \mathrm{p_T^{gen}}\ \mathrm{GeV}$	0.150

Table 11.1.: Parametrization of the inverse muon transverse momentum smearing depending on the generated transverse momentum of the muon. The constant value in the last $\mathrm{p_T}$ bin of each pseudo-rapidity region is an approximation determined as the last value of the adjacent lower $\mathrm{p_T}$ region before.

11.2.2. Photon energy smearing

The parameterization of the photon energy smearing is determined by using the Full Sim energy variance distribution that is also used in Figure 11.1 (left) as the reference

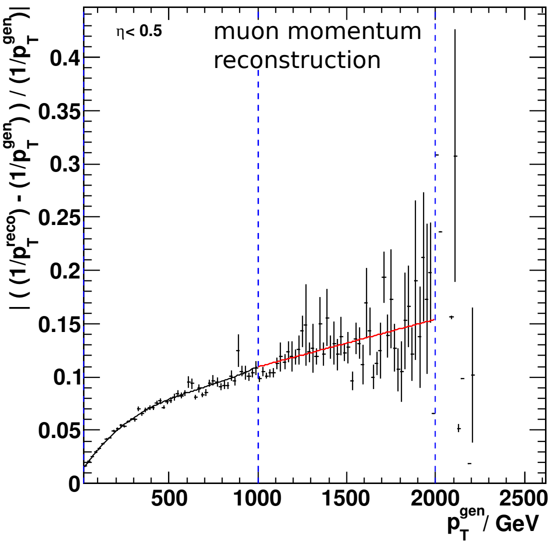

Figure 11.2.: Determination of the parameterization of the inverse muon transverse momentum smearing in the pseudo-rapidity bin of $|\eta| < 0.5$.

curve. Again, polynomial functions are fitted to the distribution in order to describe the variance as a function of the generated photon energy. The plot showing the results of the polynomial fits can be found in Figure 11.3. The resulting parameterizations can be found in Table 11.2.

		$(E_{gen} - E_{reco})^2$
$|\eta| < 1.442$	$E_{gen} < 60$ GeV	$(0.3125 \cdot (E_{gen}/\text{GeV}) + 4.25)$ GeV^2
	60 GeV $< E_{gen} <$ 400 GeV	$(4.69 \cdot 10^{-6} \cdot (E_{gen}/\text{GeV})^3 -$ $0.0029 \cdot (E_{gen}/\text{GeV})^2$ $+1.0088 \cdot (E_{gen}/\text{GeV}) - 28.735)$ GeV^2
	400 GeV $< E_{gen} <$ 1000 GeV	$(0.00211 \cdot (E_{gen}/\text{GeV})^2$ $-1.069 \cdot (E_{gen}/\text{GeV}) + 303.04)$ GeV^2
	1000 GeV $< E_{gen} <$ 1600 GeV	$(3.868 \cdot (E_{gen}/\text{GeV}) - 2586.41)$ GeV^2
	1600 GeV $< E_{gen}$	60.017 GeV^2

Table 11.2.: Parametrization of the photon energy smearing depending on the generated energy of the photon. There is only one bin in η since only photons in the barrel are considered in the analysis. The constant value in the last energy bin is an approximation determined as the last function-value of the energy region before.

11.3. Limits on example models

In the following section, a validation of the limit reinterpretation will be presented. For this purpose results for three example models are calculated once with the METAL-Forge

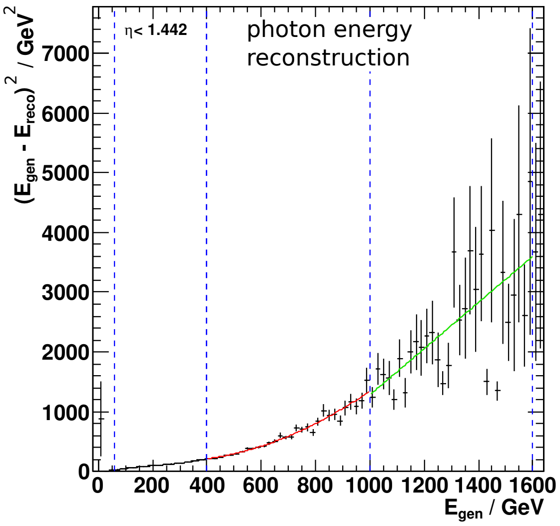

Figure 11.3.: Determination of the parameterization of the photon energy smearing in the pseudo-rapidity bins of $|\eta| < 1.442$.

reinterpretation tool and again using the full CMS simulation software. The final limit results as well as some characteristic kinematic distributions yielded from both approaches are compared to each other. Finally, the cross section limits are compared to the results of dedicated analyses.

11.3.1. Introduction to the example models

The first two signal models that are used in this thesis to validate the reinterpretation tool all postulate new vector bosons as an addition to the ones known from the Standard Model. They have been selected as examples since models that predict new vector bosons are of particular interest at the LHC as they can tackle many questions unanswered by the Standard Model and produce clear signatures in phase-space regions that are accessible for the first time by the LHC.

The first model describes the production and decay of a heavy copy of the Standard Model W-Boson called “Sequential Standard Model W'”(SSM W') [95] and the second one describes an additional resonance in the dilepton mass spectrum called Z'_{ψ} [96].

The third model postulates a new type of particle called “leptoquark” which is a particle that carries both lepton and baryon number. This model was chosen since it includes jets as part of the decay signature which is not the case for the first two models.

A short introduction for the three theories will be given in the following. This is not intended as a complete discussion of the theories but rather to provide a framework for the understanding of the following validation. For detailed information, refer to the previously cited literature.

Sequential Standard Model W′

The SSM W′ model was developed to provide a benchmark signature for searches targeting W-like signals at high masses. The W' in this model is constructed as a carbon copy of the Standard Model W with the same couplings and the mass as a free parameter. The mass is restricted to values large enough to enable the decay into pairs of one top quark and one bottom quark. The decay into WZ is assumed to be non-existent. For the purpose of the validation described in this chapter it was chosen to investigate the decay of the W' into an electron and an electron-neutrino. The branching ratio for this decay is $\mathrm{BR}(\mathrm{W}' \rightarrow \mathrm{e}\,\nu) \approx 8\%$ and the cross section for various mass parameters can be found in Table 11.3. Signal samples for the decay of the W' into an electron and an electron-neutrino have been produced at leading-order cross section with the PYTHIA6 [68] event generator and using the CTEQ6L1 [97] pdf set. K-factors have been calculated to scale the cross section to next-to-next-to-leading-order QCD [83]. The full CMS detector simulation[2] was performed for these samples in order to validate the results obtained with the Delphes simulation for the same processes. The Delphes simulation uses HepMC input data produced from the same events previously generated with PYTHIA6. The sample production was performed by the analysis group of [83].

$m_{\mathrm{W}'}$ (GeV)	σ_{LO} (pb)	k-factor LO → NNLO	σ_{NNLO} (pb)
500	16.48	1.363	22.46
1100	0.5881	1.331	0.7828
1500	0.1193	1.293	0.1543
2000	0.02123	1.214	0.02577
2500	0.004725	1.140	0.005387
3000	0.001319	1.151	0.001518

Table 11.3.: Cross section of the W' in the SSM. The samples are produced with PYTHIA6 in leading-order cross section and are scaled to next-to-next-to-leading-order cross section by using k-factors [83].

Dilepton resonance Z'_ψ

Various BSM theories predict additional resonances in the dilepton mass spectrum. The model chosen as a validation benchmark in this thesis postulates a new superordinate symmetry described by a gauge group SO(10) x $\mathrm{U}(1)_\psi$ which breaks into the known Standard Model at the TeV scale [60]. This new symmetry introduces an additional neutral gauge boson which is called Z'_ψ. The experimental signature is very similar to the Standard Model Z boson with a resonance in the invariant mass spectrum of lepton pairs located at the mass of the new boson which is a free parameter of the model. Signal

---

[2] The global tag used to describe the status of the detector is “START53 V7A-v1” and pileup was described with the scenario “S10”.

samples are again produced with PYTHIA6 and using the CTEQ6L1 pdf set. The cross section of various mass points can be found in Table 11.4. The full CMS simulation[3] as well as the Delphes simulation was performed in the same way as it was done before for the SSM W'. The sample production was done by the analysis group of [98]

Z'_ψ (GeV)	σ_{LO} (pb)	k-factor LO → NNLO	σ_{NNLO} (pb)
750	0.14	1.3	0.182
1000	0.0369	1.3	0.0479
1500	0.00433	1.3	0.005629
2000	$6.88 \cdot 10^{-4}$	1.3	$8.94 \cdot 10^{-4}$
2500	$1.27 \cdot 10^{-4}$	1.3	$1.65 \cdot 10^{-4}$
3000	$2.5 \cdot 10^{-5}$	1.3	$3.25 \cdot 10^{-5}$

Table 11.4.: Cross section of the Z'_ψ. The samples are produced with PYTHIA6 in leading-order (LO) cross section and are scaled to next-to-next-to-leading-order (NNLO) cross section by using a simplified constant k-factor [98].

Leptoquarks

The particles of the Standard Model are divided into quarks and leptons with the former ones carrying a quantum number called “baryon number” and the latter one carrying a quantum number called “lepton number” which both are conserved in all interactions described by the Standard Model. The leptoquark is a hypothetical particle that carries both baryon and lepton number and couples to both leptons and quarks. It is predicted by many extensions to the Standard Model such as grand unified theories, extended technicolor models and models that describe a lepton and quark substructure. The leptoquark considered in this study is described by an effective theory such as described in [99]. It is assumed that the leptoquarks exists in three generations without intergenerational mixing and that both baryon and lepton number are conserved at production and decay of each leptoquark. This means that these leptoquark are produced in pairs at the LHC and each decays into one lepton and one quark. The signal investigated in this study is limited to leptoquarks of the second generation which decay into one muon and one charm quark with a branching ratio of one. This results in a experimental signature of two muons and two jets in the final state with the two pairs of a muon and a jet arising from the same leptoquarks forming a resonance in their mass spectrum at the mass of the leptoquark. Signal samples were again produced with PYTHIA6 and using the CTEQ6L1 pdf set. The CMS detector simulation was done in the same way as

---

[3] The global tag used to describe the status of the detector is START53 V7C1-v1 and pileup was described with the scenario “S10”. The global tag has been switched from START53 V7A-v1 to START53 V7C1-v1 since a misalignment of the muon system had been found in the former one which influences the reconstruction of high p_T muons and was corrected in the latter version (for detailed study see [98]).

for the W' signal. The sample production was performed by the analysis group of [100]. The cross section of various mass points can be found in Table 11.5.

$\mathrm{m_{LQ}}$ (GeV)	σ_{NLO} (pb)
350	0.77
550	0.0431
750	$7.61 \cdot 10^{-3}$
950	$0.634 \cdot 10^{-3}$
1050	$0.256 \cdot 10^{-3}$

Table 11.5.: Cross section of the Leptoquark pair production. The cross sections are calculated at NLO [100].

11.3.2. Validation of the Delphes simulation of the example models

The first step of validating the results of the recast software consists of comparing characteristic kinematic distributions yielded from the full CMS simulation to the one yielded from Delphes for the three signal models. Using Delphes to calculate the signal efficiencies is only feasible if these distributions are in reasonably good agreement.

Sequential Standard Model $\mathbf{W'} \to \mathbf{e}\,\nu$ $(\mathbf{M_{W'} = 1.5\ TeV})$

Figure 11.4 shows the basic kinematic properties of the electron arising from the decay of the W' boson with a mass of 1.5 TeV and Figure 11.5 shows some additional distributions characterizing the decay and the electron energy reconstruction. Figure 11.6 shows the distribution of the number of jets in the signal events as well as the transverse momentum distribution of the leading jet. The Delphes results are in good agreement with the results produced with the full CMS simulation (Full Sim) in all distributions.

Dilepton resonance $\mathbf{Z'_{\psi}} \to \mu\,\mu$ $(\mathbf{M_{Z'} = 1.5\ TeV})$

Figure 11.7 shows the basic kinematic properties of the leading muon arising from the decay of the Z$'$ boson with a mass of 1.5 TeV. Good agreement is found between the results generated with Delphes and the ones generated with the full CMS simulation. Figure 11.8 shows the distributions of the invariant mass of the muon pair in the signal events in the inclusive and the jet-inclusive case. While the results in the former one are in good agreement, the results in the latter one show some deviation. The result of the Delphes simulation yields approximately 10% fewer events than it is the case for the full simulation. This deviation is caused by a slight mismodeling of photons as can be derived from the lower plot in Figure 11.8: The mass distribution of the 2μ 1γ `jet−incl.` event class shows an excess of events predicted by Delphes relative to the prediction from the full CMS simulation. These events are not included in the 2μ `jet−incl.` event class (upper right plot) which explains the correlated deficit in that class.

Fortunately, this mismodeling has no effect on the final result as can be seen in Figure 11.13 since the `2`μ `incl.` event class yields the best expected limit which is not effected by the photon reconstruction at all.

Figure 11.9 shows the MET properties of the signal simulation: The upper left plot shows the MET spectrum while the upper right plots shows the angle in the transverse plane between the four-vector sum of all jets and the vector of MET. The lower right plot shows the angle in the transverse plane between the leading muon and the vector of MET. All distributions are in reasonably good agreement considering the fact that the signal contains no intrinsic MET which means that all MET in the event is caused by mismeasurements. The lower left plot shows the muon resolution which is also in good agreement.

Leptoquark pair production ($\mathbf{M_{LQ} = 0.95}$ TeV)

Figure 11.10 shows the kinematic properties of the decay of a leptoquark pair with 0.95 TeV particle mass each. The left plot shows the invariant mass of the leading muon and the leading jet in the `1`μ `1 jet incl.` event class and the right plot shows the invariant mass calculated from the two leading muons and two leading jets in the `2`μ `2 jet incl.` event class. The first plot shows a sharp peak at the mass of the leptoquark while the second plot shows a broader peak at approximately twice the mass. The Delphes simulation and the full simulation are in good agreement.

Figure 11.11 four plots of additional signal properties: The upper left plot shows the number of muons and the upper right plot the number of jets. The lower left plots shows the distribution of MET and the lower right plot shows the angle in the transverse plane between the leading muon and the vector of MET. All plots are in reasonably good agreement.

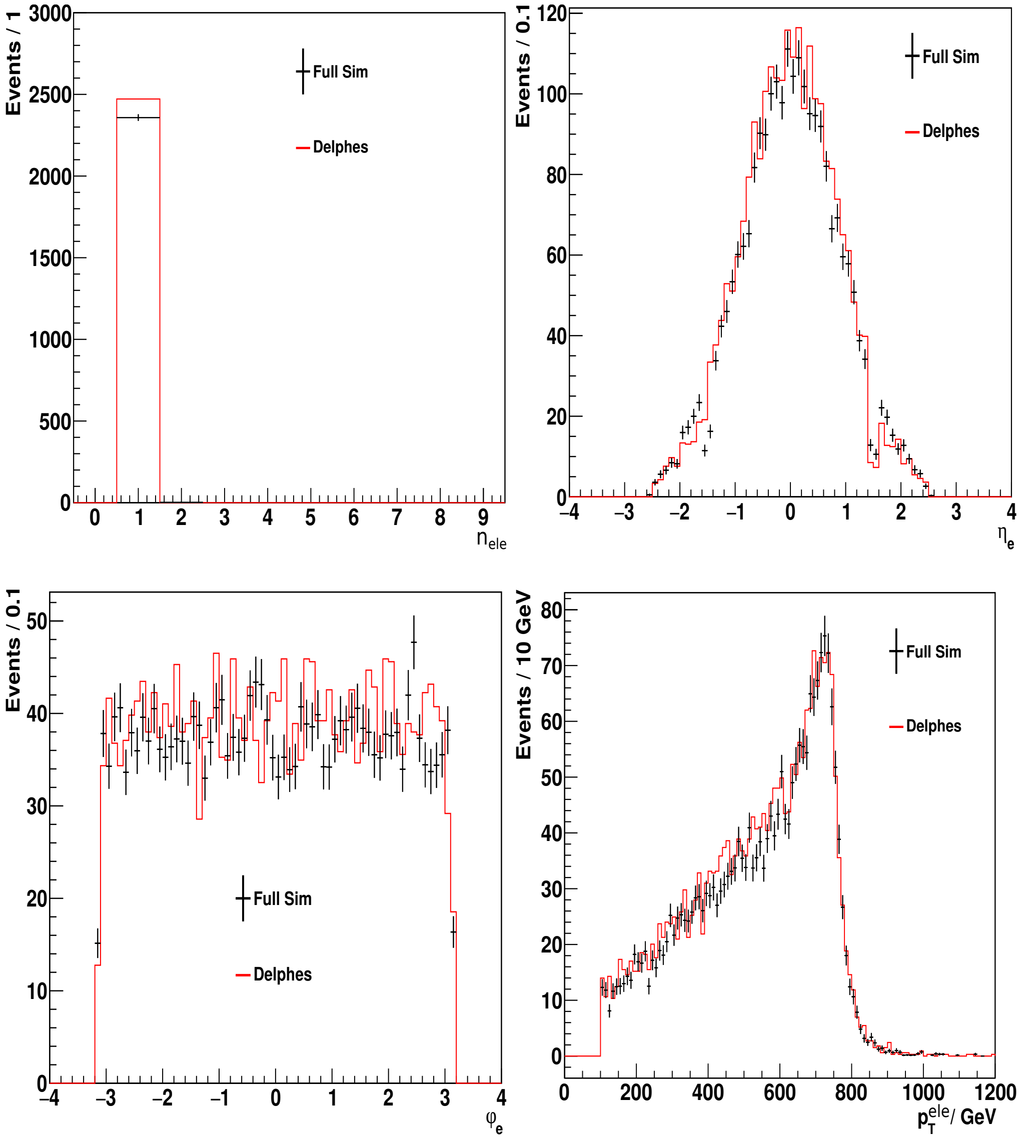

Figure 11.4.: SSM $W' \to e\,\nu$ ($M = 1.5$ TeV): Basic kinematic properties of the electron arising from the decay of the W' boson. The distributions are scaled to an integrated luminosity of 19.7 fb^{-1}. The results from the Delphes simulation and the full CMS simulation (Full Sim) are in good agreement.

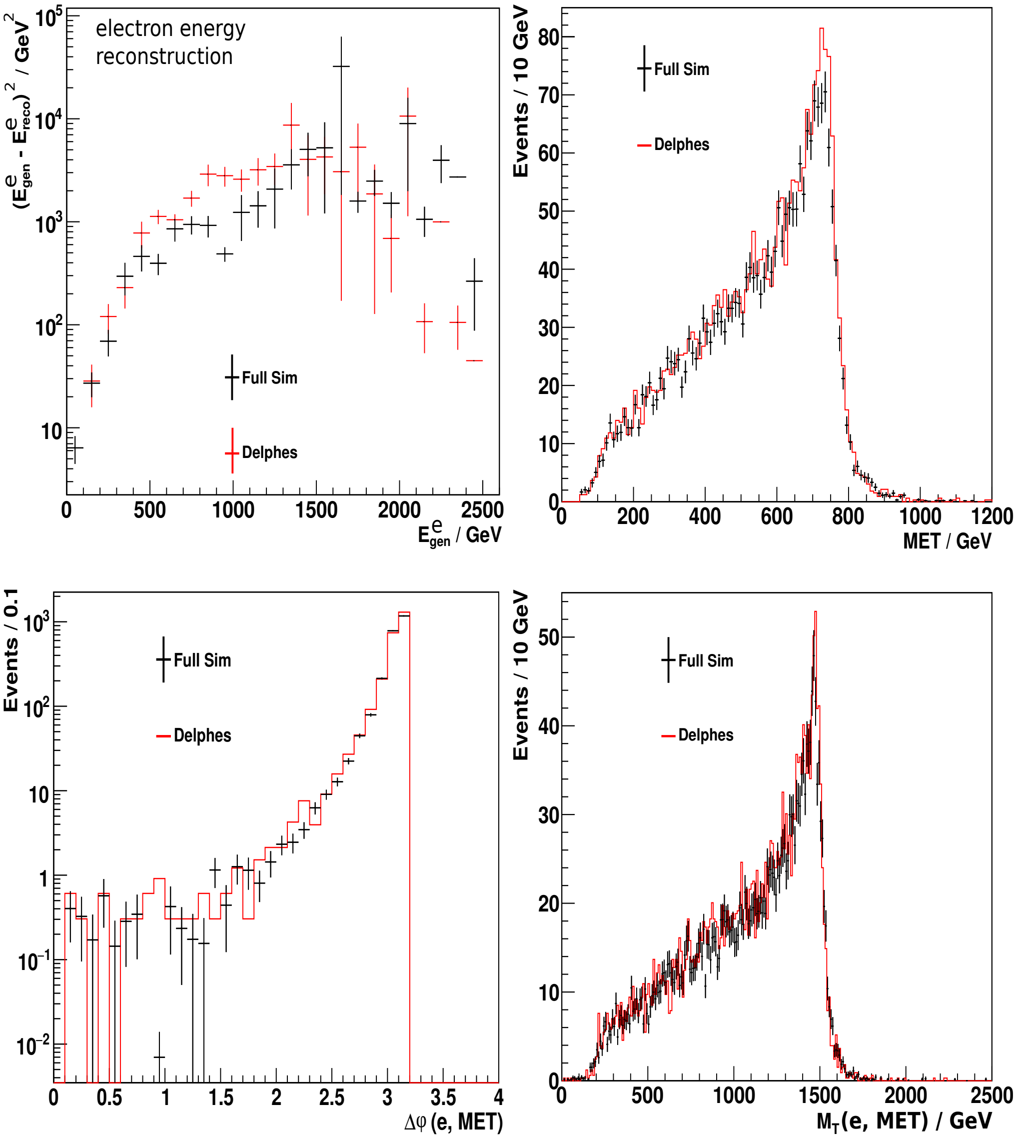

Figure 11.5.: SSM W′ → e ν (M = 1.5 TeV): Additional distributions characterizing the decay of the W' boson. The distributions are scaled to an integrated luminosity of 19.7 fb^{-1}. The results from the Delphes simulation and the full CMS simulation (Full Sim) are in good agreement.

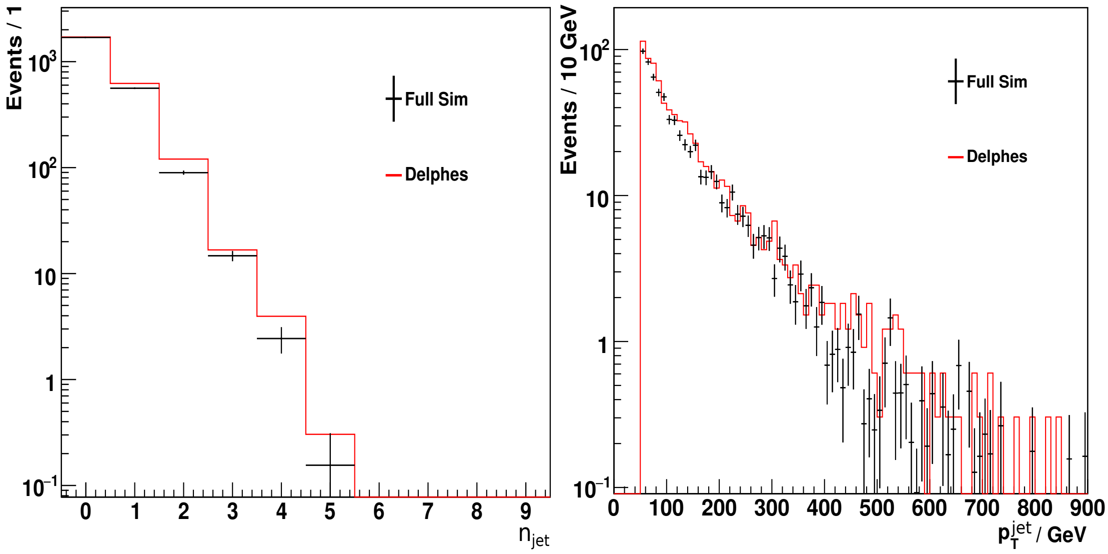

Figure 11.6.: SSM $W' \rightarrow e\ \nu$ ($M = 1.5$ TeV): Number of jets and transverse momentum distribution of the leading jet in the signal events. The distributions are scaled to an integrated luminosity of 19.7 fb^{-1}. The results from the Delphes simulation and the full CMS simulation (Full Sim) are in good agreement.

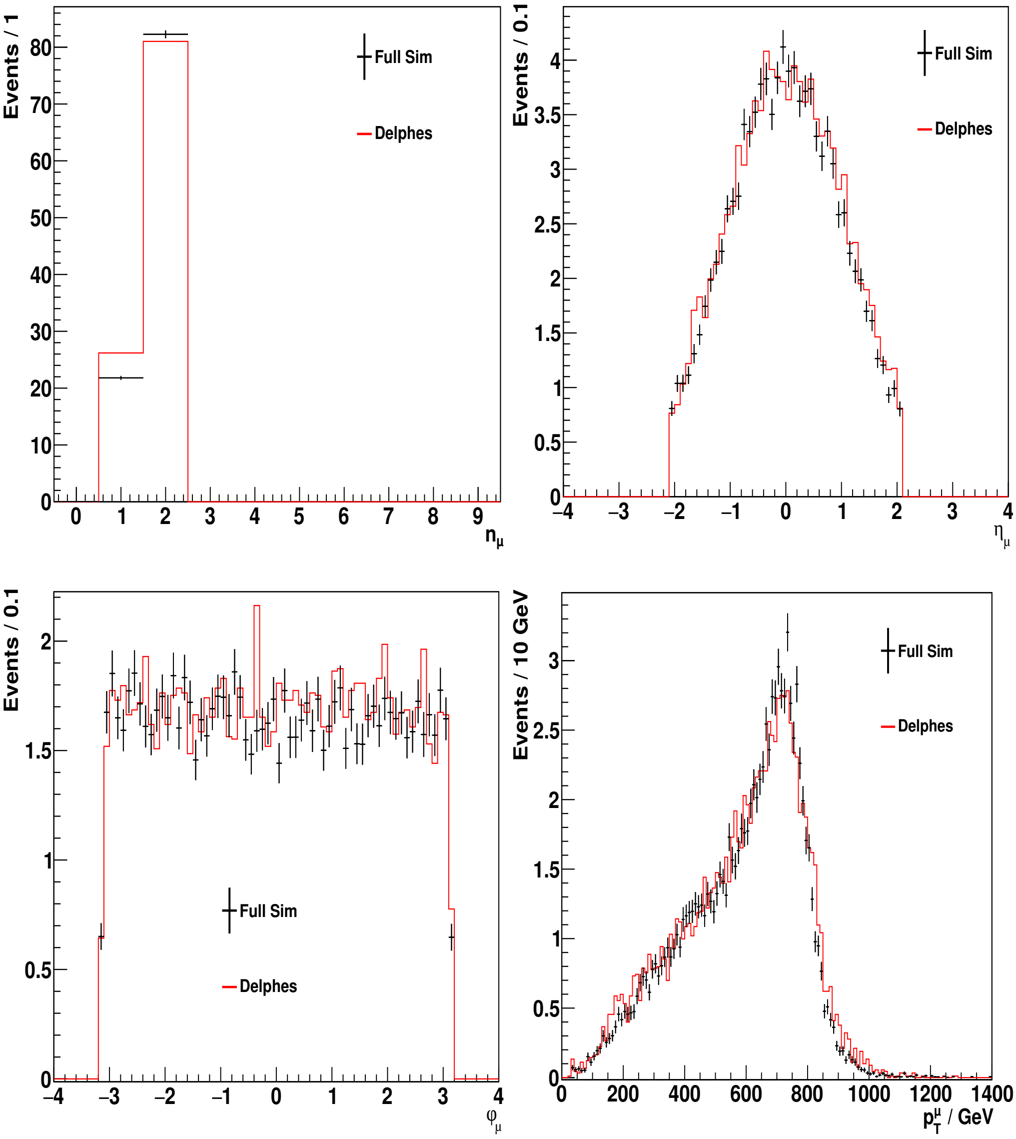

Figure 11.7.: $Z'_\psi \rightarrow \mu\ \mu$ (M = 1.5 TeV): Basic kinematic properties of the leading muon arising from the decay of the Z′ boson. The distributions are scaled to an integrated luminosity of 19.7 fb^{-1}. The results from the Delphes simulation and the full CMS simulation (Full Sim) are in good agreement.

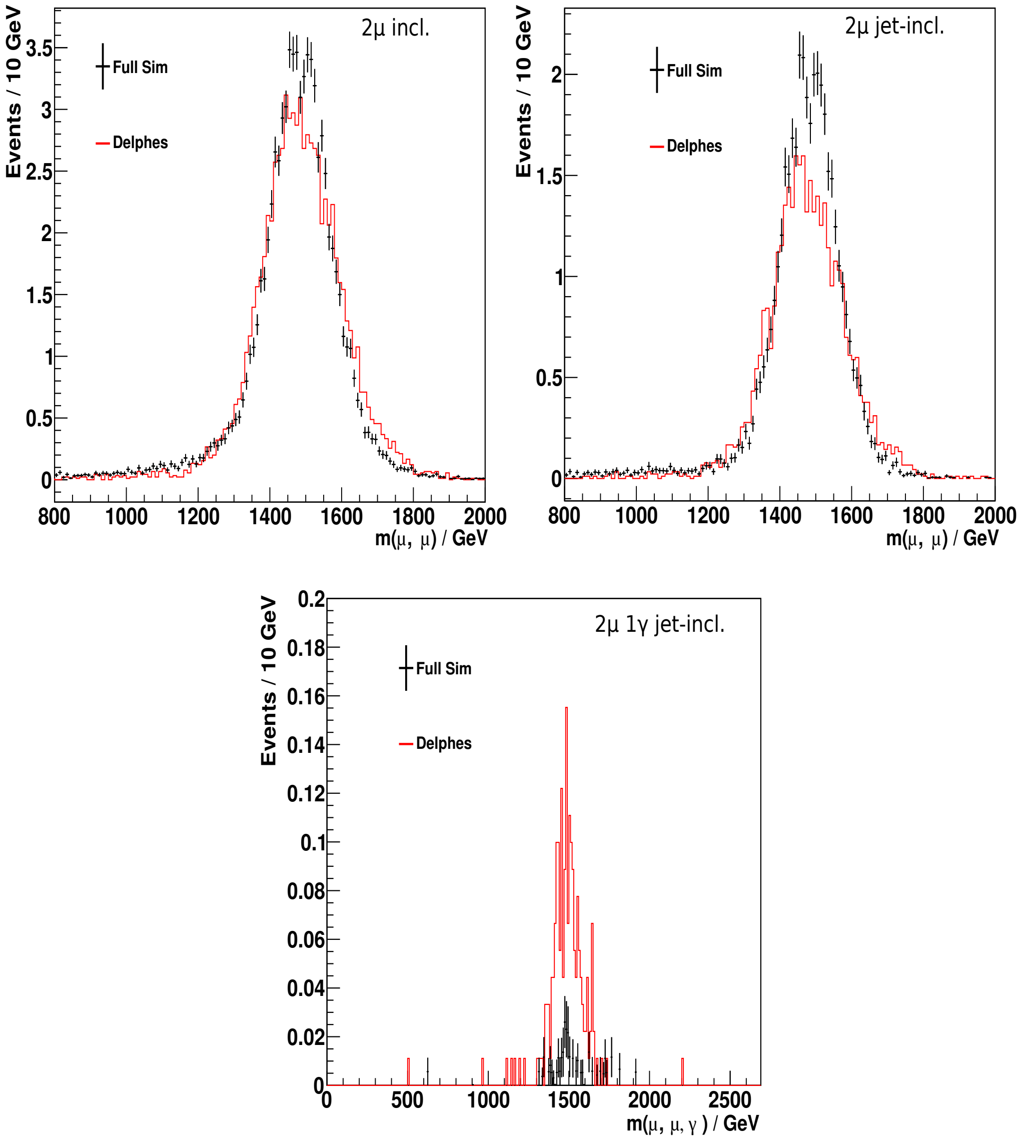

Figure 11.8.: $Z'_{\psi} \to \mu\ \mu$ (M = 1.5 TeV): Invariant mass distributions of three different event classes . The upper left plot shows the invariant mass for the 2μ `incl.` event class and the upper right plot for the 2μ `jet−incl.` event class. The distributions are scaled to an integrated luminosity of 19.7 fb^{-1}. For the former one, the result from the Delphes simulation and the full CMS simulation (Full Sim) are in good agreement while some discrepancy can be observed for the latter one ($\approx 10\%$ deficit in Delphes simulation). This deficit is caused by a slight mismodeling of the photon reconstruction which can be seen in the lower plot which shows the invariant mass distribution of the 2μ 1γ `jet−incl.` event class. The Delphes simulation contains more events with photons compared with the full Simulation which are therefore missing in the upper right plot.

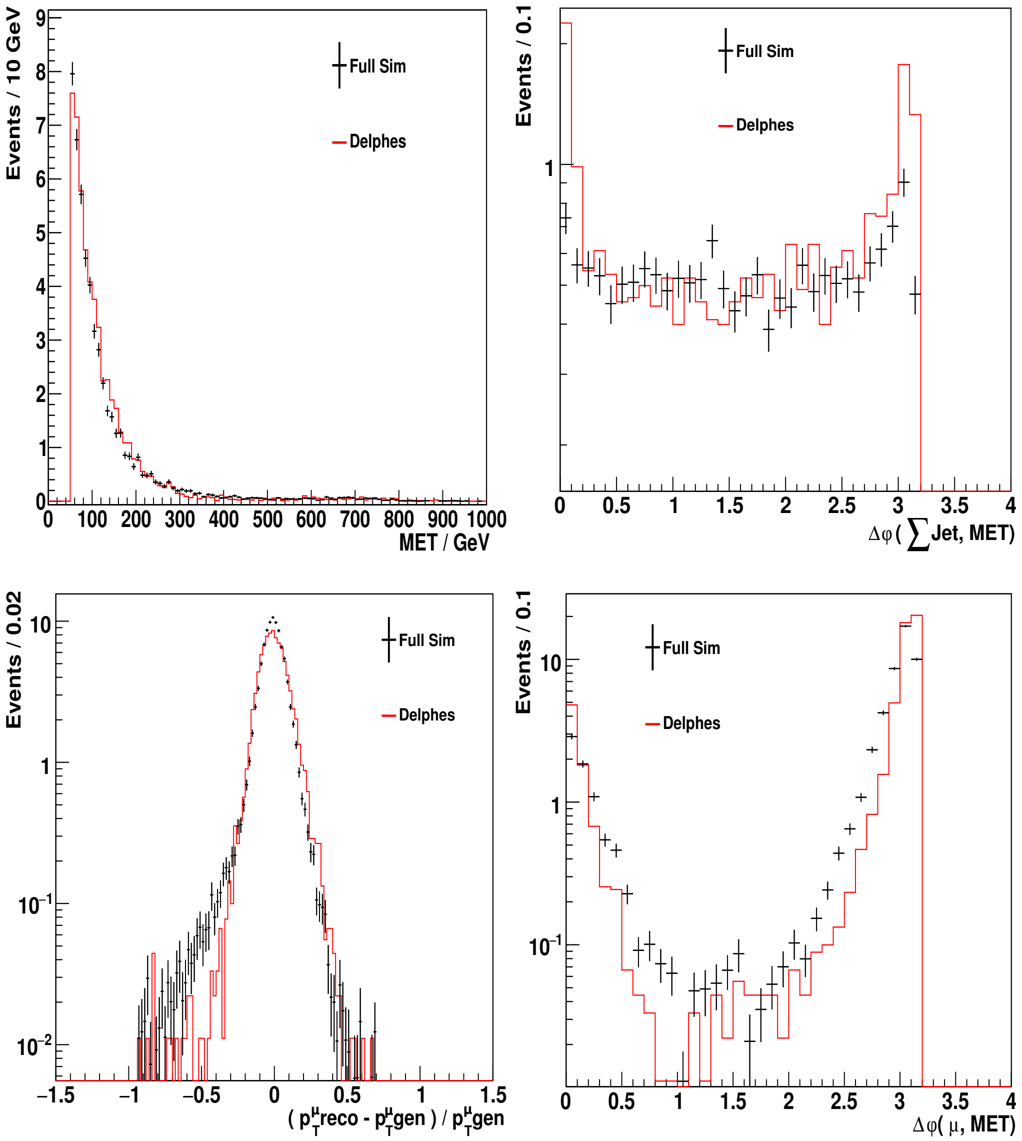

Figure 11.9.: $Z'_\psi \to \mu\,\mu$ (M = 1.5 TeV): MET investigation plots. The plot in the first row left shows the distribution of MET in the signal events. The distributions are scaled to an integrated luminosity of 19.7 fb^{-1}. Since the signal does not contain intrinsic MET, it is caused solely by mismeasurement ("fake MET"). The other three plots show event properties that are connected to the MET: The lower left plot shows the muon resolution. Since the two muons carry most of the momentum of the the final state, mismeasurement of the muons would be the main cause of fake MET. The two plots on the right show the ϕ angle between the MET vector and the muon (lower plot) and between the MET vector and the vector sum of all jets in the event (upper plot).

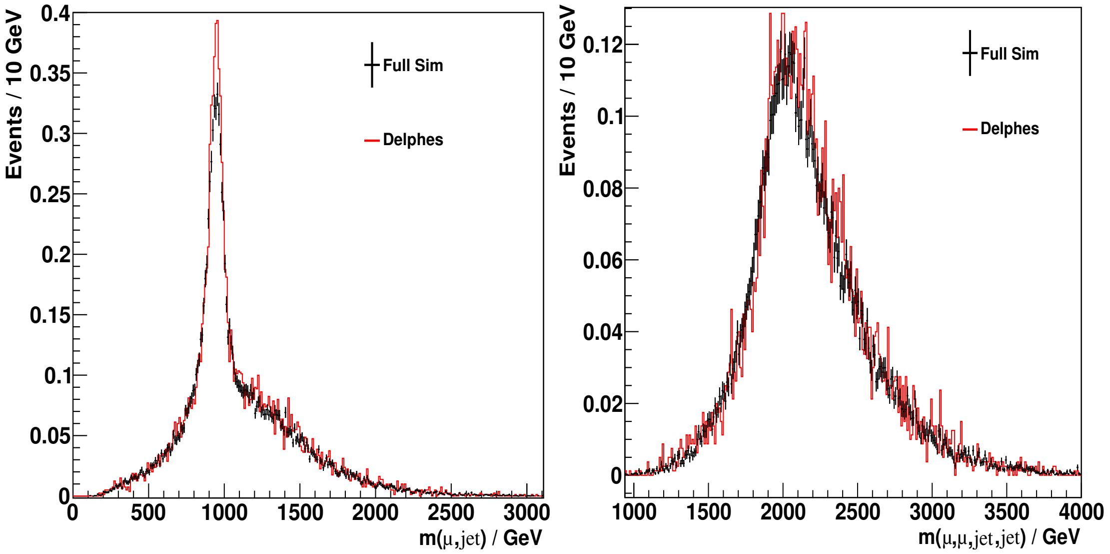

Figure 11.10.: Leptoquark pair production ($M_{LQ} = 0.95$ TeV). Invariant mass distributions in the 1μ `1jet incl.` event class (left) and 2μ `2jet incl.` event class (right). The distributions are scaled to an integrated luminosity of 19.7 fb^{-1}. The left plot shows a sharp peak at the mass of the leptoquark ($M_{LQ} = 0.95$ TeV) while the second one shows a broader peak at twice the mass. The results from the Delphes simulation and the full CMS simulation are in good agreement.

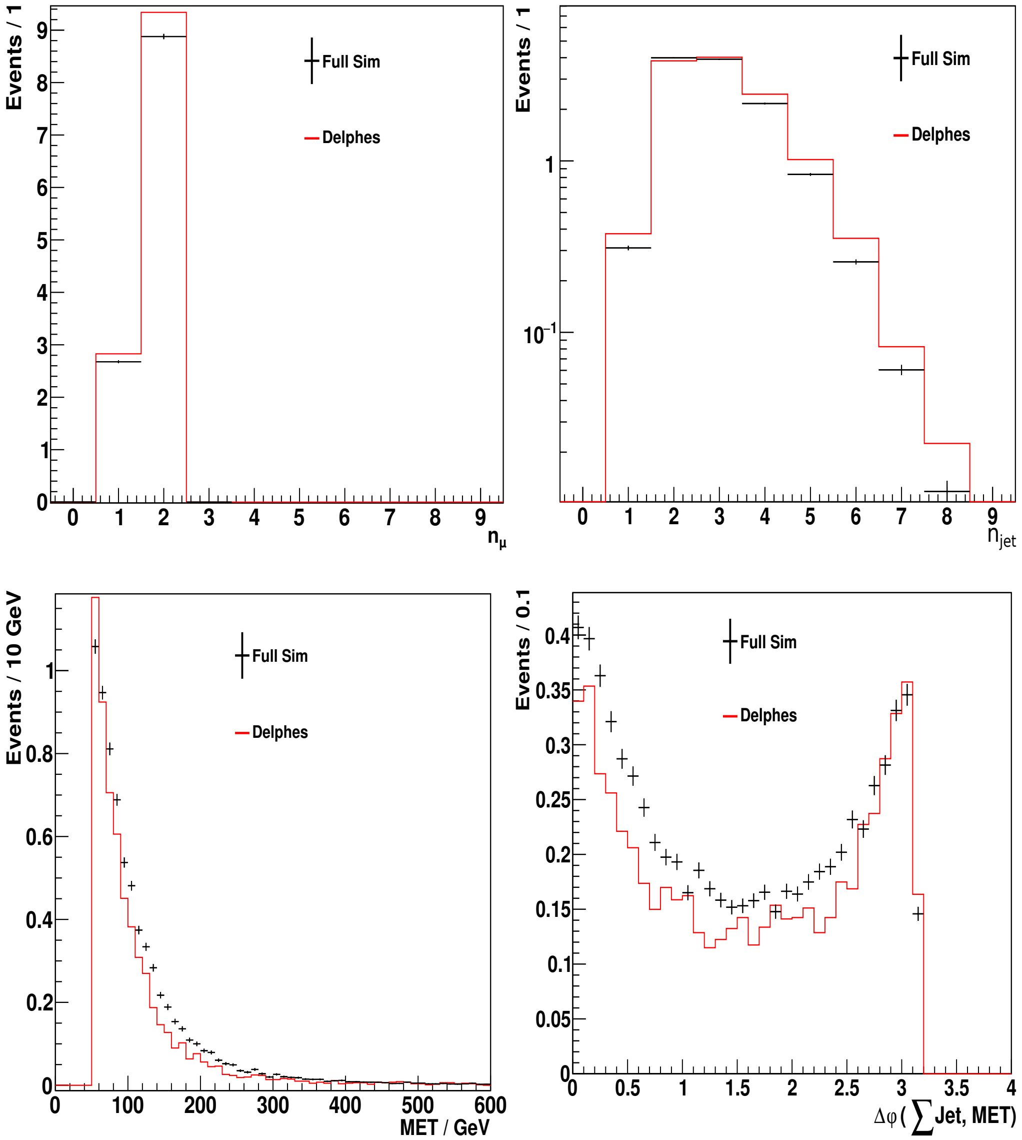

Figure 11.11.: Leptoquark pair production ($M_{LQ} = 0.95$ TeV): Additional distributions characterizing the decay of the two leptoquarks. The two upper plots show the number of muons and jets in the events. The lower left plot shows the MET distribution and the lower right plot shows the ϕ angle between the MET vector and the vector sum of all jets in the event. The results from the Delphes simulation and the full CMS simulation are in reasonably good agreement.

11.3.3. Results and comparison with dedicated analyses

The final step of the recast validation consists of the actual calculation of the exclusion limits for the three example theory mass points. The recasting is done with the Delphes signal simulation as well as with the full CMS simulation to estimate the influence of the Delphes simulation on the final result. Additionally, the results are compared to the exclusion limits published by CMS for these three models obtained with dedicated analyses.

Figure 11.12 shows the results for the 1.5 TeV mass point of the SSM $\mathrm{W}' \to \mathrm{e}\,\nu$ model. The left plots shows the result obtained with the Delphes simulation and the right plot the one obtained with the full CMS simulation. The most sensitive class for both cases is the `1e 1MET jet-incl.` event class.

The simulated spectrum of the signal is superimposed on the kinematic distribution of the data and the Standard Model expectation with the green dotted lines indicating the most sensitive kinematic region.

The observed limit obtained with the Delphes simulation is 1.33 fb and the limit obtained with the full CMS simulation is 1.39 fb. Both results are in reasonable agreement where the full CMS simulation result is slightly more conservative ($\approx 4\,\%$). The limit published by CMS for this mass point of this model is approximately 1 fb [101] which shows that the recast procedure produces useful results.

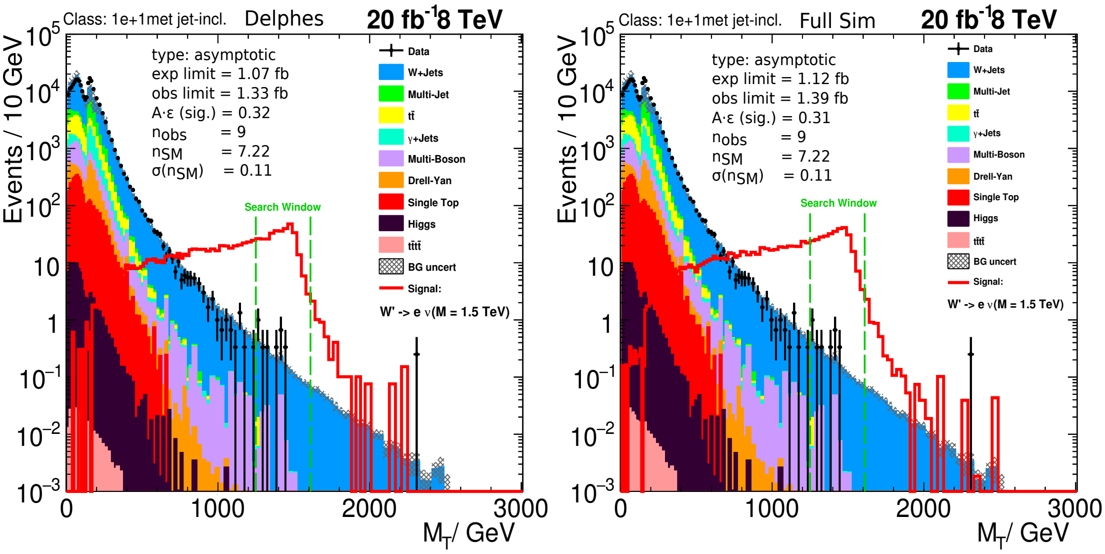

Figure 11.12.: $\mathrm{W}' \to \mathrm{e}\,\nu$ (M = 1.5 TeV): Result of the recasting procedure for the first example theory obtained with the Delphes simulation (left) and with the full CMS simulation(right). The kinematic distribution yielding the best expected limit is shown together with the limit results and input values. Both methods yield comparable results. The green dotted lines indicate the most sensitive kinematic region determined by the recast algorithm.

Figure 11.13 shows the results for the 1.5 TeV mass point of the $\mathrm{Z}'_{\psi} \to \mu\,\mu$ model.

Again, the left plots shows the result obtained with the Delphes simulation and the right plot the one obtained with the full CMS simulation. The most sensitive class for both cases is the 2μ `incl.` event class.

The observed limit is 0.45 fb for both the results obtained with the Delphes simulation and the full CMS simulation within the rounding precision. This limit is competitive to the dedicated analysis which published a limit for this mass point of this model of approximately 0.44 fb [59].

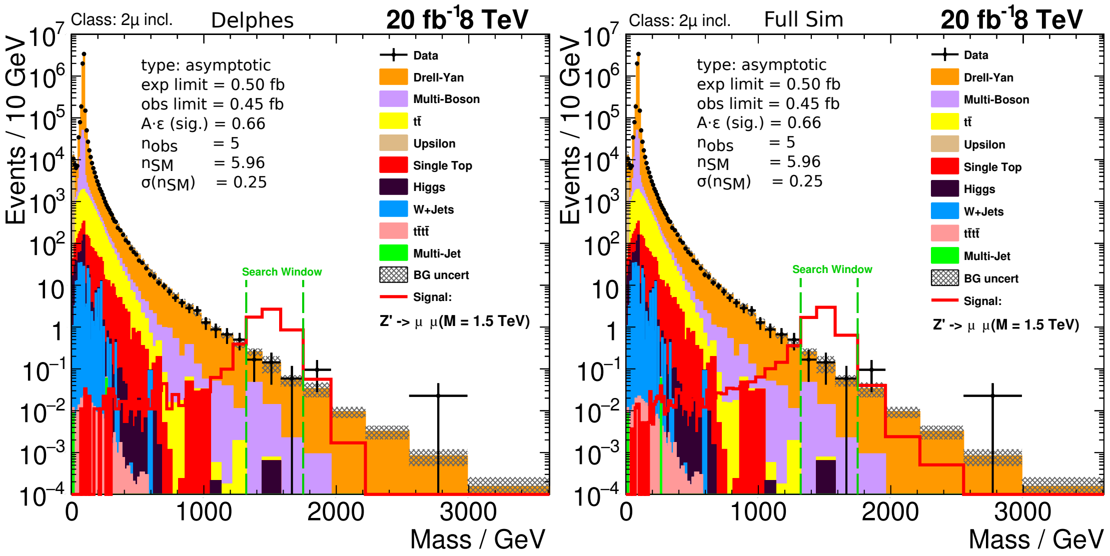

Figure 11.13.: $Z'_\psi \to \mu\,\mu$ (M = 1.5 TeV): Result of the recasting procedure for the second example theory obtained with the Delphes simulation (left) and with the full CMS simulation(right). The kinematic distribution yielding the best expected limit is shown together with the limit results and input values. Both methods yield comparable results. The green dotted lines indicate the most sensitive kinematic region determined by the recast algorithm.

Figure 11.14 shows the results for the 0.95 TeV mass point of the Leptoquark pair production (M_{LQ} = 0.95 TeV) model: The Delphes simulation (left plot) and the full CMS simulation (right plot) both yield the same event class (2μ `2jet incl.`) as the most sensitive class. In contrast to the first two models where the (transverse) mass distribution yielded the best limit, the most sensitive distribution for the leptoquark model is the $\sum p_T$ distribution. The results from both types of simulation are in good agreement: The Delphes simulation yields an observed limit of 1.41 fb while the full CMS simulation yields an observed limit of 1.51 fb. The dedicated analysis performed for this leptoquark model by the CMS collaboration yields an observed limit of 0.3 fb [102] for the 950 GeV mass point which is approximately five times stronger than the limit obtained with METAL results. This is due to the fact that the dedicated analysis uses different selections based on the kinematic properties of the process which cannot be done with METAL. These selections improve the sensitivity of the dedicated analyses to this signal compared to METAL. This is not the case for the first two example models since close to no signal specific selections are applied by these analyses.

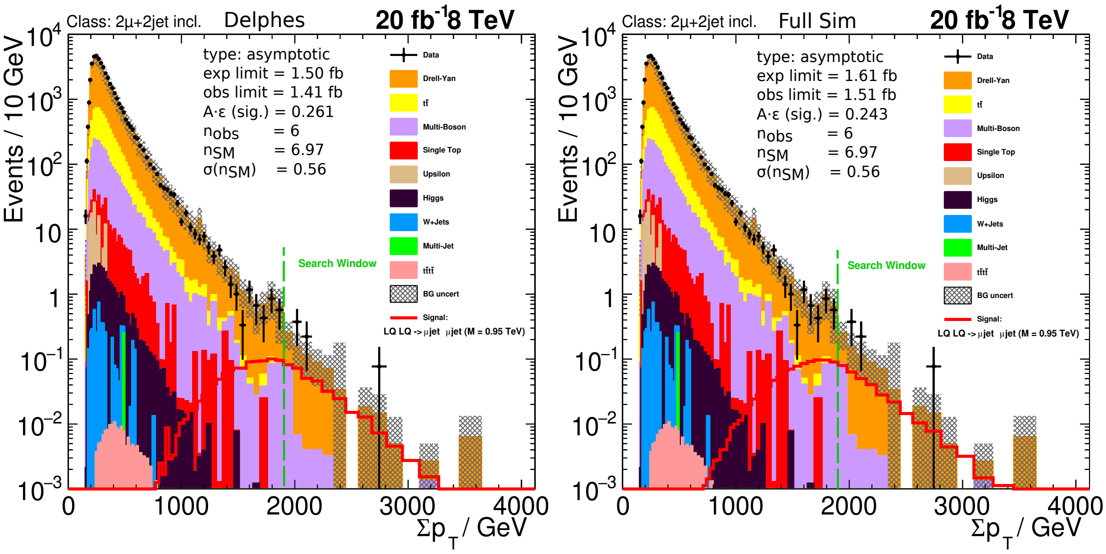

Figure 11.14.: Leptoquark pair production ($M_{LQ} = 0.95$ TeV): Result of the recasting procedure for the third example theory obtained with the Delphes simulation (left) and with the full CMS simulation(right). The kinematic distribution yielding the best expected limit is shown together with the limit results and input values. Both methods yield comparable results. The green dotted lines indicate the most sensitive kinematic region determined by the recast algorithm.

The first two example model signal points are excluded in both the Delphes and CMS simulation cases since the theoretically predicted cross sections ($\sigma(W'\ (M = 1.5\ \text{TeV})) = 154.3$ fb, $\sigma(Z'_\psi\ (M = 1.5\ \text{TeV})) = 5.63$ fb) are well above the observed exclusion limits. The leptoquark model signal point cannot be excluded with METAL since the theoretically predicted cross section ($\sigma(\text{LQ LQ})(M = 0.95\ \text{TeV})) = 0.634$ fb) is smaller than the exclusion limit.

11.3.4. Conclusion on the recast procedure

The investigated example models show overall a good agreement between the results obtained with the Delphes simulation, the full CMS simulation and for the first two examples ($\sigma(\mathrm{W}'\ (\mathrm{M} = 1.5\ \mathrm{TeV}))$, $\sigma(\mathrm{Z}'_{\psi}\ (\mathrm{M} = 1.5\ \mathrm{TeV}))$) even with the results of dedicated analyses. Control plots show a slight mismodeling of the $\sigma(\mathrm{Z}'_{\psi}\ (\mathrm{M} = 1.5\ \mathrm{TeV}))$ signal in the final state containing one photon and two muons. This mismodeling should only have a small influence on the results of the limit reinterpretation for most possible signals that do not contain photons at tree level since the most sensitive final state will most likely be one without photons. In case that photons are part of the signature of the model of interest (or anytime the excluded cross-section is very close to the theoretical predicted one) it is advised to contact the MUSiC working group who can rerun the limit calculation using the full CMS simulation.

12. Conclusion and Outlook

In this thesis the development of the software framework METAL was presented. The purpose of this work is to provide a fast and easy to use way of testing and constraining models for new phenomena using the results of the MUSiC classification. Various validations were performed proving the applicability of the chosen approach.

Limits on three example models (one W-like and one Z-like heavy resonance and the pair production of second generation leptoquarks) have been calculated using the software framework and the results have been compared to those of dedicated analyses for the three models. For the chosen mass values of the W-like and one Z-like resonances, METAL yields not only feasible results but also shows similar sensitivity proving that it can even be competitive to dedicated analyses under certain circumstances. The more complex signature of the leptoquark signal leads to a reduced sensitivity of METAL to this model compared to the dedicated analysis. Selections exploiting the kinematic properties of the signal are used in the dedicated analysis which are not applied in METAL.

In the last years, a trend has become apparent over a wide range of particle physics projects to present results in a model independent fashion in order to make them more useful for later usage by other physicists. METAL has the potential to become an important part of this development. At the moment, its usage is constrained to members of the CMS collaboration only, but further efforts of the MUSiC working group will hopefully lead to a public release in the near future.

Part IV.

Appendix

A. Standard Model Simulation Samples

Process	Details	Generator	k-factor (order)	# Events
γ+Jets		PYTHIA6	1.3 (NLO)	$1.6 \cdot 10^6$
W+Jets		MadGraph	1.21 (NNLO)	$6.0 \cdot 10^7$
	$M_{l^\pm\nu} > 200$ GeV	MadGraph	1.21 (NNLO)	$1.2 \cdot 10^6$
	$H_\mathrm{T} > 150$ GeV	MadGraph	1.21 (NNLO)	$4.3 \cdot 10^7$
	Wbb $\rightarrow l^\pm\nu$bb	MadGraph	1.79 (NLO)	$2.0 \cdot 10^7$
Drell-Yan	$M_{l^\pm l^\pm} > 10$ GeV	MadGraph	1.2 (NNLO)	$6.0 \cdot 10^7$
	$p_\mathrm{T}(Z) > 50$ GeV	MadGraph	1.0 (LO)	$3.8 \cdot 10^8$
	$M_{l^\pm l^\pm} > 200$ GeV	POWHEG	1.02 (NNLO)	$2.2 \cdot 10^6$
	Z+Jets $\rightarrow \nu\nu$	MadGraph	1.0 (LO)	$3.0 \cdot 10^7$
Multi-Boson	$\gamma\gamma$	PYTHIA6	1.0 (LO)	$7.7 \cdot 10^6$
	WW	PYTHIA6	1.63 (NLO)	$1.0 \cdot 10^7$
	$\mathrm{W}^\pm\mathrm{W}^\pm$	MadGraph	1.0 (LO)	$1.8 \cdot 10^5$
	WW via DPS	PYTHIA6	1.0 (LO)	$8.0 \cdot 10^5$
	gg $\rightarrow$ WW	gg2VV	1.4 (NLO)	$1.0 \cdot 10^5$
	ZZ $\rightarrow 4l^\pm$	POWHEG	1.0 (NLO)	$1.5 \cdot 10^7$
	ZZ $\rightarrow 2l^\pm$2q, $2l^\pm 2\nu$, 2q2ν	MadGraph	1.0 (LO)	$2.7 \cdot 10^6$
	gg $\rightarrow$ ZZ	gg2VV	1.0 (NLO)	$9.0 \cdot 10^5$
	WZ	MadGraph	1.0 (LO)	$7.9 \cdot 10^6$
	Vγ	MadGraph	1.2 (NLO)	$1.0 \cdot 10^7$
	WWW	MadGraph	0.98 (NLO)	$2.0 \cdot 10^5$
	ZZZ	MadGraph	1.2 (NLO)	$2.0 \cdot 10^5$
	WWZ	MadGraph	0.92 (NLO)	$2.0 \cdot 10^5$
	WZZ	MadGraph	1.02 (NLO)	$2.0 \cdot 10^5$
	WWγ	MadGraph	1.0 (LO)	$5.0 \cdot 10^5$
	W$\gamma\gamma$	MadGraph	1.0 (LO)	$2.0 \cdot 10^6$
Multi-Jet		PYTHIA6	1.0 (LO)	$4.5 \cdot 10^8$
Single Top		POWHEG	1.04-1.34 (NNLL)	$5.2 \cdot 10^6$
t$\bar{\mathrm{t}}$		POWHEG	1.0 (NNLO)	$2.6 \cdot 10^7$
	t$\bar{\mathrm{t}}$ ($M_{tt} > 700$ GeV)	POWHEG	1.11 (NNLO)	$4.0 \cdot 10^6$
	t$\bar{\mathrm{t}}\gamma$	MadGraph	1.0 (LO)	$1.0 \cdot 10^6$
	t$\bar{\mathrm{t}}$W	MadGraph	1.08 (NLO)	$1.0 \cdot 10^5$
	t$\bar{\mathrm{t}}$Z	MadGraph	1.2 (NLO)	$2.0 \cdot 10^5$
	t$\bar{\mathrm{t}}$WW	MadGraph	1.0 (LO)	$2.0 \cdot 10^5$
t$\bar{\mathrm{t}}$t$\bar{\mathrm{t}}$		MadGraph	1.28 (NLO)	$9.0 \cdot 10^4$
Higgs	gg $\rightarrow$ ZZ	MiNLO	1.0 (NLO)	$8.0 \cdot 10^5$
	gg $\rightarrow$ bb, $\gamma\gamma$, $\tau\tau$, Zγ, WW	POWHEG	1.0 (NLO)	$2.6 \cdot 10^6$
	VBF $\rightarrow$ bb, $\gamma\gamma$, $\tau\tau$, Zγ, VV	POWHEG	1.0 (NLO)	$2.5 \cdot 10^6$
	WH $\rightarrow \mu\mu$, bb	POWHEG	1.0 (NLO)	$1.1 \cdot 10^6$
	ZH $\rightarrow \mu\mu$, bb	POWHEG	1.0 (NLO)	$2.9 \cdot 10^6$
	TTH $\rightarrow$ bb, $\gamma\gamma$, Zγ	PYTHIA6	1.0 (NLO)	$1.2 \cdot 10^6$
	WH, ZH $\rightarrow \gamma\gamma$, Zγ	PYTHIA6	1.0 (NLO)	$1.1 \cdot 10^6$
	WH, ZH, TTH $\rightarrow \tau\tau$, VV	PYTHIA6	1.0 (NLO)	$9.0 \cdot 10^5$
Upsilon	Y(1S)/Y(2S)/Y(3S) $\rightarrow \mu\mu$	EVTGEN	1.0 (LO)	$5.0 \cdot 10^6$

Figure A.1.: Summary of the Standard Model simulation datasets (taken from [2]).

B. The METAL Reinterpretation Tool

B.1. General information

The following instruction explains how to set up the METAL reinterpretation tool called "METAL Forge", download the needed input files and how to use the tool. In order to download the tool and the needed input files, it is necessary to have access to the CMS gitlab group and to CERNS's afs file system. The tool was developed and tested on a system with the following specifications:

- **OS:** Scientific Linux release 6.8 Carbon
- **Kernel:** Linux 2.6.32-642.13.1.el6.x86_64
- **Python:** 2.6.6
- **ROOT:** 5.34/34
- **pythia:** 8210

Correct functionality cannot be guaranteed on systems with different specifications.

B.2. Set up the tool

Set up Delphes

You need a dedicaed version from Delphes in order to run the tool:

1. Source on gitlab: https://gitlab.cern.ch/knutzen/delphes_for_metal.git
2. Clone this repository on your local machine or add it to an existing Delphes installation.
3. Change to branch: **delphes_for_metal**
4. Compile the new version.
5. If you want to run on LHE files, you have to make sure that pythia8 is installed on your system and Delphes is correctly configured in order to run pythia8 internally (for more information see the Delphes homepage https://cp3.irmp.ucl.ac.be/projects/delphes).

Set up METAL forge

1. Clone https://gitlab.cern.ch/knutzen/METAL_forge.git on your local machine.

2. Get the necessary input files(class_plots.tar.gz, limit_maps.tar.gz) from: /afs/cern.ch/user/k/knutzen/public/METAL_files

3. Unpack the two files (tar -xf *.tar.gz)

B.3. How to run the tool

1. Source Delphes:
   cd PATH_TO_DELPHES_BASE_DIR; source DelphesEnv.sh

2. Source METAL forge:
   cd PATH_TO_METAL_forge_BASE_DIR; source set_env.sh

3. Go to a directory of your choice

4. Run the program:
   python PATH_TO_METAL_forge_BASE_DIR/recast_limit.py modelinputfile (HepMC or LHE) **-x** cross_section_of_model (in fb) **-p** ABS_PATH_TO_limit_maps_folder (created from limit_maps.tar.gz) **-c** PATH_TO_class_plots.root (created from class_plots.tar.gz) **-d** PATH_TO_DELPHES_BASE_DIR

5. An example HepMC file
   (**ZprimePSIToMuMu_M_1500_TuneZ2star_8TeV_pythia6_cff.dat**)
   can be found in
   /afs/cern.ch/user/k/knutzen/public/METAL_files.
   It corresponds to the example model introduced in Section 11.3.1 and discussed in Section 11.3.3.

B.4. Output of the tool

The main result of the reinterpretation is summarized in the command line at the end of the output produced by the tool. This comprises the message whether the model is excluded or not, the event class and distribution that yielded the best expected limit, the region within this distribution that yielded the best expected limit, the signal efficiency in this region, as well as the values for the expected and observed exclusion limit.

Additionally, a folder is created that contains two root files which provide the kinematic distributions containing the best expected limit and the one that contains the second best expected limit. The name of these root files indicate the event class as well as the kinematic distribution which they contain.

The folder does also contain a log file (limitResult.txt) that contains the limit values as well as additional information like the number of observed events, expected background events and its uncertainty in the selected kinematic regions of all distributions that have been investigated for this model.

All other files in the folder are intermediate results produced during the reinterpretation which are of no interest for the normal user.

B.5. Contact

In case you have any questions or problems with the tool or you want to give feedback, please contact:

simon.knutzen@rwth-aachen.de (Simon Knutzen, author)

C. Delphes Optimization

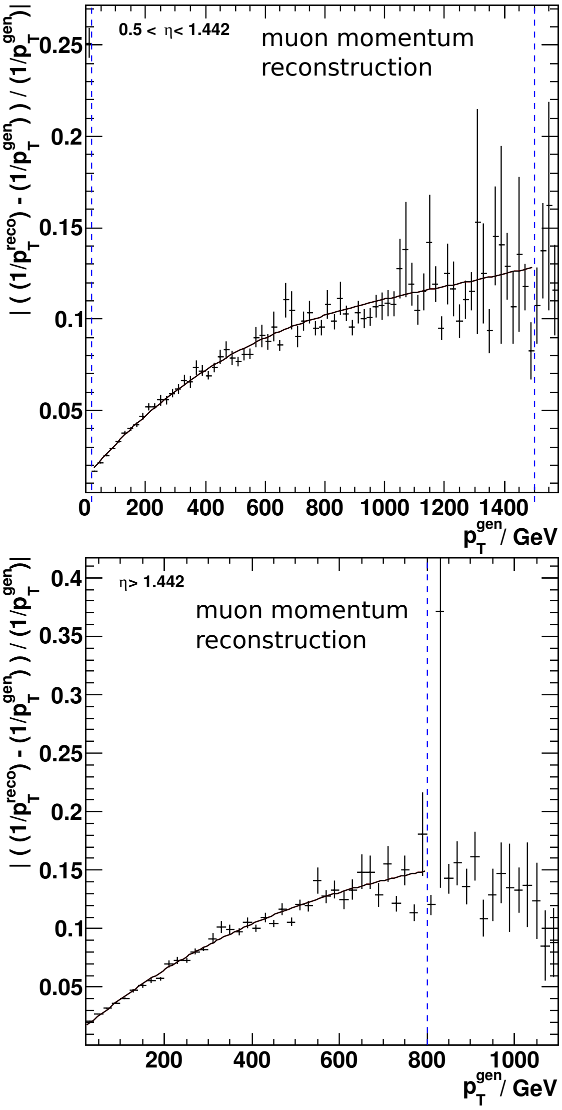

Figure C.1.: Determination of the parameterization of the inverse muon transverse momentum smearing in the pseudo-rapidity bins of $0.5 < |\eta| < 1.442$ (left) and $1.442 < |\eta|$ (right).

D. Delphes Parameter Card

In the following, the full Delphes parameter card used by the METAL framework is stated. It contains all parameterizations needed in order to emulate the detector response and reconstruction algorithms.

```
#######################################
# Order of execution of various modules
#######################################

set ExecutionPath {
  ParticlePropagator

  ChargedHadronTrackingEfficiency
  ElectronTrackingEfficiency
  MuonTrackingEfficiency

  ChargedHadronMomentumSmearing
  ElectronEnergySmearing
  MuonMomentumSmearing

  TrackMerger
  Calorimeter
  AntiElectronFilter

  PhotonEnergySmearing

  EFlowMerger
  EFlowIsoForEleMerger
  EFlowIsoForGamMerger

  PhotonEfficiency
  PhotonIsolation

  ElectronEfficiency
  ElectronIsolation

  MuonEfficiency
  MuonIsolation
```

```
  NeutrinoFilter
  GenJetFinder
  GenMissingET

  FastJetFinder

  JetEnergyScale

  JetFlavorAssociation

  BTagging
  TauTagging

  UniqueObjectFinder

  MissingET

  ScalarHT

  TreeWriter
}

#################################
# Propagate particles in cylinder
#################################

module ParticlePropagator ParticlePropagator {
  set InputArray Delphes/stableParticles

  set OutputArray stableParticles
  set ChargedHadronOutputArray chargedHadrons
  set ElectronOutputArray electrons
  set MuonOutputArray muons

  # radius of the magnetic field coverage, in m
  set Radius 1.29
  # half-length of the magnetic field coverage, in m
  set HalfLength 3.00

  # magnetic field
  set Bz 3.8
}
```

```
####################################
# Charged hadron tracking efficiency
####################################

module Efficiency ChargedHadronTrackingEfficiency {
  set InputArray ParticlePropagator/chargedHadrons
  set OutputArray chargedHadrons

  # add EfficiencyFormula {efficiency formula as a function of eta and pt}
  # tracking efficiency formula for charged hadrons
  set EfficiencyFormula { (pt <= 0.1)   * (0.00) + \
  (abs(eta) <= 1.5) * (pt > 0.1   && pt <= 1.0)   * (0.85) + \
  (abs(eta) <= 1.5) * (pt > 1.0)                  * (0.97) + \
  (abs(eta) > 1.5 && abs(eta) <= 2.5) * (pt > 0.1 && pt <= 1.0) * (0.85) + \
  (abs(eta) > 1.5 && abs(eta) <= 2.5) * (pt > 1.0)              * (0.90) + \
  (abs(eta) > 1.5 && abs(eta) <= 2.5) * (pt > 1.0)              * (0.85) +
  (abs(eta) > 2.5)                                               * (0.00)}
}

##############################
# Electron tracking efficiency
##############################

module Efficiency ElectronTrackingEfficiency {
  set InputArray ParticlePropagator/electrons
  set OutputArray electrons

  # set EfficiencyFormula {efficiency formula as a function of eta and pt}
  # tracking efficiency formula for electrons
  set EfficiencyFormula { (pt <= 0.1)   * (0.00) +
   (abs(eta) <= 1.5) * (pt > 0.1   && pt <= 1.0)   * (0.73) +
   (abs(eta) <= 1.5) * (pt > 1.0   && pt <= 1.0e2) * (0.95) +
   (abs(eta) <= 1.5) * (pt > 1.0e2)                * (0.99) +
   (abs(eta) > 1.5 && abs(eta) <= 2.5) * (pt > 0.1 && pt <= 1.0)   * (0.50) +
   (abs(eta) > 1.5 && abs(eta) <= 2.5) * (pt > 1.0 && pt <= 1.0e2) * (0.83) +
   (abs(eta) > 1.5 && abs(eta) <= 2.5) * (pt > 1.0e2)              * (0.90) +
   (abs(eta) > 2.5)                                                 * (0.00)}
}

##########################
# Muon tracking efficiency
##########################
```

```
module Efficiency MuonTrackingEfficiency {
  set InputArray ParticlePropagator/muons
  set OutputArray muons

  # tracking efficiency formula for muons
  set EfficiencyFormula { (pt <= 0.1)   * (0.00) +
   (abs(eta) <= 1.5) * (pt > 0.1   && pt <= 1.0)   * (0.75) +
   (abs(eta) <= 1.5) * (pt > 1.0)                  * (0.99) +
   (abs(eta) > 1.5 && abs(eta) <= 2.5) * (pt > 0.1 && pt <= 1.0) * (0.70) +
   (abs(eta) > 1.5 && abs(eta) <= 2.5) * (pt > 1.0)              * (0.98) +
   (abs(eta) > 2.5)                                              * (0.00)}
}

########################################
# Momentum resolution for charged tracks
########################################

module MomentumSmearing ChargedHadronMomentumSmearing {
  set InputArray ChargedHadronTrackingEfficiency/chargedHadrons
  set OutputArray chargedHadrons

  # resolution formula for charged hadrons
  set ResolutionFormula {
   (abs(eta) <= 1.5) * (pt > 0.1   && pt <= 1.0) * (0.015) + \
   (abs(eta) <= 1.5) * (pt > 1.0   && pt <= 1.0e1)* (0.013) + \
   (abs(eta) <= 1.5) * (pt > 1.0e1 && pt <= 2.0e2) * (0.02) + \
   (abs(eta) <= 1.5) * (pt > 2.0e2)                * (0.05) + \
   (abs(eta) > 1.5 && abs(eta) <= 2.5) * (pt > 0.1 && pt <= 1.0)   * (0.015) + \
   (abs(eta) > 1.5 && abs(eta) <= 2.5) * (pt > 1.0 && pt <= 1.0e1) * (0.015) + \
   (abs(eta) > 1.5 && abs(eta) <= 2.5) * (pt > 1.0e1 && pt <= 2.0e2) * (0.04) + \
   (abs(eta) > 1.5 && abs(eta) <= 2.5) * (pt > 2.0e2)                * (0.05)}

}


#################################
# Energy resolution for electrons
#################################

module EnergySmearing ElectronEnergySmearing {
  set InputArray ElectronTrackingEfficiency/electrons
  set OutputArray electrons

  set ResolutionFormula { \
```

```
      (abs(eta) <= 2.5) * (energy > 0.1   && energy <= 2.5e1) * (energy*0.015) + \
      (abs(eta) <= 2.5) * (energy > 2.5e1)\
      * sqrt(energy^2*0.005^2 + energy*0.027^2 + 0.15^2) + \
      (abs(eta) > 2.5 && abs(eta) <= 3.0)\
      * sqrt(energy^2*0.005^2 + energy*0.027^2 + 0.15^2) + \
      (abs(eta) > 3.0 && abs(eta) <= 5.0)\
      * sqrt(energy^2*0.08^2 + energy*1.97^2)}

}

###############################
# Momentum resolution for muons
###############################

module InverseMomentumSmearing MuonMomentumSmearing {
  set InputArray MuonTrackingEfficiency/muons
  set OutputArray muons
  # resolution formula for muons
  set ResolutionFormula {
     (abs(eta) <= 0.5) * (pt > 20 && pt < 1000) * ( (0.010036227)\
     + (0.000243722)*pt + \
     (-2.77319022794e-07)*pt*pt +(1.33691585312e-10)*pt*pt*pt) + \
     (abs(eta) <= 0.5) * (pt > 1000 && pt < 2000) * ( (0.06494291)\
     + (4.46126224913e-05)*pt) + \
     (abs(eta) <= 0.5) * (pt > 2000 ) * (0.154) + \
     (abs(eta) > 0.5 && abs(eta) <= 1.442) * (pt > 20 && pt < 1500)\
     * ( (0.01362482) + (0.0001926859)*pt +\
     (-1.3143856616e-07)*pt*pt + (3.60972831842e-11)*pt*pt*pt) + \
     (abs(eta) > 0.5 && abs(eta) <= 1.442) * (pt > 1500 ) * (0.12874) + \
     (abs(eta) > 1.442) * (pt > 20 && pt < 800) * ( (0.01011625893) +\
     (0.0003187498)*pt + \
     (-2.39859692431e-07)*pt*pt + (7.42107538779e-11)*pt*pt*pt) + \
     (abs(eta) > 1.442) * (pt > 800 ) * (0.14956) \

  }
}

##############
# Track merger
##############

module Merger TrackMerger {
# add InputArray InputArray
  add InputArray ChargedHadronMomentumSmearing/chargedHadrons
```

```
  add InputArray ElectronTrackingEfficiency/electrons
  #add InputArray ElectronEnergySmearing/electrons
  add InputArray MuonMomentumSmearing/muons
  set OutputArray tracks
}

#############
# Calorimeter
#############

module Calorimeter Calorimeter {
  set ParticleInputArray ParticlePropagator/stableParticles
  #set ParticleInputArray TrackMerger/tracks
  set TrackInputArray TrackMerger/tracks
  #set TrackInputArray ElectronEnergySmearing/electrons

  set TowerOutputArray towers
  set PhotonOutputArray photons

  set EFlowTrackOutputArray eflowTracks
  set EFlowPhotonOutputArray eflowPhotons
  set EFlowNeutralHadronOutputArray eflowNeutralHadrons

  set ECalEnergyMin 0.5
  set HCalEnergyMin 1.0

  set ECalEnergySignificanceMin 1.0
  set HCalEnergySignificanceMin 1.0

  set SmearTowerCenter true

  set pi [expr {acos(-1)}]

  # lists of the edges of each tower in eta and phi
  # each list starts with the lower edge of the first tower
  # the list ends with the higher edged of the last tower

  # 5 degrees towers
  set PhiBins {}
  for {set i -36} {$i <= 36} {incr i} {
    add PhiBins [expr {$i * $pi/36.0}]
  }
  foreach eta {-1.566 -1.479 -1.392 -1.305 -1.218 -1.131 -1.044 -0.957
     -0.87 -0.783 -0.696 -0.609 -0.522 -0.435 -0.348 -0.261 -0.174 -0.087
```

```
   0 0.087 0.174 0.261 0.348 0.435 0.522 0.609 0.696 0.783 0.87 0.957
   1.044 1.131 1.218 1.305 1.392 1.479 1.566 1.653} {
  add EtaPhiBins $eta $PhiBins
}

# 10 degrees towers
set PhiBins {}
for {set i -18} {$i <= 18} {incr i} {
  add PhiBins [expr {$i * $pi/18.0}]
}
foreach eta {-4.35 -4.175 -4 -3.825 -3.65 -3.475 -3.3 -3.125 -2.95
   -2.868 -2.65 -2.5 -2.322 -2.172 -2.043 -1.93 -1.83 -1.74 -1.653
   1.74 1.83 1.93 2.043 2.172 2.322 2.5 2.65 2.868 2.95 3.125 3.3
   3.475 3.65 3.825 4 4.175 4.35 4.525} {
  add EtaPhiBins $eta $PhiBins
}

# 20 degrees towers
set PhiBins {}
for {set i -9} {$i <= 9} {incr i} {
  add PhiBins [expr {$i * $pi/9.0}]
}
foreach eta {-5 -4.7 -4.525 4.7 5} {
  add EtaPhiBins $eta $PhiBins
}

# default energy fractions {abs(PDG code)} {Fecal Fhcal}
add EnergyFraction {0} {0.0 1.0}
# energy fractions for e, gamma and pi0
add EnergyFraction {11} {1.0 0.0}
add EnergyFraction {22} {1.0 0.0}
add EnergyFraction {111} {1.0 0.0}
# energy fractions for muon, neutrinos and neutralinos
add EnergyFraction {12} {0.0 0.0}
add EnergyFraction {13} {0.0 0.0}
add EnergyFraction {14} {0.0 0.0}
add EnergyFraction {16} {0.0 0.0}
add EnergyFraction {1000022} {0.0 0.0}
add EnergyFraction {1000023} {0.0 0.0}
add EnergyFraction {1000025} {0.0 0.0}
add EnergyFraction {1000035} {0.0 0.0}
add EnergyFraction {1000045} {0.0 0.0}
# energy fractions for K0short and Lambda
add EnergyFraction {310} {0.3 0.7}
```

```
  add EnergyFraction {3122} {0.3 0.7}

  # set ECalResolutionFormula {resolution formula as a function of eta and energy}
  set ECalResolutionFormula { \
    (abs(eta) <= 3.0) * sqrt(energy^2*0.005^2 + energy*0.027^2 + 0.15^2) + \
   (abs(eta) > 3.0 && abs(eta) <= 5.0) * sqrt(energy^2*0.08^2 + energy*1.97^2)}

  # set HCalResolutionFormula {resolution formula as a function of eta and energy}
  set HCalResolutionFormula {\
   (abs(eta) <= 1.7) * sqrt(energy^2*0.0302^2 + energy*0.5205^2 + 1.59^2) + \
   (abs(eta) > 1.7 && abs(eta) <= 3.2) * sqrt(energy^2*0.050^2 + energy*0.706^2) + \
   (abs(eta) > 3.0 && abs(eta) <= 4.9) * sqrt(energy^2*0.05^2 + energy*1.00^2)}


}

#######################
# Electron Track merger
#######################

#module Merger EleTrackMerger {
#  add InputArray TrackMerger/tracks
#  add InputArray ElectronEnergySmearing/electrons
#  set OutputArray tracks
#}

######################
# Anti Electron filter
######################

module PdgCodeFilter AntiElectronFilter {
  set InputArray Calorimeter/eflowTracks
  set OutputArray eflowTracksNoEle
  set Invert false
  add PdgCode {11}
  add PdgCode {-11}
}

###############################
# Energy resolution for photons
###############################
#
module EnergySmearing PhotonEnergySmearing {
  set InputArray Calorimeter/eflowPhotons
```

```
  set OutputArray photons
  set ResolutionFormula {(abs(eta) < 1.442) * (energy > 0.1   && energy <= 60. )\
     * (sqrt( energy*0.3125 + 4.25 ) ) + \
      (abs(eta) < 1.442) * (energy > 60. && energy <= 400. ) * \
      ( sqrt( ( energy^3*(4.698166e-06) + energy^2*(-0.0029050) + \
      energy*( 1.0088180) + (-28.735) ) ) ) + \
      (abs(eta) < 1.442) * (energy > 400. && energy <= 1000. ) * \
      ( sqrt( ( energy^2*(0.002112897372) + energy*(-1.0694199) + \
      (303.040980) ) ) ) + \
      (abs(eta) < 1.442) * (energy > 1000. && energy <= 1600. ) * \
      ( sqrt( ( energy*(3.86780762) + (-2586.4065) ) ) ) +  \
      (abs(eta) < 1.442) * (energy > 1600. ) * ( (60.017) ) +  \
      (abs(eta) > 1.56) * (energy > 0.1   && energy <= 30. )  * \
      (sqrt( energy*0.3125 + 4.25) ) + \
      (abs(eta) > 1.56) * (energy > 30. && energy <= 200. )   * \
      ( sqrt( ( energy^3*(-4.15834e-05) + energy^2*(0.01607559) + \
      energy*(-1.4466821) + (77.953034) ) )  ) + \
      (abs(eta) > 1.56) * (energy > 200. && energy <= 1000. )  * \
      ( sqrt( ( energy^3*(-1.384421e-07) + energy^2*(0.0007773) + \
      energy*(0.083254676) + (61.9656464) ) ) )  +  \
      (abs(eta) > 1.56) * (energy > 1000. && energy <= 1800. ) * \
      ( sqrt( ( energy*(1.47093835) + (-603.14703) ) ) ) + \
      (abs(eta) > 1.56) * (energy > 1800. ) * ( (45.22) )
  }
}

####################
# Energy flow merger
####################

module Merger EFlowMerger {
# add InputArray InputArray
  add InputArray AntiElectronFilter/eflowTracksNoEle
  add InputArray PhotonEnergySmearing/photons
  add InputArray Calorimeter/eflowNeutralHadrons
  add InputArray ElectronEnergySmearing/electrons
  set OutputArray eflow
}

module Merger EFlowIsoForGamMerger {
  add InputArray ElectronEnergySmearing/electrons
  add InputArray AntiElectronFilter/eflowTracksNoEle
  add InputArray Calorimeter/eflowNeutralHadrons
  set OutputArray eflowGamIso
```

```
}

module Merger EFlowIsoForEleMerger {
  add InputArray AntiElectronFilter/eflowTracksNoEle
  add InputArray Calorimeter/eflowPhotons
  add InputArray Calorimeter/eflowNeutralHadrons
  set OutputArray eflowEleIso
}



###################
# Photon efficiency
###################
module Efficiency PhotonEfficiency {
  set InputArray PhotonEnergySmearing/photons
  #set InputArray Calorimeter/eflowPhotons
  set OutputArray photons

  # set EfficiencyFormula {efficiency formula as a function of eta and pt}

  # efficiency formula for photons
  set EfficiencyFormula {
  (pt <= 10.0) * (0.00) + \
  (abs(eta) <= 1.5) * (pt > 10.0)  * (0.95) + \
  (abs(eta) > 1.5 && abs(eta) <= 2.5) * (pt > 10.0)  * (0.85) + \
  (abs(eta) > 2.5)                                   * (0.00)}
}

##################
# Photon isolation
##################

module Isolation PhotonIsolation {
  set CandidateInputArray PhotonEfficiency/photons
  set IsolationInputArray EFlowIsoForGamMerger/eflowGamIso

  set OutputArray photons

  set DeltaRMax 0.3

  set PTMin 0.5

  set PTRatioMax 0.12
```

```
}

#################
# Electron filter
#################

#module PdgCodeFilter ElectronFilter {
#  set InputArray Calorimeter/eflowTracks
#  set OutputArray electrons
#  set Invert true
#  add PdgCode {11}
#  add PdgCode {-11}
#}


#####################
# Electron efficiency
#####################

module Efficiency ElectronEfficiency {
  set InputArray ElectronEnergySmearing/electrons
  set OutputArray electrons
  set EfficiencyFormula {(pt <= 10.0) * (0.00) +
               (abs(eta) <= 1.5) * (pt > 10.0)  * (0.95) +
       (abs(eta) > 1.5 && abs(eta) <= 2.5) * (pt > 10.0)  * (0.85) +
       (abs(eta) > 2.5)                                   * (0.00)}
}

####################
# Electron isolation
####################

module Isolation ElectronIsolation {
  set CandidateInputArray ElectronEfficiency/electrons
  set IsolationInputArray EFlowIsoForEleMerger/eflowEleIso

  set OutputArray electrons

  set DeltaRMax 0.3

  set PTMin 1.0

  set PTRatioMax 0.4
}
```

```
#################
# Muon efficiency
#################

module Efficiency MuonEfficiency {
  set InputArray MuonMomentumSmearing/muons
  set OutputArray muons

  # set EfficiencyFormula {efficiency as a function of eta and pt}

  # efficiency formula for muons

    set EfficiencyFormula {
     (pt <= 10.0) * (0.00) +
     (abs(eta) <= 1.5) * (pt > 10.0 && pt <= 1.0e3) * (0.95) +
     (abs(eta) <= 1.5) * (pt > 1.0e3)
     * (0.95 * exp(0.5 - pt*5.0e-4)) +
     (abs(eta) > 1.5 && abs(eta) <= 2.4)
     * (pt > 10.0 && pt <= 1.0e3) * (0.95) +
     (abs(eta) > 1.5 && abs(eta) <= 2.4)
     * (pt > 1.0e3) * (0.95 * exp(0.5 - pt*5.0e-4)) +
     (abs(eta) > 2.4) }
}

################
# Muon isolation
################

module Isolation MuonIsolation {
  set CandidateInputArray MuonEfficiency/muons
  set IsolationInputArray EFlowMerger/eflow

  set OutputArray muons

  set DeltaRMax 0.3

  set PTMin 1.0

  set PTRatioMax 0.4
}
```

```
##################
# Scalar HT merger
##################

module Merger ScalarHT {
  add InputArray UniqueObjectFinder/jets
  add InputArray UniqueObjectFinder/electrons
  add InputArray UniqueObjectFinder/photons
  add InputArray UniqueObjectFinder/muons
  set EnergyOutputArray energy
}

###################
# Missing ET merger
###################


module Merger MissingET {
  add InputArray EFlowMerger/eflow
  set MomentumOutputArray momentum
}

#####################
# Neutrino Filter
#####################

module PdgCodeFilter NeutrinoFilter {

  set InputArray Delphes/stableParticles
  set OutputArray filteredParticles

  set PTMin 0.0

  add PdgCode {12}
  add PdgCode {14}
  add PdgCode {16}
  add PdgCode {-12}
  add PdgCode {-14}
  add PdgCode {-16}

}


#####################
```

```
# MC truth jet finder
#####################

module FastJetFinder GenJetFinder {
  set InputArray NeutrinoFilter/filteredParticles

  set OutputArray jets

  # algorithm: 1 CDFJetClu, 2 MidPoint, 3 SIScone,
  # 4 kt, 5 Cambridge/Aachen, 6 antikt
  set JetAlgorithm 6
  set ParameterR 0.5

  set JetPTMin 20.0
}

#########################
# Gen Missing ET merger
########################

module Merger GenMissingET {
# add InputArray InputArray
  add InputArray NeutrinoFilter/filteredParticles
  set MomentumOutputArray momentum
}



############
# Jet finder
############

module FastJetFinder FastJetFinder {
#  set InputArray Calorimeter/towers
  set InputArray EFlowMerger/eflow

  set OutputArray jets

  # algorithm: 1 CDFJetClu, 2 MidPoint, 3 SIScone,
  # 4 kt, 5 Cambridge/Aachen, 6 antikt
  set JetAlgorithm 6
  set ParameterR 0.5

  set JetPTMin 20.0
```

```
}

##################
# Jet Energy Scale
##################

module EnergyScale JetEnergyScale {
  set InputArray FastJetFinder/jets
  set OutputArray jets

  # scale formula for jets
  set ScaleFormula {sqrt( (2.5 - 0.15*(abs(eta)))^2 / pt + 1.0 )}
}

########################
# Jet Flavor Association
########################

module JetFlavorAssociation JetFlavorAssociation {

  set PartonInputArray Delphes/partons
  set ParticleInputArray Delphes/allParticles
  set ParticleLHEFInputArray Delphes/allParticlesLHEF
  set JetInputArray JetEnergyScale/jets

  set DeltaR 0.5
  set PartonPTMin 1.0
  set PartonEtaMax 2.5

}

###########
# b-tagging
###########

module BTagging BTagging {
  set JetInputArray JetEnergyScale/jets

  set BitNumber 0

  # add EfficiencyFormula {abs(PDG code)}
  # {efficiency formula as a function of eta and pt}
  # PDG code = the highest PDG code of a quark or
  # gluon inside DeltaR cone around jet axis
```

```
  # gluon's PDG code has the lowest priority

  # based on arXiv:1211.4462

  # default efficiency formula (misidentification rate)
  add EfficiencyFormula {0} {0.01+0.000038*pt}

  # efficiency formula for c-jets (misidentification rate)
  add EfficiencyFormula {4} {0.25*tanh(0.018*pt)*(1/(1+ 0.0013*pt))}

  # efficiency formula for b-jets
  add EfficiencyFormula {5} {0.85*tanh(0.0025*pt)*(25.0/(1+0.063*pt))}
}

#############
# tau-tagging
#############

module TauTagging TauTagging {
  set ParticleInputArray Delphes/allParticles
  set PartonInputArray Delphes/partons
  set JetInputArray JetEnergyScale/jets

  set DeltaR 0.5

  set TauPTMin 1.0

  set TauEtaMax 2.5

  # default efficiency formula (misidentification rate)
  add EfficiencyFormula {0} {0.01}
  # efficiency formula for tau-jets
  add EfficiencyFormula {15} {0.6}
}

#####################################################
# Find uniquely identified photons/electrons/tau/jets
#####################################################

module UniqueObjectFinder UniqueObjectFinder {
# earlier arrays take precedence over later ones
# add InputArray InputArray OutputArray
  add InputArray MuonIsolation/muons muons
  add InputArray ElectronIsolation/electrons electrons
```

```
  add InputArray PhotonIsolation/photons photons
  add InputArray JetEnergyScale/jets jets
}

##################
# ROOT tree writer
##################

# tracks, towers and eflow objects are not stored by default in the output.
# if needed (for jet constituent or other studies), uncomment the relevant
# "add Branch ..." lines.

module TreeWriter TreeWriter {
# add Branch InputArray BranchName BranchClass
  add Branch Delphes/allParticles Particle GenParticle

  add Branch TrackMerger/tracks Track Track
  add Branch Calorimeter/towers Tower Tower

  add Branch Calorimeter/eflowTracks EFlowTrack Track
  add Branch Calorimeter/eflowPhotons EFlowPhoton Tower
  add Branch Calorimeter/eflowNeutralHadrons EFlowNeutralHadron Tower

  add Branch GenJetFinder/jets GenJet Jet
  add Branch GenMissingET/momentum GenMissingET MissingET

  add Branch UniqueObjectFinder/jets Jet Jet
  add Branch UniqueObjectFinder/electrons Electron Electron
  #add Branch ElectronEnergySmearing/electrons Ele Electron
  add Branch UniqueObjectFinder/photons Photon Photon
  #add Branch PhotonEfficiency/photons Pho Photon
  add Branch UniqueObjectFinder/muons Muon Muon
  add Branch MissingET/momentum MissingET MissingET
  add Branch ScalarHT/energy ScalarHT ScalarHT
}
```

Bibliography

[1] D. Duchardt, "Model Unspecific Search for New Physics in pp Collisions at sqrt(s) = 8 TeV". PhD thesis, RWTH Aachen University. Soon to be published.

[2] CMS Collaboration, "MUSiC, a Model Unspecific Search for New Physics, in pp Collisions at $\sqrt{s} = 8$ TeV", *CMS Physics Analysis Summary CMS-PAS-EXO-14/016* (2017).

[3] M. E. Peskin and D. V. Schroeder, "An introduction to quantum field theory". Advanced book program. Westview Press Reading (Mass.), 1995.

[4] L. Edelhäuser and A. Knochel, "Tutorium Quantenfeldtheorie". Springer Berlin Heidelberg, 2016.

[5] T. Hebbeker, "Skript zur Vorlesung Elementarteilchenphysik I / II", RWTH 2007.

[6] P. A. M. Dirac, "The Quantum Theory of the Electron", *Proc. R. Soc. Lond.* **117** (Feb, 1928) 610–624. `doi:10.1098/rspa.1928.0023`.

[7] S. Glashow, "Partial Symmetries of Weak Interactions", *Nucl.Phys.* **22** (1961) 579–588. `doi:10.1016/0029-5582(61)90469-2`.

[8] S. Weinberg, "A Model of Leptons", *Phys. Rev. Lett.* **19** (Nov, 1967) 1264–1266. `doi:10.1103/PhysRevLett.19.1264`.

[9] S. L. Glashow, J. Iliopoulos, and L. Maiani, "Weak Interactions with Lepton-Hadron Symmetry", *Phys. Rev.* **D2** (1970) 1285–1292. `doi:10.1103/PhysRevD.2.1285`.

[10] D. J. Gross and F. Wilczek, "Asymptotically Free Gauge Theories. I", *Phys. Rev. D* **8** (Nov, 1973) 3633–3652. `doi:10.1103/PhysRevD.8.3633`.

[11] K.A. Olive et al. (Particle Data Group), "Review of particle physics", *Chin. Phys. C, 38, 090001 (2014)* (2014).

[12] C. S. Wu, E. Ambler, R. W. Hayward et al., "Experimental Test of Parity Conservation in Beta Decay", *Phys. Rev.* **105** (Feb, 1957) 1413–1415. `doi:10.1103/PhysRev.105.1413`.

[13] M. Goldhaber, L. Grodzins, and A. W. Sunyar, "Helicity of Neutrinos", *Phys. Rev.* **109** (Feb, 1958) 1015–1017. `doi:10.1103/PhysRev.109.1015`.

[14] F. Englert and R. Brout, “Broken Symmetry and the Mass of Gauge Vector Mesons”, *Phys. Rev. Lett.* **13** (Aug, 1964) 321–323. `doi:10.1103/PhysRevLett.13.321`.

[15] P. Higgs, “Broken symmetries, massless particles and gauge fields”, *Physics Letters* **12** (1964), no. 2, 132 – 133. `doi:10.1016/0031-9163(64)91136-9`.

[16] P. W. Higgs, “Broken Symmetries and the Masses of Gauge Bosons”, *Phys. Rev. Lett.* **13** (Oct, 1964) 508–509. `doi:10.1103/PhysRevLett.13.508`.

[17] J. Goldstone, A. Salam, and S. Weinberg, “Broken Symmetries”, *Phys. Rev.* **127** (1962) 965–970. `doi:10.1103/PhysRev.127.965`.

[18] G. S. Guralnik, C. R. Hagen, and T. W. B. Kibble, “Global Conservation Laws and Massless Particles”, *Phys. Rev. Lett.* **13** (1964) 585–587. `doi:10.1103/PhysRevLett.13.585`.

[19] CMS Collaboration, “Observation of a new boson at a mass of 125 GeV with the CMS experiment at the LHC”, *Physics Letters B* **716** (2012), no. 1, 30 – 61. `doi:10.1016/j.physletb.2012.08.021`.

[20] ATLAS Collaboration, “Observation of a new particle in the search for the Standard Model Higgs boson with the ATLAS detector at the LHC”, *Phys. Lett.* **B716** (2012) 1–29, `arXiv:1207.7214`. `doi:10.1016/j.physletb.2012.08.020`.

[21] K. Ellis, J. Stirling, and B. Webber, “QCD and Collider Physics”. Cambridge Monographs on Particle Physics, Nuclear Physics and Cosmology, 2003.

[22] R. D. Ball et al., “Parton distributions for the LHC run II”, *Journal of High Energy Physics* **B716** (2015).

[23] K.A. Olive et al. (Particle Data Group), “Review of particle physics”, *Chin. Phys. C, 38, 010009 (2014) and 2015 update* (2015).

[24] L. Evans and P. Bryant, “LHC Machine”, *Journal of Instrumentation* **3** (2008), no. 08, S08001.

[25] ATLAS Collaboration, “The ATLAS Experiment at the CERN Large Hadron Collider”, *JINST* **3** (2008) S08003. `doi:10.1088/1748-0221/3/08/S08003`.

[26] CMS Collaboration, “The CMS experiment at the CERN LHC”, *JINST* **3** (2008), no. S08004,. `doi:10.1088/1748-0221/3/08/S08004`.

[27] ALICE Collaboration, “The ALICE experiment at the CERN LHC ”, *JINST* **3** (2008) S08002. `doi:10.1088/1748-0221/3/08/S08002`.

[28] LHCb Collaboration, “The LHCb Detector at the LHC ”, *JINST* **3** (2008) S08005. `doi:10.1088/1748-0221/3/08/S08005`.

[29] V. Berardi et al., "TOTEM: Technical design report. Total cross section, elastic scattering and diffraction dissociation at the Large Hadron Collider at CERN", (2008).

[30] O. Adriani et al., "Technical design report of the LHCf experiment: Measurement of photons and neutral pions in the very forward region of LHC", (2006).

[31] CERN Website. `https://bigscience.web.cern.ch/bigscience/Objects/LHC/accelerator.jpg`.

[32] CMS Collaboration, "Description and performance of track and primary-vertex reconstruction with the CMS tracker", *JINST* **9** (2014), no. 10, P10009. `doi:10.1088/1748-0221/9/10/P10009`.

[33] P. Adzic et al., "Energy resolution of the barrel of the CMS electromagnetic calorimeter", *JINST* **2** (2007) P04004. `doi:10.1088/1748-0221/2/04/P04004`.

[34] CMS Collaboration, "The performance of the CMS muon detector in proton-proton collisions at sqrt(s) = 7 TeV at the LHC", *JINST* **8** (2013) P11002, `arXiv:1306.6905`. `doi:10.1088/1748-0221/8/11/P11002`.

[35] CMS Collaboration, "The CMS trigger system", `arXiv:1609.02366`.

[36] I. Bird, "Computing for the Large Hadron Collider", *Ann.Rev.Nucl.Part.Sci.* **61** (2011) 99–118. `doi:10.1146/annurev-nucl-102010-130059`.

[37] J. Neyman and E. S. Pearson, "On the Problem of the Most Efficient Tests of Statistical Hypotheses", *Phil. Trans. R. Soc. Lond. A* (1933) 231:289–337.

[38] A. L. Read, "Modified frequentist analysis of search results (The CL(s) method)", in *Workshop on confidence limits, CERN, Geneva, Switzerland, 17-18 Jan 2000: Proceedings*, pp. 81–101. 2000.

[39] A. L. Read, "Presentation of search results: the $\mathrm{CL_s}$ technique", *Journal of Physics G: Nuclear and Particle Physics* **28** (2002), no. 10, 2693.

[40] G. Cowan, K. Cranmer, E. Gross et al., "Asymptotic formulae for likelihood-based tests of new physics", *Eur. Phys. J.* **C71** (2011) 1554, `arXiv:1007.1727`. [Erratum: Eur. Phys. J.C73,2501(2013)]. `doi:10.1140/epjc/s10052-011-1554-0, 10.1140/epjc/s10052-013-2501-z`.

[41] A. Wald, "Tests of statistical hypotheses concerning several parameters when the number of observations is large", *Trans. Amer. Math. Soc.* **54** (1943) 426–482. `doi:10.1090/S0002-9947-1943-0012401-3`.

[42] CMS Collaboration, "MUSiC - An Automated Scan for Deviations between Data and Monte Carlo Simulation", *CMS Physics Analysis Summary CMS-PAS-EXO-08/005* (2008).

[43] T. Hebbeker, “A Global Comparison between L3 Data and Standard Model Monte Carlo - a first attempt”. `https://web.physik.rwth-aachen.de/~hebbeker/l3note_2305.pdf`, L3 note 1998.

[44] DØ Collaboration, “Quasi-model-independent search for new physics at large transverse momentum”, *Phys. Rev. D* **64** (Jun, 2001) 012004. `doi:10.1103/PhysRevD.64.012004`.

[45] DØ Collaboration Collaboration, “Search for new physics in $e\mu X$ data at DØ using SLEUTH: A quasi-model-independent search strategy for new physics”, *Phys. Rev. D* **62** (Oct, 2000) 092004. `doi:10.1103/PhysRevD.62.092004`.

[46] D0 Collaboration Collaboration, “Quasi-Model-Independent Search for New High p_T Physics at D0”, *Phys. Rev. Lett.* **86** (Apr, 2001) 3712–3717. `doi:10.1103/PhysRevLett.86.3712`.

[47] CDF Collaboration, “Model-Independent and Quasi-Model-Independent Search for New Physics at CDF”, *Phys. Rev.* **D78** (2008) 012002, `arXiv:0712.1311`. `doi:10.1103/PhysRevD.78.012002`.

[48] CDF Collaboration, “Global search for new physics with 2.0 fb^{-1} at CDF”, *Phys. Rev. D* **79** (Jan, 2009) 011101. `doi:10.1103/PhysRevD.79.011101`.

[49] H1 Collaboration, “A General search for new phenomena in ep scattering at HERA”, *Phys. Lett.* **B602** (2004) 14–30, `arXiv:hep-ex/0408044`. `doi:10.1016/j.physletb.2004.09.057`.

[50] ATLAS Collaboration, “A general search for new phenomena with the ATLAS detector in pp collisions at $\sqrt{s} = 8$ TeV”, Technical Report ATLAS-CONF-2014-006, CERN, Geneva, Mar, 2014.

[51] C. Hof, “Implementation of a model independent search for new physics with the CMS detector exploiting the world-wide LHC computing grid”. PhD thesis, RWTH Aachen University, 2009.

[52] P. A. Biallass, “Commissioning of the CMS muon detector and development of generic search strategies for new physics”. PhD thesis, RWTH Aachen University, 2009.

[53] H. Pieta, “MUSiC - a Model Unspecific Search in CMS based on 2010 LHC data”. PhD thesis, RWTH Aachen University, 2012.

[54] P. Papacz, “Model unspecific search for new physics in CMS based on 2011 data”. PhD thesis, RWTH Aachen University, 2014.

[55] CMS Collaboration, “Model Unspecific Search for New Physics in pp Collisions at sqrt(s) = 7 TeV”, *CMS Physics Analysis Summary CMS-PAS-EXO-10/021* (2011).

[56] CMS Collaboration, "Particle Flow Event Reconstruction in CMS and Performance for Jets, Taus, and missing transverse energy", *CMS Physics Analysis Summary CMS PAS PFT-09/001* (2009) 25.

[57] CMS Collaboration, "CMS Luminosity Based on Pixel Cluster Counting - Summer 2013 Update", *CMS Physics Analysis Summary CMS-PAS-LUM-13/001* (2013).

[58] The PDF4LHC working group, "Recommendation for LHC cross section calculations". `http://www.hep.ucl.ac.uk/pdf4lhc/`.

[59] CMS Collaboration, "Search for physics beyond the standard model in dilepton mass spectra in proton-proton collisions at sqrts = 8 TeV", *Journal of High Energy Physics* **2015** (2015), no. 4, 25. `doi:10.1007/JHEP04(2015)025`.

[60] L. Thomas, "Search for new heavy narrow resonances decaying into a dielectron pair with the CMS detector". PhD thesis, Brussels U., 2014.

[61] Kuan Hsin Chen et al., "The Scale Factors for Photon Selection (Jan22ReReco v.s. s10 MC)". `https://indico.cern.ch/event/305105/contributions/1672017/attachments/579290/797665/CutBasedPhotonIDSF_v2.pdf`.

[62] C. Biggio et al., "Search for heavy lepton partners of neutrinos in pp collisions at 8 TeV, in the context of Type III seesaw mechanism", *CMS Analysis Note: AN-13-135.*

[63] A. Askew et al., "Search for Dark Matter and Large Extra Dimensions in the gamma+MET final state in pp collisions at sqrt(s)=8 TeV in the CMS experiment with 19.6 fb-1 of data", *CMS Analysis Note: AN-12-439.*

[64] CMS Collaboration, "Reference muon momentum scale and resolution". `https://twiki.cern.ch/twiki/bin/viewauth/CMS/MuonReferenceResolution?rev=28`, 29.09.2015.

[65] CMS Collaboration Collaboration, "ECAL Detector Performance, 2011 Data". `https://cds.cern.ch/record/1457922`.

[66] CMS Collaboration, "Jet energy scale and resolution in the CMS experiment in pp collisions at 8 TeV", *Submitted to: JINST* (2016) `arXiv:1607.03663`.

[67] CMS Collaboration, "Performance of the CMS missing transverse momentum reconstruction in pp data at $\sqrt{s} = 8$ TeV", *JINST* **10** (2015), no. 02, P02006, `arXiv:1411.0511`. `doi:10.1088/1748-0221/10/02/P02006`.

[68] T. Sjöstrand, S. Mrenna, and P. Z. Skands, "PYTHIA 6.4 Physics and Manual", *JHEP* **05** (2006) 026. `doi:10.1088/1126-6708/2006/05/026`.

[69] T. Sjöstrand, S. Ask, J. R. Christiansen et al., "An Introduction to PYTHIA 8.2", *Comput. Phys. Commun.* **191** (2015) 159–177, `arXiv:1410.3012`. `doi:10.1016/j.cpc.2015.01.024`.

[70] A. Albert, "Extension of the Model Unspecific Search in CMS to Final States with Jets using 2012 Data", Master's thesis, RWTH, 2015.

[71] S. Agostinelli, J. Allison, K. Amako et al., "Geant4—a simulation toolkit", *Nuclear Instruments and Methods in Physics Research Section A: Accelerators, Spectrometers, Detectors and Associated Equipment* **506** (2003), no. 3, 250 – 303. `doi:http://dx.doi.org/10.1016/S0168-9002(03)01368-8`.

[72] H.-L. Lai, M. Guzzi, J. Huston et al., "New parton distributions for collider physics", *Phys. Rev.* **D82** (2010) 074024, `arXiv:1007.2241`. `doi:10.1103/PhysRevD.82.074024`.

[73] A. D. Martin, W. J. Stirling, R. S. Thorne et al., "Parton distributions for the LHC", *Eur. Phys. J.* **C63** (2009) 189–285, `arXiv:0901.0002`. `doi:10.1140/epjc/s10052-009-1072-5`.

[74] R. D. Ball et al., "Parton distributions with LHC data", *Nucl. Phys.* **B867** (2013) 244–289, `arXiv:1207.1303`. `doi:10.1016/j.nuclphysb.2012.10.003`.

[75] CMS Collaboration, "Performance of CMS muon reconstruction in pp collision events at $\sqrt{s} = 7$ TeV", *JINST* **7** (2012) P10002, `arXiv:1206.4071`. `doi:10.1088/1748-0221/7/10/P10002`.

[76] S. Erdweg, "Search for Dark Matter and W' in the final state with one muon and missing transverse energy with CMS", Master's thesis, RWTH, 2013.

[77] CMS Collaboration, "Performance of electron reconstruction and selection with the CMS detector in proton-proton collisions at $\sqrt{\mathrm{s}} = 8$ TeV", *Journal of Instrumentation* **10** (2015), no. 06, P06005.

[78] W. Adam, R. Frühwirth, A. Strandlie et al., "Reconstruction of electrons with the Gaussian-sum filter in the CMS tracker at the LHC", *Journal of Physics G: Nuclear and Particle Physics* **31** (2005), no. 9, N9.

[79] R. Frühwirth and S. Frühwirth-Schnatter, "On the treatment of energy loss in track fitting", *Computer Physics Communications* **110** (1998), no. 1, 80 – 86. `doi:http://dx.doi.org/10.1016/S0010-4655(97)00157-4`.

[80] CMS Collaboration, "Performance of photon reconstruction and identification with the CMS detector in proton-proton collisions at $\sqrt{\mathrm{s}} = 8$ TeV", *Journal of Instrumentation* **10** (2015), no. 08, P08010. `doi:10.1088/1748-0221/10/08/P08010`.

[81] M. Cacciari, G. P. Salam, and G. Soyez, "The Anti-k_T jet clustering algorithm", *JHEP* **0804** (2008) 063, `arXiv:0802.1189`. `doi:10.1088/1126-6708/2008/04/063`.

[82] CMS Collaboration, “CMS MET Filters”. `https://twiki.cern.ch/twiki/bin/view/CMS/MissingETOptionalFilters?rev=66`, 27.05.2015.

[83] S. Chang, S. Erdweg, K. Hoepfner et al., “Search for new physics in the single lepton + MET final states with the full 2012 dataset at sqrt(s)=8 TeV”, *CMS AN-12-423* (2012).

[84] J. de Favereau, C. Delaere, P. Demin et al., “DELPHES 3: a modular framework for fast simulation of a generic collider experiment”, *Journal of High Energy Physics* **2014** (2014), no. 2, 57. `doi:10.1007/JHEP02(2014)057`.

[85] M. Drees, H. Dreiner, D. Schmeier et al., “CheckMATE: Confronting your Favourite New Physics Model with LHC Data”, *Comput. Phys. Commun.* **187** (2015) 227–265, `arXiv:1312.2591`. `doi:10.1016/j.cpc.2014.10.018`.

[86] K. Cranmer and I. Yavin, “RECAST — extending the impact of existing analyses”, *Journal of High Energy Physics* **2011** (2011), no. 4, 38. `doi:10.1007/JHEP04(2011)038`.

[87] D0 Collaboration Collaboration, “Search for New Physics Using QUAERO: A General Interface to D0 Event Data”, *Phys. Rev. Lett.* **87** (Nov, 2001) 231801. `doi:10.1103/PhysRevLett.87.231801`.

[88] S. Caron and B. Knuteson, “QUAERO@H1: an interface to high-p_T HERA event data”, *The European Physical Journal C* **53** (2008), no. 1, 167–175. `doi:10.1140/epjc/s10052-007-0468-3`.

[89] CMS Collaboration, “Documentation of the RooStats -based statistics tools for Higgs PAG”. `https://twiki.cern.ch/twiki/bin/view/CMS/SWGuideHiggsAnalysisCombinedLimit?rev=158`, 24.10.2016.

[90] RooStats Collaboration, “RooStats, 2012”. `https://twiki.cern.ch/twiki/bin/view/CMS/RooStats`, 08.10.2012.

[91] J. Alwall et al., “A Standard format for Les Houches event files”, *Comput. Phys. Commun.* **176** (2007) 300–304, `arXiv:hep-ph/0609017`. `doi:10.1016/j.cpc.2006.11.010`.

[92] M. Dobbs and J. B. Hansen, “The HepMC C++ Monte Carlo event record for High Energy Physics.”, *Computer Physics Communications* **134** (2001), no. 1, 41 – 46. `doi:10.1016/S0010-4655(00)00189-2`.

[93] Seth Zenz, “Github repository for Delphes.”. `https://github.com/sethzenz/Delphes/commit/7a3c2aaa36845e9e71d69399de58be5d459e0e34`.

[94] M. Olschewski, “Search for new physics in proton-proton collision events with a lepton and missing transverse energy”. PhD thesis, RWTH Aachen University, 2016.

[95] G. Altarelli, B. Mele, and M. Ruiz-Altaba, "Searching for New Heavy Vector Bosons in $p\bar{p}$ Colliders", *Z. Phys.* **C45** (1989) 109.

[96] A. Leike, "The phenomenology of extra neutral gauge bosons", *Physics Reports* **317** (1999), no. 3–4, 143 – 250. `doi:http://dx.doi.org/10.1016/S0370-1573(98)00133-1`.

[97] J. Pumplin, D. R. Stump, J. Huston et al., "New Generation of Parton Distributions with Uncertainties from Global QCD Analysis", *Journal of High Energy Physics* **2002** (2002), no. 07, 012.

[98] G. Alverson, I. Belotelo, D. Bourilkov et al., "Search for High-Mass Resonances Decaying to Muon Pairs in pp Collisions at $\sqrt{\mathrm{s}} = 8$ TeV", *CMS Analysis Note: AN-12-422*.

[99] W. Buchmüller, R. Rückl, and D. Wyler, "Leptoquarks in lepton-quark collisions", *Physics Letters B* **191** (1987), no. 4, 442 – 448. `doi:10.1016/0370-2693(87)90637-X`.

[100] Emanuela Barberis, Darin Baumgartel and David Morse, "Search for Pair-production of Second generation Leptoquarks in 8 TeV proton-proton collisions.", *CMS Analysis Note: AN-12-481*.

[101] CMS Collaboration Collaboration, "Search for physics beyond the standard model in final states with a lepton and missing transverse energy in proton-proton collisions at $\sqrt{s} = 8$ TeV", *Phys. Rev. D* **91** (May, 2015) 092005. `doi:10.1103/PhysRevD.91.092005`.

[102] CMS Collaboration, "Search for pair production of first and second generation leptoquarks in proton-proton collisions at $\sqrt{\mathrm{s}} = 8$ TeV", *CMS Physics Analysis Summary CMS PAS EXO-12-041* (2015).

Danksagung

Zum Abschluss meiner Dissertation möchte ich den vielen Personen danken, die mich während meiner Promotion unterstützt haben und ohne die diese Arbeit nicht möglich gewesen wäre.

Zuallererst danke ich Prof. Dr. Thomas Hebbeker, der es mir ermöglicht hat, diese Arbeit am III. Physikalischen Institut durchführen zu können und mir bei vielen Herausforderungen mit Rat zur Seite stand.

Ausserdem danke ich Dr. Arnd Meier für die Betreuung während meiner Promotion und für das Korrekturlesen von großen Teilen meiner Arbeit.

Mein ganz besonderer Dank gilt meiner Bürokollegin Deborah Duchardt für die intensive Zusammenarbeit in der MUSiC Arbeitsgruppe und für viele hilfreiche Diskussionen.

Vielen Dank möchte ich auch allen anderen Kollegen aus der Aachener Arbeitsgruppe für die tolle Arbeitsatmosphäre aussprechen: Bei Fragen und Problemen fand ich stets jemanden der mir hilfreich zur Seite standen oder mir Gesellschaft bei einer Tasse Kaffee leistete.

Aussserdem danke ich Dr. Lisa Edelhäuser und Dr. Alexander Knochel die mir nicht nur viele Theoriekonzepte nähergebracht haben, sondern mich auch auf die Idee gebracht haben, modellunabhängige Limits zum Thema meiner Dissertation zu machen.

Des Weiteren danke ich meinem Bruder Philipp, der mir geholfen hat, die Zeichensetzung in meiner Arbeit unter Kontrolle zu bringen.

Zum Abschluss möchte ich auch meinen Eltern und meiner ganzen Familie danken, die mich während meines gesamten Studium stets unterstützt haben.